Delft University of Technology

Thermoelastic Stability of Deployable Space Telescopes

Villalba, Víctor

DOI
10.4233/uuid:0e98bb62-5518-4c59-9f6a-b845b8a71997

Publication date
2023

Document Version
Final published version

Citation (APA)
Villalba, V. (2023). *Thermoelastic Stability of Deployable Space Telescopes*. [Dissertation (TU Delft), Delft University of Technology]. https://doi.org/10.4233/uuid:0e98bb62-5518-4c59-9f6a-b845b8a71997

Important note
To cite this publication, please use the final published version (if applicable).
Please check the document version above.

Copyright
Other than for strictly personal use, it is not permitted to download, forward or distribute the text or part of it, without the consent of the author(s) and/or copyright holder(s), unless the work is under an open content license such as Creative Commons.

Takedown policy
Please contact us and provide details if you believe this document breaches copyrights.
We will remove access to the work immediately and investigate your claim.

This work is downloaded from Delft University of Technology.
For technical reasons the number of authors shown on this cover page is limited to a maximum of 10.

THERMOELASTIC STABILITY OF DEPLOYABLE SPACE TELESCOPES

THERMOELASTIC STABILITY OF DEPLOYABLE SPACE TELESCOPES

Proefschrift

ter verkrijging van de graad van doctor
aan de Technische Universiteit Delft,
op gezag van de Rector Magnificus prof. dr. ir. T.H.J.J. van der Hagen,
voorzitter van het College voor Promoties,
in het openbaar te verdedigen op
donderdag 9 maart 2023 om 15:00 uur.

door

Víctor Manuel VILLALBA CORBACHO

Master of Science in Space Technology,
Luleå Tekniska Universitet, Luleå, Zweden
geboren te Málaga, Spanje.

Dit proefschrift is goedgekeurd door de

Rector Magnificus	Chairman
Promotor: Prof. dr. E.K.A. Gill	Technische Universiteit Delft
Copromotor: dr. ir. J.M. Kuiper	Technische Universiteit Delft

Onafhankelijke leden:

Prof. dr. ir. J.L. Herder	Technische Universiteit Delft
Prof. dr. ir. R. Vingerhoeds	ISAE-SUPAERO
Prof. Dr.-Ing. E. Stoll	Technische Universität Berlin
Dr. S. R. Turteltaub	Technische Universiteit Delft
Prof. dr. P.G. Steeneken	Technische Universiteit Delft, reserve member

Keywords: thermoelastics, deployable space telescopes, piezoelectric actuators, compliant mechanisms, mechanical design, systems engineering

Printed by: Ridderprint

Front & Back: Cover art made by Alexandra Zamolex.

Copyright © 2023 by V. Villalba Corbacho

ISBN 978-94-6458-915-3

An electronic version of this dissertation is available at
http://repository.tudelft.nl/.

A mis padres.

CONTENTS

SUMMARY

Imagery collected from space provides very useful information about our planet. Today there are many Earth Observation satellites in orbit which allow us to collect information which is used for environmental monitoring, response to catastrophes, surveillance and security, urban planning, economic analysis and many other applications. Thus, there is a drive to improve the quality of this imagery, such as its resolution and the frequency with which it can be collected. The quantity of pictures taken will be increased by launching more systems, the quality of the pictures depends, amongst other factors, on the system's physical size. To serve those needs, bigger telescopes have to be launched more often.

One of the ideas to keep launch costs affordable whilst increasing the sizes of the optical systems is to use deployable optical systems, which are comparatively light and small, but reach their large size once in space. However, positioning of the optical elements in such systems is critical to their performance. The goal of this dissertation is to examine the different thermal and mechanical challenges to the operation of deployable space telescopes for Earth Observation. A literature study was performed to establish what those challenges are and identify which critical technologies enable deployable space telescopes. For astronomy applications, the success of the James Webb Space Telescope shows that this type of system is possible, but it faced substantially different challenges from a thermal standpoint, which are also detailed in this thesis. The thermoelastic behaviour of deployable telescopes in low Earth orbit was chosen as a main focus for the rest of the research project.

The literature study highlighted the importance of correction mechanisms which can correct the positioning of the optical elements in order to mitigate the effect of the disturbance that are encountered in the space environment. These disturbances may come from loads during launch and deployment, thermal cycling over the orbit, or vibrations caused by the spacecraft systems. The second part of this thesis is devoted to design and modelling of an active optics mechanism for the Delft Deployable Space Telescope project, which is a case study for the design of a deployable telescope for Earth Observation with sub-metre resolution on the ground. A design and trade-off methodology taking into account the choices that need to be made regarding geometry, actuator technology and material selection was conducted. The design is then supported by computational modelling covering kinematic performance, launch survival and thermoelastic deformation under orbital conditions.

In order to build confidence that these models are reliable, a model verification and validation approach was defined and executed. The validation approach includes the use of parallel multiphysics modelling, and a novel thermoelastic testing method. The test consists of heating the test item and examining final position of its end effector. This test method is analogous to thermoelastic tests performed with simple geometries which can be found in literature, but the complex geometry introduces challenges in decomposing the behaviour of the structure. The thermoelastic testing methodology requires its own verification and validation. A hybrid approach was used to integrate verification and validation both on the models and the test setup was utilised. The models could ultimately not be validated, but lessons learned were compiled. The main reason why the testing approach does not provide sufficient information for model diagnosis is its inability to separate mechanisms of thermal expansion in the complex structure of the flexured frame. Thus, a stepwise approach to thermoelastic test validation is required. A sensitivity analysis was performed on the model results to discard known, potential sources of error. However, none of the parameters studied changes the behaviour of the model enough to explain the difference between model predictions and experimental results.

In addition to thermoelastic modelling and testing, experimental modal analysis was also performed on the test item. However, the eigenfrequencies of the test item were not well predicted by neither of the finite element modal analyses performed. The main features of the eigenmode shapes could be predicted due to the dominance of the massive intermediate bodies in the mass distribution of the test item.

The final part of this thesis focuses on the thermal emission due to self-heating of piezoelectric actuators, as these are one of the more advantageous technologies to power active optics mechanisms for this type of application. A novel experimental setup was designed, constructed and operated to characterise the power dissipation and temperature profile of actuators in vacuum and with controlled boundary conditions. The experimental setup consists of a thermally controlled enclosure which allows only one path for evacuation of the heat dissipated by the actuator. A control system dissipating a known amount of heat keeps the temperature of the heat path stable, so the addition of power dissipated by the actuator causes a measurable drop in the power produced by the control system.

The results of the experiment do not show a strong dependency of thermal emission on the initial temperature of the item, contrary to the literature on the topic. This discrepancy is likely the result of the very limited heat evacuation from the test item under vacuum conditions. The results also indicate that, in vacuum conditions, a potential factor limiting the stroke and frequency of active optics correction is the self-heating of the actuators. This is expected in the case of thermal runaway, which is known to be a danger to the actuator's integrity, but it can also lead to unwanted thermoelastic deformations on the mechanism frame.

In conclusion, the lessons on the importance of thermal and thermoelastic challenges on the development of deployable space telescopes have been compiled. Ideas for future work, specially in the development of active optics systems for deployable optics applications taking into account thermoelastic effects, are also presented.

SAMENVATTING

Beelden verzameld vanuit de ruimte bieden zeer nuttige informatie over onze planeet. Tegenwoordig zijn er veel aardobservatiesatellieten in een baan om de aarde waarmee we informatie kunnen verzamelen die wordt gebruikt voor milieumonitoring, reactie op rampen, bewaking en veiligheid, stadsplanning, economische analyse en vele andere toepassingen. Er is dus een drive om de kwaliteit van deze beelden te verbeteren, zoals de resolutie en de frequentie waarmee ze kunnen worden verzameld. Het aantal gemaakte foto's kan worden verhoogd door meer systemen te lanceren, de kwaliteit van de foto's hangt onder andere af van de fysieke grootte van het systeem. Om aan die behoeften te voldoen, moeten er vaker grotere telescopen worden gelanceerd.

Een van de ideeën om de lanceringskosten betaalbaar te houden en tegelijkertijd de afmetingen van de optische systemen te vergroten, is het gebruik van ontvouwbare optische systemen, die relatief licht en klein zijn, maar hun grote omvang kunnen bereiken wanneer ze eenmaal in de ruimte zijn. De positionering van de optische elementen in dergelijke systemen is echter cruciaal voor hun prestaties. Het doel van dit proefschrift is het onderzoeken van de verschillende thermische en mechanische uitdagingen voor de werking van ontvouwbare ruimtetelescopen voor aardobservatie. Er is een literatuurstudie uitgevoerd om vast te stellen wat die uitdagingen zijn en welke doorslaggevende technologieën ontvouwbare ruimtetelescopen mogelijk maken. Voor astronomische toepassingen laat het succes van de James Webb ruimtetelescoop zien dat dit type systeem mogelijk is, maar vanuit thermisch oogpunt voor aanzienlijk andere uitdagingen stond, die ook in dit proefschrift worden beschreven. Het thermo-elastische gedrag van ontvouwbare telescopen in een lage baan om de aarde werd gekozen als hoofdfocus voor de rest van het onderzoeksproject.

De literatuurstudie benadrukte het belang van correctiemechanismen die de positionering van de optische elementen kunnen corrigeren om het effect van de verstoringen die in de ruimteomgeving optreden te verminderen. Deze verstoringen kunnen afkomstig zijn van belastingen tijdens lanceren en ontvouwen, thermische cycli over de baan of trillingen veroorzaakt door de ruimtevaartuigsystemen. Het tweede deel van dit proefschrift is gewijd aan het ontwerp en de modellering van een actief optisch mechanisme voor het Delft Deployable Space Telescope project, een casestudy voor het ontwerp van een ontvouwbare telescoop voor aardobservatie met een resolutie van minder dan een meter op de grond. Er werd een ontwerp en afwegingsmethodiek uitgevoerd waarbij rekening werd gehouden met de keuzes die moeten worden gemaakt met betrekking tot geometrie, actuatortechnologie en materiaalkeuze. Het ontwerp wordt vervolgens ondersteund door computermodellering die kinematische prestaties, lanceringsoverleving en thermo-elastische vervorming onder orbitale omstandigheden omvat.

Om het vertrouwen op te bouwen dat deze modellen betrouwbaar zijn, werd een modelverificatie en validatiestrategie gedefinieerd en uitgevoerd. De validatiestrategie omvat het gebruik van parallelle multifysische modellering en een nieuwe thermo-elastische testmethode. De test bestaat uit het opwarmen van het testonderdeel en het onderzoeken van de uiteindelijke positie van de eindeffector. Deze testmethode is analoog aan thermo-elastische tests die worden uitgevoerd met eenvoudige geometrieën en die in de literatuur te vinden zijn, maar de complexe geometrie introduceert uitdagingen bij het ontleden van het gedrag van de constructie. De thermoelastische testmethode vereist zijn eigen verificatie en validatie. Er werd een hybride aanpak gebruikt om verificatie en validatie zowel op de modellen als op de testopstelling te integreren. De modellen konden uiteindelijk niet worden gevalideerd, maar de opgedane ervaringen werden verzameld. De belangrijkste reden waarom de testbenadering niet voldoende informatie biedt voor modeldiagnose, is het onvermogen om mechanismen van thermische uitzetting in de complexe structuur van het gebogen frame te scheiden. Een stapsgewijze benadering van thermoelastische testvalidatie is dus vereist. Er is een gevoeligheidsanalyse uitgevoerd op de modelresultaten om bekende, potentiële foutbronnen te negeren. Geen van de bestudeerde parameters verandert het gedrag van het model echter voldoende om het verschil tussen modelvoorspellingen en experimentele resultaten te verklaren.

Naast thermo-elastische modellering en testen werd ook experimentele modaalanalyse uitgevoerd op het testitem. De eigenfrequenties van het testonderdeel werden echter niet goed voorspeld door geen van de uitgevoerde eindige elementen modaalanalyses. De belangrijkste kenmerken van de eigenmode vormen konden worden voorspeld vanwege de dominantie van de massieve tussenlichamen in de massaverdeling van het testitem.

Het laatste deel van dit proefschrift richt zich op de thermische emissie als gevolg van zelfverhitting van piëzo-elektrische actuatoren, aangezien dit een van de meest voordelige technologieën is om actieve optische mechanismen voor dit type toepassing aan te drijven. Een nieuwe experimentele opstelling werd ontworpen, gebouwd en gebruikt om de vermogensdissipatie en het temperatuurprofiel van actuatoren in een vacuüm en met gecontroleerde randvoorwaarden te karakteriseren. De experimentele opstelling bestaat uit een thermisch gecontroleerde behuizing die slechts één pad toelaat voor evacuatie van de warmte die door de actuator wordt gedissipeerd. Een besturingssysteem dat een bekende hoeveelheid warmte afvoert, houdt de temperatuur van het warmtepad stabiel, dus de toevoeging van vermogen dat door de actuator wordt gedissipeerd, veroorzaakt een meetbare daling van het vermogen dat door het besturingssysteem wordt geproduceerd.

De resultaten van het experiment laten geen sterke afhankelijkheid zien van thermische emissie van de begintemperatuur van het item, in tegenstelling tot de literatuur over dit onderwerp. Dit verschil is waarschijnlijk het resultaat van de zeer beperkte warmteafvoer van het testvoorwerp onder vacuümomstandigheden. De resultaten geven ook aan dat, in vacuümomstandigheden, een potentiële factor die de slag en frequentie van actieve optische correctie beperkt, de zelfopwarming van de actuatoren is. Dit wordt verwacht in het geval van thermische ontsnapping, waarvan bekend is dat het een gevaar vormt voor de integriteit van de actuator, maar het kan ook leiden tot ongewenste thermo-elastische vervormingen op het frame van het mechanisme.

Tot slot zijn de lessen over het belang van thermische en thermo-elastische uitdagingen voor de ontwikkeling van ontvouwbare ruimtetelescopen verzameld. Ideeën voor toekomstig werk, met name bij de ontwikkeling van actieve optische systemen voor ontvouwbare optische toepassingen, rekening houdend met thermo-elastische effecten, worden ook gepresenteerd.

ACKNOWLEDGEMENTS

Most people who have met me know that I have a particularly acidic, some may say corrosive, sense of humour. After the five years I have spent working on this thesis, I could say it is time to break character for a bit and extend a heartfelt thank you to the people who have helped me with it. However, I will say no such thing.

Firstly I would like to thank my supervisor, Hans Kuiper, for giving me the chance to do this PhD and his support, even though at times it was hard to agree what I needed to do. The freedom he gave me was a big part of the experience as a doctoral candidate, I hope he can find some value in this work too. Also to my promotor Eberhard Gill for his guidance and constructive criticism. In addition, I can assure that without him this thesis would contain even more typos and mistakes than it does.

Outside of my supervisors, I want to thank Just Herder. Now, we could spend a while discussing professor Herder's qualities, but we need to leave some ink for the rest of the thesis. Dennis Dolkens' help with starting this process is much appreciated, and I hope he can complete his own doctorate soon. I also learned a lot about engineering from Rudolf Saathof, I only wish he could learn as much about jokes from me. Jaap Meijaard, Jos van Driel and Stefano Speretta were also helpful at different stages of this work. I also need to thank the many MSc students we have had in the DST project at TU Delft, as there was always more to explore than I could ever do myself. Sean Pepper's work in particular was very important for my own. The members of the thermal control section of the NLR in Marknesse also deserve credit for their help, and for their show of how a competent research team functions. As a PhD, I also had the chance to do educational work, which brought me to meet Julien van Campen and Rene Alderliesten, who are both very fun people. It also implied some tough bartering with Barry Zandbergen, but that was fun too.

Joshua Spaander is likely the most helpful person I will ever meet, from technical discussion to storage solutions, including comic relief, Joshua helps with everything. I must admit I do not know how or when this thesis would have been completed if not for him. Mario Badás did what he does best, and kidnapped me to do mechanical modelling, which was very useful. I also need to acknowledge the help of Srikanth Vasudevan and Jurij Sodja.

Other PhDs warmly welcomed me when I arrived: Fiona, Johan el Patrón, Marsil, Daduí, Zixuan, Mario, Minghe, Linyu, and eventually Sevket, under special circumstances. The newer dear colleagues are also to be thanked for the fun times, especially my ramen partner Stefano, but also the others: Lorenzo, Stefano (yet another), Erdem, Ruipeng, Jingyi, Rashika, Juan, and also ninth floor recruits Livio, Tara, Natalia and Marie. Rens' Google-assisted translation services are also highly appreciated. It was always fun to go to the PhD drinks and catch up with Kirk, Kim, Colin, Javi, Inés, Bruce, Silvia, Reynard, Ata, Bieke, Anique, and of course Roberto, who was always expanding the drinking with cool people who were not supposed to be there, like Santi, Ligaya, Jason, Sharath and Shakti.

Thanks also to Bart van de Laar and his Spartan workout pupils, Mascha, Ravi, Fernando, Marc, Umu, Francesc, and especially to Jori, who was my family when I was cut off from mine. Thanks to the staff of the X gym, where I never spent enough time, as well as the people I met there.

My friends group from Seville, Adri, Ángel, Javi, Fran, Rafa, Miky, Samu, Jesús, Antonio, Juanma, Manu and Pelayo are all very special, and by special here I mean unbelievably bad at videogames. José, Raúl, Paco and Álvaro still stand me after a whole decade, which is surprising. Also Sandri, who taught me I should not make a career in ticket sales or club security. I also need to mention Juan Manuel Lora, but it will be in the same sentence as Rosa and Luminita just to curb how special he feels. Kind regards to other friends I made during the masters, Vanessa, Camille, Jonathan, Luka, Alex, Anjana, Angèle, Elliot, Maros, Shehryar, and many others. Shaondip, always the supportive one, still thinks I am doing fine at engineering. I also need to appreciate the fun had with Jakub and his wife Alex, Quentin, Denisa and Matthias, and Gilberto. I also need to thank Luis for the beers had in Rotterdam. I even still have some friends in Malaga, like Cristina, Álvaro & Álvaro, Gonzalo, Gema, Ilari and Christian.

Finally, I need to thank my family, which I am lucky to have a lot of. In particular I have to thank my parents, who are still looking for ways to help me, as if my upbringing, education and life were not enough.

Que Dios os lo pague, porque yo nunca podré hacerlo.

LIST OF FIGURES

LIST OF TABLES

1

INTRODUCTION

Figure 1.1: The 'Pillars of Creation' as photographed with HST. Credit to NASA, ESA and the Hubble Heritage Team (STScI/AURA)

1.1. BACKGROUND

Since the beginning of spaceflight, the advantages of observing both the universe and Earth from orbit have been obvious. The age of spaceflight is typically considered to begin in 1957 with Sputnik 1, the first satellite in orbit. Just two years later, Explorer 6 took the first pictures of cloud cover from space. In 1960, the first satellite which was useful for weather predictions, Tiros 1, was launched. The first astronomical space telescope was the Orbiting Astronomical Observatory 2 (OAO-2) "Stargazer", launched in 1968. Many observatories have been launched since then into space, to use the privileged perspective from orbit, whether to look down at the Earth, or to look out at the universe. The most famous space telescope is the Hubble Space Telescope (HST). HST has produced some of the most spectacular pictures of elements in the universe, such as depicted in **Figure** 1.1. Whilst not achieving the fame of HST, many missions that observe the Earth supply vital data, and also pictures of out environment, such as **Figure** 1.2.

Aside from the aesthetic value of the pictures taken by these systems, their main use is providing data. Since their invention, telescopes have been the best tool of astronomers. Telescopes have got ever more powerful and delivered ever more data to support or refute theories about the origin, behaviour and ultimate fate of the universe. Arguably even more important, Earth Observation systems deliver information relevant to urban planning, the state of Earth's ecosystems, the composition of the atmosphere and the presence of natural or military threats. This data, collected regularly in time and with high data quality guides all sorts of decisions on the ground.

The targets may be observed in different wavelength regimes in order to extract different type of information, depending on the target and the purpose of the observation. For example, trace gases can be detected in the atmosphere in the wavelength range of 5 to 10 micron

Figure 1.2: Seville, Spain, and its surroundings as photographed by Sentinel 2. Credit to ESA.

(**Hundt et al., 2018**) for the purpose of detecting pollutants. The calculation of land and sea surface temperatures is aided by instruments observing the visible and infrared parts of the spectrum (**Schultz et al., 2020**), which then is introduced in climate models. Other security, health and safety applications were reviewed by (**Sobrino et al., 2016**). There are also applications using the ultraviolet part of the spectrum as described by (**Paxton et al., 2017**).

Quality of data may be defined in many different ways. In the context of Earth Observation, it may be thought of as frequent updates of the situation in a particular area of the planet, which is temporal called resolution. In other cases the interest is in capturing a lot of details, which is called spatial resolution. These two types of metrics are the main ones in the argument for deployable space optics. Other metrics of interest may be radiometric resolution, or spectral resolution, referring to the intensity of radiation at different wavelengths or at the presence of distinct components of light respectively.

The temporal resolution of a spaceborne optical system is determined by its orbital dynamics, the swath width of the instrument, and the range of its attitude control (**Li, 2021**). Observatories intended to reach high spatial resolution are placed in low Earth orbit, and the only way to influence their temporal resolution is to put more of those systems in orbit in order to fly over a given location more frequently. Spatial resolution is determined fundamentally by the phenomenon of wave diffraction. The (**Rayleigh, 1879**) criterion gives the criterion for angular resolution:

$$\theta \approx 1.22\frac{\lambda}{D}. \tag{1.1}$$

Here θ is the minimal resolvable angle, λ is the wavelength of light and D is the aperture of the entrance pupil. Examining this expression reveals that if small resolvable angles are required, the aperture of the system needs to be increased for a given observation wavelength. One of the central challenges in space instrumentation design is to increase the physical aperture of telescopes whilst being constrained by manufacturing and launcher technology.

A mind map showing the location of space instrumentation design in the wider context of spacecraft mission design is shown in **Figure** 1.3.

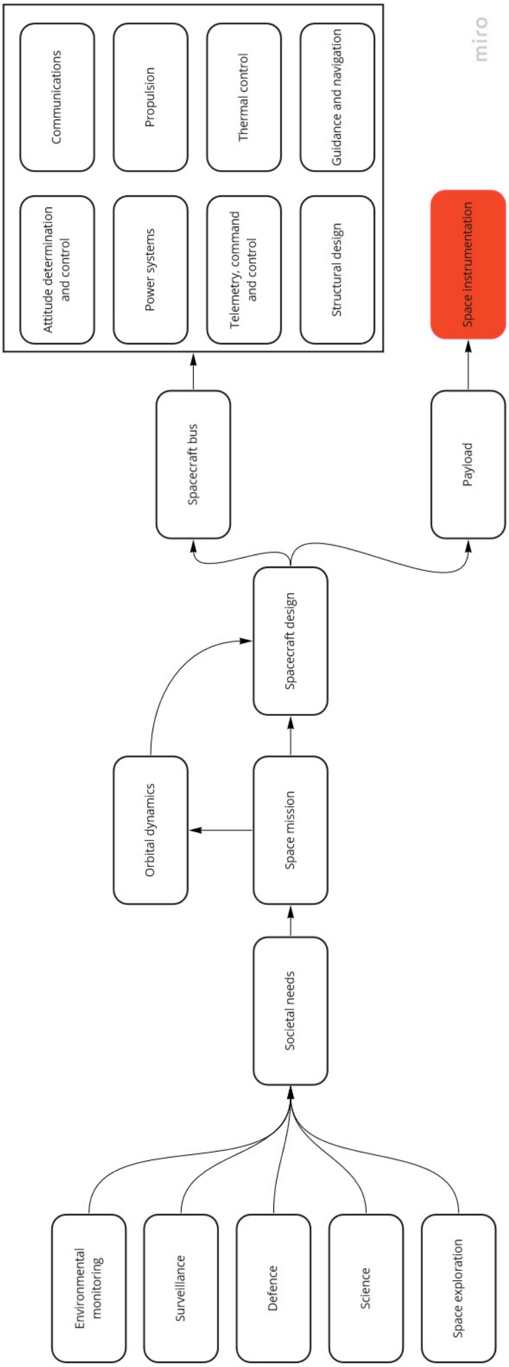

Figure 1.3: Mind map showing the global context in which space instrumentation is embedded.

1.2. CONVENTIONAL, SEGMENTED, ACTIVE AND DEPLOYABLE OPTICS

In order to increase the available aperture of telescope systems, the first idea is increasing the size of the primary optical element. To this point, no distinction has been made between refractive and reflective optics, but in this particular work, the main concerns are the properties of reflective optical elements. The main reason is that lenses are much more difficult to manufacture into the large primary aperture sizes that characterise modern telescope systems than mirrors. Refractive elements such as lenses, prisms and beam splitters may be used as elements further down the optical path. Mirrors are much easier to manufacture into larger constructions and do not suffer from chromatic aberrations (**Bely, 2003**).

Here conventional structures are understood to be those which do not rely on mechanisms to maintain high stability (**Edeson et al., 2010**). These also need to use monolithic optical elements, because precise alignment of segmented elements requires actuation mechanisms. The limits to the size of a monolithic primary mirror are related to its manufacturing and handling. (**Nelson, 2005**) A very large mirror sags during manufacturing and requires a very large vacuum chamber for deposited coatings. It is also difficult to transport, and concentrates the risk of damage into one expensive component. Costs for tooling and materials also become more expensive. The largest monolithic mirrors manufactured are the two 8.4 m segments of the Large Binocular Telescope (**Hill, 2010; Martin et al., 2006**). By comparison, the largest ground telescope under construction is the European Extremely Large Telescope, whose primary mirror is 39 m in diameter.

Conventional optics for space are limited in achievable angular resolution compared to other system architectures, but they remain the most widely used due to their relative simplicity and robustness. The use of freeform optical elements allows considerable system size reduction (**Rolland et al., 2021**) compared to traditional aspherical surfaces. Advances in athermalization of refractive systems allow the design of very compact cameras and other instruments (**Garranzo et al., 2019; Ivanov et al., 2020**). In addition, topology optimization of mirror mounts may allow further reductions in temperature sensitivity of reflective systems (**Koppen et al., 2018**).

Segmenting the primary mirror into many independent parts eases the manufacturing of very large mirrors (**Orlov et al., 2000**), but it comes at the cost of needing to 'phase' those mirror segments. Phasing is the process of aligning the mirror segments relative to each other so that they form the intended surface (**Defrère et al., 2014**). This is in order to have all segments behave like a single surface from an optics standpoint. Phasing error in optical telescopes needs to remain in the order of 10 nm, but it is dependent on the wavelength observed and the desired imaging quality. In addition, the edges between segmented mirrors add wave diffraction to the system (**Nelson, 2005**). Primary mirror segmentation also has practical limits to how large telescopes can be built on the ground, analysed by Preumont et al. (**Preumont et al., 2009**)

Active optics is a technology in which the mirrors are actuated mechanically in order to correct for disturbances to the precise relative positioning of mirror segments. Typically active optics are distinguished from adaptive optics by actuation frequency, with active optics being low frequency applications (**Hubin and Noethe,** 1993). Active optics may actively deform a mirror segment to conform to a desired shape under mechanical loads, or move the mirrors as rigid bodies to align them.

Adaptive optics are an improvement initially developed for ground-based large observatories. Adaptive optics use deformable mirror elements to correct in real time for the changes in refraction coefficient of the atmosphere, therefore bringing the system on the ground closer to diffraction-limited performance. This technology can also be used in orbit to relax the shape budgets of mirror elements under thermal or mechanical loads (**Allen et al.,** 2016**; Shi et al.,** 2015) and to correct optical aberrations introduced in coronagraph elements (**Potier et al.,** 2021). Adaptive optics have also been proposed as a risk-management tool (**Hickey et al.,** 2010), as they permit correction of disturbances found after system deployment, such as those that afflicted the Hubble Space Telescope.

Deployable optics are a system architecture in which one or more optical elements are stowed for launch in a small bundle, and then are able to deploy into a much larger shape. This has the advantage of saving space when stowed in the launcher, and potentially save launch mass (**Gooding et al.,** 2018). This thesis is an effort in investigating the mechanical engineering aspects that need to be taken into account to make deployable space telescopes a reality.

1.3. THE DELFT DEPLOYABLE SPACE TELESCOPE

The main subject guiding this thesis is a project started at the Delft University of Technology for the design of a Deployable Space Telescope (DST). This project was initiated by Kuiper, who acts as senior systems engineer (**Kuiper and Dolkens,** 2016). The DST original concept is a three mirror anastigmatic telescope with a segmented, deployable primary mirror and a deployable secondary mirror. This incarnation of the DST concept is meant to do diffraction limited imaging in the visible light, which was described by (**Dolkens et al.,** 2018). The baseline capability is a Ground Sampling Distance (GSD) of 25 cm from a 500 km orbit. An artistic impression of the concept can found in **Figure** 1.4.

More recently, due to changes in the priorities of the group, some elements of the research relate to a thermal infrared telescope (TIR) of reduced dimensions. The change to TIR has strong implications in the optical and systems design of the instrument. The main structural effect of this change is the relaxation of the wavefront error budget. This means that alignment of optical elements is easier for TIR than for the DST if diffraction limited performance is the goal.

1.4. RESEARCH QUESTIONS

The objective of this thesis is to contribute to the description and solution of the mechanical engineering challenges which arise in deployable space telescopes. The first research question is related to finding out what those challenges are.

RQ1: What are the characteristics of a deployable structure which can meet the

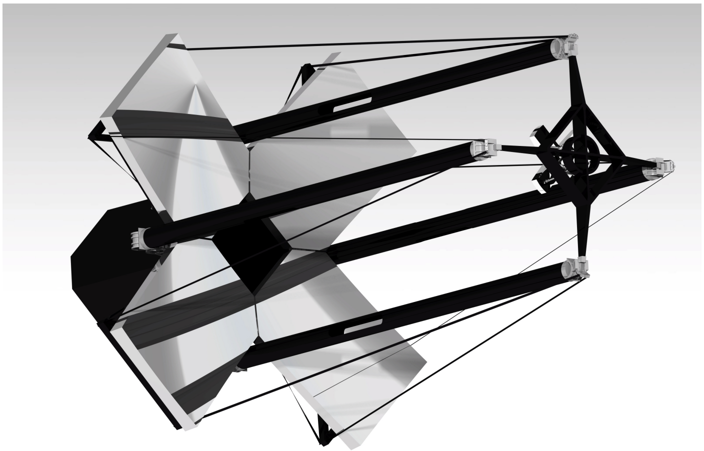

Figure 1.4: Concept of the Delft Deployable Space Telescope.

> stability, accuracy, and integrity requirements needed for space-based optical performance?

It is clear that active optics will play a role in the design of deployable space telescopes and so a very important research line in this thesis is to study the methods to design them and testing them, giving rise to research question number 2:

> **RQ2:** What are the characteristics of an active optics mechanism capable of aligning the segmented mirrors of a deployable telescope?

In order to build confidence that these design and modelling procedures used in answering the prior research questions were in accordance to the behaviour of real systems, there is also a desire to test some components. Comparing experimental results and predictions made by modelling is a good way to validate computer models.

> **RQ3:** What are the characteristics of the critical components of the DST, as derived from in-the-loop hardware testing?

The critical components which could be examined under research question 3 are the flexured frame of the primary mirror active optics mechanism, and a linear piezoelectric actuators. These were selected for experimental examination based on the results of research questions 1 and 2.

1.5. METHODOLOGY AND OUTLINE OF THIS THESIS

Chapter 2 of this thesis is meant to answer the research question number 1 in a qualitative fashion. This is done via extensive review of the available literature on deployable optics and its mechanical and thermal aspects as treated in previous projects.

Chapter 3 deals with the design aspects of active optics mechanisms, with a particular focus on designing for the Delft DST. That chapter deals with design methodology taken from other literature and applied to a design case and supported with structural finite element modelling and lumped mass thermal modelling.

Chapter 4 proposes a systematic verification and validation approach to support the models presented in **Chapter 3**. The validation approach includes experimental modal analysis and parallel computational modelling. A novel thermoelastic test methodology is introduced as part of the validation approach, which requires its own verification process.

In **Chapter 5**, a thermal test methodology for the self-heating of piezoelectric actuators is presented. This test is able to accurately reflect the operational conditions of the actuators in orbit and contributes to describe the behaviour of actuators when driven at high strokes and frequency, which is critical to define operational boundaries for active optics mechanisms.

The final chapter presents the conclusions to this research and suggested future work in the mechanical engineering issues of deployable telescopes.

A mind map summarising the disciplines covered by this thesis is shown in **Figure 1.5**. Also included are the disciplines which are necessary for complete instrument design, but not covered by this thesis.

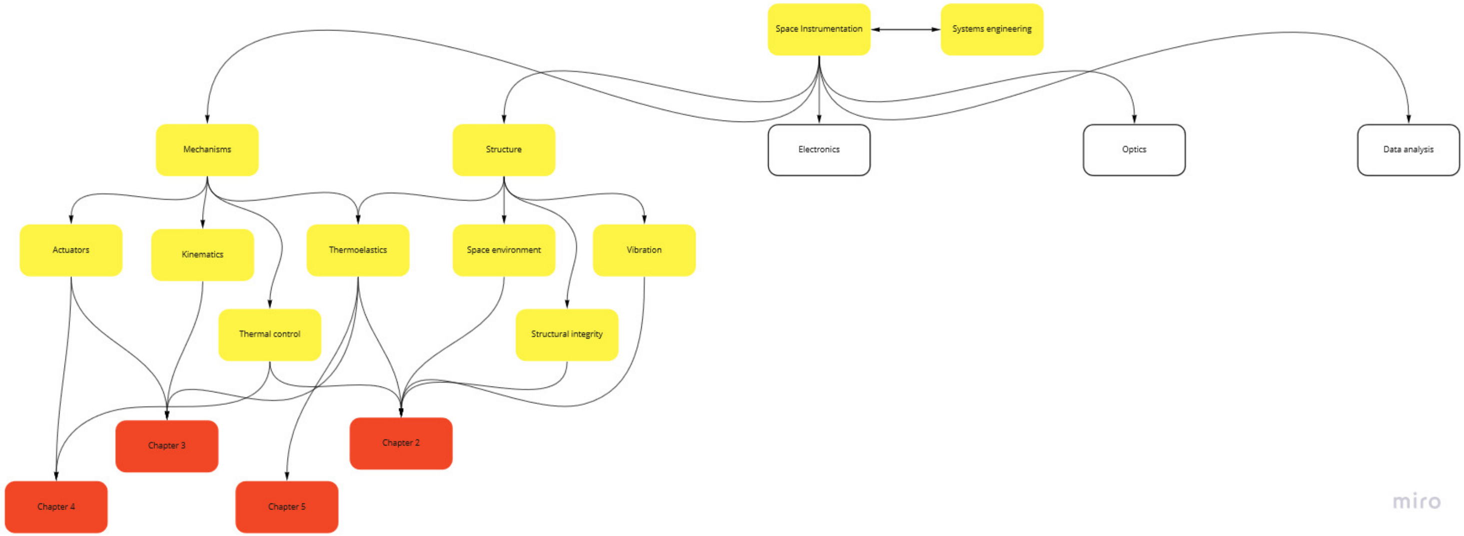

Figure 1.5: Summary of the key disciplines covered in different chapters of the thesis within instrument design.

BIBLIOGRAPHY

Allen, M. R., Kim, J. J., & Agrawal, B. N. (2016). Correction of an active space telescope mirror using a deformable mirror in a woofer-tweeter configuration. *Journal of Astronomical Telescopes, Instruments, and Systems*, *2*(2), 029001. https://doi.org/10.1117/1.jatis.2.2.029001

Bely, P. Y. (2003). *The Design and Construction of Large Optical Telescopes*. Springer.

Defrère, D., Hinz, P., Downey, E., Ashby, D., Bailey, V., Brusa, G., Christou, J., Danchi, W. C., Grenz, P., Hill, J. M., Hoffmann, W. F., Leisenring, J., Lozi, J., McMahon, T., Mennesson, B., Millan-Gabet, R., Montoya, M., Powell, K., Skemer, A., … Veillet, C. (2014). Co-phasing the Large Binocular Telescope: status and performance of LBTI/PHASECam. *Optical and Infrared Interferometry IV*, *9146*(July 2014), 914609. https://doi.org/10.1117/12.2057178

Dolkens, D., Kuiper, H., & Villalba Corbacho, V. M. (2018). The deployable telescope: a cutting-edge solution for high spatial and temporal resolved Earth observation. *Advanced Optical Technologies*, *7*(6).

Edeson, R., Aglietti, G. S., & Tatnall, A. R. (2010). Conventional stable structures for space optics: The state of the art. *Acta Astronautica*, *66*(1-2), 13–32. https://doi.org/10.1016/j.actaastro.2009.06.015

Garranzo, D., Núñez, A., Laguna, H., Belenguer, T., & de Miguel, E. (2019). APIS: the miniaturized Earth observation camera on-board OPTOS CubeSat. *Journal of Applied Remote Sensing*, *13*(03), 1. https://doi.org/10.1117/1.jrs.13.032502

Gooding, D., Richardson, G., Haslehurst, A., Smith, D., Saunders, C., Aglietti, G., Blows, R., Shore, J., Hampson, K., & Booth, M. (2018). A novel deployable telescope to facilitate a low-cost < 1m GSD video rapid-revisit small satellite constellation. *International Conference on Space Optics*, (0).

Hickey, G., Barbee, T., Ealey, M., & Redding, D. (2010). Actuated hybrid mirrors for space telescopes. *Space Telescopes and Instrumentation 2010: Optical, Infrared, and Millimeter Wave*, *7731*(August 2010), 773120. https://doi.org/10.1117/12.858217

Hill, J. M. (2010). The Large Binocular Telescope. *Applied Optics*, *49*(16), 115–122. https://doi.org/10.1364/AO.49.00D115

Hubin, N., & Noethe, L. (1993). Active Optics, Adaptive Optics, and Laser Guide Stars. *262*(November). https://doi.org/10.1126/science.262.5138.1390

Hundt, P. M., Tuzson, B., Aseev, O., Liu, C., Scheidegger, P., Looser, H., Kapsalidis, F., Shahmohammadi, M., Faist, J., & Emmenegger, L. (2018). Multi-species trace gas sensing with dual-wavelength QCLs. *Applied Physics B: Lasers and Optics*, *124*(6), 1–9. https://doi.org/10.1007/s00340-018-6977-y

Ivanov, S. E., Romanova, G. E., & Sachkov, D. Y. (2020). Optical design method for afocal achromatic systems. *Optical Engineering*, *59*(01), 1. https://doi.org/10.1117/1.oe.59.1.015105

Koppen, S., Vreugd, J. d., & Langelaar, M. (2018). Topology optimization of multicomponent optomechanical systems. (April), 885–901.

Kuiper, H., & Dolkens, D. (2016). A Deployable Telescope Concept for Sub-Meter Resolutions. *Acta Futura*, *10*, 131–144. https://doi.org/10.5281/zenodo.202244

Li, J. (o. S. S. E. C. (2021). Space Orbit Design of Remote Sensing Satellite. In J. (o. S. S. E. C. Li (Ed.), *Satellite remote sensing technologies* (pp. 27–53). Springer.

Martin, H. M., Allen, R. G., Cuerden, B., Hill, J. M., Ketelsen, D. A., Miller, S. M., Sasian, J. M., Tuell, M. T., & Warner, S. (2006). Manufacture of the second 8.4 m primary mirror for the Large Binocular Telescope. *Optomechanical Technologies for Astronomy*, *6273*(July 2006). https://doi.org/10.1117/12.672454

Nelson, J. (2005). Optics in Astrophysics. In R. Foy & F. C. Foy (Eds.). Springer.

Orlov, V. G., Cuevas, S., Garfias, F., Voitsekhovich, V. V., & Sanchez, L. J. (2000). Co-phasing of segmented mirror telescopes with curvature sensing. *Telescope Structures, Enclosures, Controls, Assembly/Integration/Validation, and Commissioning*, *4004*(August 2000). https://doi.org/10.1117/12.393930

Paxton, L. J., Schaefer, R. K., Zhang, Y., & Kil, H. (2017). Far ultraviolet instrument technology. *Journal of Geophysical Research: Space Physics*, *122*(2), 2706–2733. https://doi.org/10.1002/2016JA023578

Potier, A., Ruane, G., Chen, P., Chopra, A., Dewell, L., Juanola-Parramon, R., Nordt, A., Pueyo, L., Redding, D., Eldorado Riggs, A., & Sirbu, D. (2021). LUVOIR-ECLIPS closed-loop adaptive optics performance and contrast predictions. *SPIE Optical Engineering + Applications*, (September 2021), 50. https://doi.org/10.1117/12.2595116

Preumont, A., Bastaits, R., & Rodrigues, G. (2009). Scale effects in active optics of large segmented mirrors. *Mechatronics*, *19*(8), 1286–1293. https://doi.org/10.1016/j.mechatronics.2009.08.005

Rayleigh, L. (1879). Investigations in Optics with special reference to the Spectroscope. *Philosophical Magazine*, *8*(49).

Rolland, J. P., Davies, M. A., Suleski, T. J., Evans, C., Bauer, A., Lambropoulos, J. C., & Falaggis, K. (2021). Freeform optics for imaging. *Optica*, *8*(2), 161. https://doi.org/10.1364/optica.413762

Schultz, J. A., Hartmann, M., Heinemann, S., Janke, J., Jürgens, C., Oertel, D., Rücker, G., Thonfeld, F., & Rienow, A. (2020). DIEGO: A Multispectral Thermal Mission for Earth Observation on the International Space Station. *European Journal of Remote Sensing*, *53*(sup2), 28–38. https://doi.org/10.1080/22797254.2019.1698318

Shi, F., Balasubramanian, K., Bartos, R., Hein, R., Kern, B., Krist, J., Lam, R., Moore, D., Moore, J., Patterson, K., Poberezhskiy, I., Shields, J., Sidick, E., Tang, H., Truong, T., Wallace, K., Wang, X., & Wilson, D. (2015). SPIE Optical Engineering + Applications. *Techniques and Instrumentation for Detection of Exoplanets VII*, *9605*(September 2015), 960509. https://doi.org/10.1117/12.2188775

Sobrino, J. A., Del Frate, F., Drusch, M., Jiménez-Muñoz, J. C., Manunta, P., & Regan, A. (2016). Review of thermal infrared applications and requirements for future high-resolution sensors. *IEEE Transactions on Geoscience and Remote Sensing*, *54*(5), 2963–2972. https://doi.org/10.1109/TGRS.2015.2509179

2

THERMAL AND MECHANICAL ENGINEERING OF DEPLOYABLE SPACE TELESCOPES

If you had the time to lose
An open mind and time to choose
Would you care to take a look
Or can you read me like a book?

Iron Maiden - Caught Somewhere in Time

Deployable optics place new demands on the mechanical and thermal designs of new telescopes, essentially trading mass and volume for structural and control complexity. In this chapter, the thermal and mechanical challenges that should be taken into consideration when designing optical space systems are compiled. In addition, this chapter summarizes fourteen projects proposed to address them. Stringent deployment repeatability requirements demand low hysteresis, whereas stability requirements require high stiffness, proper thermal management, and active optics.

The content of this chapter has been published in Journal of Astronomical Telescopes, Instruments and Systems. 6(1), 289 (2020) (**Villalba et al., 2020**)

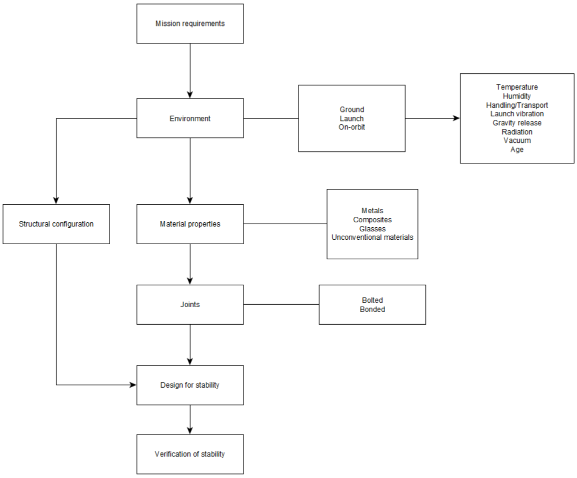

Figure 2.1: Summary chart of a review on dimensional stability of space optics. Adapted from (**Edeson et al., 2010**)

2.1. THERMO-MECHANICAL CHALLENGES IN DEPLOYABE SPACE OPTICS.

Edeson et al. (**Edeson et al., 2010**) provide a review of typical threats to geometric stability of conventional space optics. The authors of that paper refer to conventional optics as opposed to systems with active correction of degrees of freedom. These threats apply to deployable optics as well. The authors expose the physical causes of instability in general, and go on to analyse the characteristics of the materials and joints used for ultra-stable structures. Finally, the authors describe the analysis and testing procedures used to validate and verify these structures. The general flow of information in the paper by Edeson et al can be seen in **Figure 2.1**.

This section is intended to extend the description of those issues in the case of deployable optics, and include some which are specific to the new structures. Deployable telescopes, compared to typical space optics, have more deployment mechanisms with more stringent misalignment budgets and which are sources of microdynamic instability (**Lake and Hachkowski, 2000; White and Levine, 2001**). They also have longer structures only supported at their base, which means they tend to be less stiff, aggravating dynamic issues. In addition, those support structures have small thermal mass and are more exposed to external heat fluxes due to the difficulty of adding shielding or insulation. These characteristics give rise to issues in microdynamics and thermal flutter, as well as aggravate classic problems like the need for gravity off loading.

2.1.1. IMPACTS OF ATMOSPHERIC CONDITIONS

The first stage in the life of an instrument once it has been manufactured involved testing and storage on the ground. The structure of the telescope will need to be kept in conditions which mimic those encountered in space for alignment critical operations. Therefore, stability to variable ground conditions is beneficial. In addition to the standards of cleanliness inherent to any space instrument, there is the need to control for two more effects: temperature and humidity.

Thermal distortion is one of the operational challenges that will be discussed later in this chapter with more detail, though of course there is the need to maintain the stability of the test set up during alignment tests. The effect of thermal creep, particularly in materials with polymeric matrices, such as the common place carbon fibre reinforced plastics (CFRP), also needs to be taken into consideration, as heavy structures under permanent load can creep out of specifications if the storage temperature is high enough. Depending on the material, a significant fraction of this creep may be recovered (**Findley and James S. Onaran, 1978**), but it still poses a danger to the structure's repeatability.

Hygral expansion is also an important issue, since any humidity absorpted by the materials will tend to outgass in space, eliminating the swelling of the structure on the ground. This is not a major concern for metallic or ceramic materials, nor for their composites, but it can have an effect on materials with a polymeric base (**Cordero Machado et al., 2008; Krumweide, 1998**). Most assembly operations are carried out in humid air, so the components need to be coated with a moisture barrier to prevent excessive absorption. A system which is sensitive to moisture will need to receive a 'bakeout' treatment which removes this expansion prior to operations on the ground. Another mitigation technique is to store the critical components in a dry atmosphere and only getting them out for short periods for alignment operations. Note that performing a bakeout prior to alignment may be good practice, but if the structure is allowed to swell before launch, the absorbed moisture may deposit in other surfaces of the spacecraft, compromising other subsystems.

2.1.2. GRAVITY RELEASE AND TESTING PROCEDURES

Regarding their structural integrity, space structures in general can be considered to experience nearly no loads, with the notable exception of thermal loads due to temperature gradients. In deployable structures, the deployed configuration is not necessarily designed to support its own weight on Earth (**Bihl et al., 2007; Greschik and Belvin, 2007**). This forces the testing phase to use gravity offloading procedures to simulate deployment procedures and deployed-state performance. This is typically achieved by hanging the structure from several points which can move without friction parallel to the direction of the motion but compensate gravity, or supporting it with rollers on the floor.

This is true of most deployable structures such as antennas and solar panel assemblies. Optical structures are different, since they have stringent 3-D precision deployment requirements. Therefore it is important that the gravity off-load system does not overconstrain the motion of the structure. This is difficult to achieve, because gravity, being a distributed force, creates stresses within a structure supported from discrete points, which can be mitigated by adding more support points, therefore negating the principle of exact constraint. Ideally, such a system would have zero stiffness in the vertical direction, which is an emerging property of certain structural configurations. A general description of zero-stiffness mechanisms is given by (**Schenk and Guest, 2014**). Another possibility is to use a pressure-controlled flow to provide stable force output (**Han et al., 2010**).

There is an additional issue when testing the optical systems because large aperture mirrors also need to withstand their own weight during ground testing. Mirror materials, usually technical ceramics such as silicon carbide or metals, are very stiff, but the allowable surface figure error requirements during testing may pose a significant engineering challenge due to the need for special large mounts and cranes to move them around or test their performance. (**Baiocchi and Stahl, 2009**). This is an old problem and not exclusive to deployable telescopes. One of the mitigation strategies is using simulations with different mounting boundary conditions, and extracting the zero-gravity sag from the deflections resulting from pointing the mirror upwards and downwards. (**Bloemhof et al., 2009**).

2.1.3. LAUNCH AND DEPLOYMENT FAILURES

Launch is the most structurally challenging event faced by spacecraft, with the possible exceptions of in-orbit collision or re-entry. Loads experienced during transportation and handling may also be an issue with large space structures in general (**Ostrem, 1971**). Development of space structures able to withstand these loads is a wide topic and covering it is beyond the scope of this thesis. An introduction to the subject was written by (**Wijker, 2008**) . Launch vehicles manufacturers typically present four main profiles to describe the mechanical environment within the launcher: Static acceleration profile, separation Shock Response Spectrum defined in the payload adapter, sine-equivalent vibration, and acoustic vibration (**Arianespace, 2004, 2014; United Launch Alliance, 2010**). These are standard loads used in the verification procedures for all spacecraft. Loads experienced during transportation and handling may also be an issue with large space structures in general (**Ostrem, 1971**), and they must be included in the analyses.

Like other deployable elements, deployable optics are built so that the stowed state is much stiffer and stronger than the deployed configuration. Going by eigenfrequency as a criterion, launch loads typically require first eigenfrequencies in the order of 100 Hz for the structure to survive, but deployed structures typically have first bending eigenfrequencies below 1 Hz. This imposes the need for hold down and release mechanisms and alternative load paths which spare the optical elements from excessive loads. Structures typically fail due to yielding or rupture of its components, but it is advisable to keep in mind that microplasticity (**Edeson et al., 2010; Maaß and Derlet, 2017**) effects can appear well below the nominal yield stress of materials.

2.1.4. MICRODYNAMICS

Microdynamics is a term referring to a number of loosely related phenomena, all of which take place below the micro-scale threshold, a few micron characteristic size. Here the term refers to the effects of friction in joints from a purely mechanical source. Other effects which are referred to as microdynamics by other authors, such as thermal snapping, creep and microyielding are covered in other sections of this chapter (**L. Peterson and Hinkle, 2003**). This separation is adopted to clarify the causes for each phenomenon, but even in this case, several micro-scale effects are comprised in this definition. These different effects are difficult to uncouple and observe independently in experiments, and even the terminology in the literature is neither clear nor consistent in their description. An effort in this area was

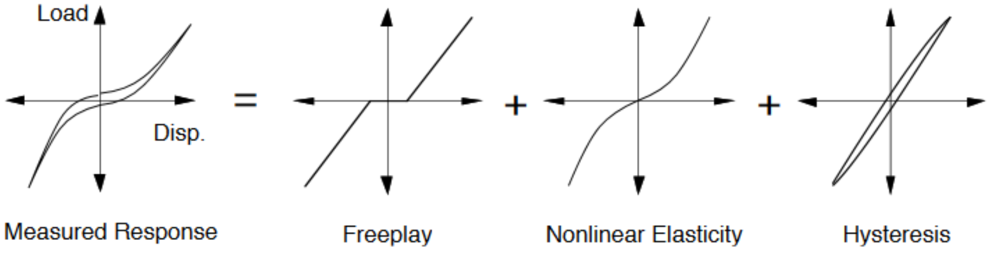

Figure 2.2: Three types of non-linear behaviour in mechanical joints. (**Lake and Hachkowski,** 2000)

presented by (**White and Levine,** 2001), who propose a framework for the analysis of microdynamic effects. The scope of their definition of microdynamics is the same as in this work.

Microdynamics are also related to structural non-linearity. Joints are known to present three essential kinds of non-linearities in their behaviour, namely freeplay, non-linear elasticity, and hysteresis. Material hysteresis and non-linear elasticity may be present in materials, but they are orders of magnitude smaller in scale for most practical materials. These effects are illustrated in **Figure** 2.2. These deviations from the ideally linear response are known to lower the eigenfrequencies of the structure respect to a linear approximation, making them significantly less stable against vibration inputs (**Ingham and Crawley,** 2001).

The microdynamics of deployable trusses have been the focus of an intense research effort in the context of developing highly stable trusses such as the one present in NuSTAR (**Stohlman and Pellegrino,** 2010). This type of joint-dominated structures experience sudden vibrations during operation which are consistent with the sudden release of energy previously lost as a result of hysteresis (**R. Hardaway and Peterson,** 2002). This is very similar to the phenomenon of thermal snapping, but can happen without the influence of a thermal load (**Levine,** 1998). Peterson (**L. Peterson and Hinkle,** 2003) also provide a rationale to lay out hysteresis requirements on large structures. For a given level of acceptable displacement, a stiffer structure is able to accommodate more hysteretic loss with acceptable stability.

The joints where these hysteretic losses occur usually rely on contact surfaces for the transmision of the deployment torque. An example of such mechanism is the ball-bearing hinge developed as part of the Origins program and presented by (**Lake et al.,** 1996). This was a joint designed to minimise non-linear responses.

Ingham (**Ingham and Crawley,** 2001) investigated the modal behaviour of another deployable truss structure. Very small strains, below 1 $\mu\epsilon$, were shown not to effect the modal shapes of the structure, therefore respecting its linear behaviour. Strains above this level however did induce a shift in the eigenfrequency and an increase in the observed damping ratio. The researchers conclude that the non-linear structural damping mechanisms in the joints do not activate for strains below this boundary. An effort to incorporate similar effects was reported by (**Coppolino et al.,** 2004), including non-linearity, stiffness uncertainty and snapping in joints. The authors created a toolbox to define properties at component level and simulate whole structures in the 100-500 Hz frequency band.

Another effect within the microdynamics classification is the so-called micro-lurching, described by (**Warren et al.,** 1999), who found that joint-dominated structures subjected to transient disturbances consistently 'lurch' to a new static position once the vibration dissipates. Repeating this event a sufficient number of times makes the structure reach an 'equilibrium zone' which was found to be extremely repeatable. This behaviour allows positioning a large deployable structure with very high repeatability by using intentional, transient disturbances. The underlying cause of this behaviour is understood to be the progressive release of residual strain energy stored at the frictional interfaces prior to the intentional excitation.

2.1.5. MICROVIBRATION

Microvibration, also referred to as jitter in the literature when it affects spacecraft attitude, is the presence of small oscillations propagating through the spacecraft structure. In most cases, these vibrations pose no threat to the survival of said structure, but they can alter pointing of the system and cause misalignment of optical components, in which case it is referred to as Wavefront Error (WFE) jitter (**Hyde et al.,** 2004). In fact this type of vibrations is widely considered as one of the largest threats to the pointing stability of optical payloads. (**Addari et al.,** 2017**; D. K. Kim,** 2014a**; Liu et al.,** 2008)

Reaction wheel assemblies are generally the largest source of vibration in most systems (**D. K. Kim,** 2014b**; Masterson et al.,** 2002). The dynamics of this phenomenon are usually modelled with an unbalanced rotor model with the first harmonic appearing at the reaction wheel speed. Subsequent harmonics, which may be of similar importance, appear as a result of other imperfections in the wheel assembly. Examples or these defects are inhomogeneity of the wheel's mass, worn or irregularly shaped bearings, stick-slip behaviour or freeplay. One may argue that friction effects are also similar or even the same as those described as 'microdynamics' in this text, but for the purposes here, the reaction wheel is a 'black box' with an output vibration signature. Magnetic bearings reaction wheels have been proposed to mitigate these problems (**Gerlach et al.,** 2006). Other sources of vibrations in spacecraft are the turbulent flow of coolant or propellant, propulsive burns, composite microcracking and any other mechanism with moving parts. Another source of jitter is micrometeoroid or orbital debris impact, which cause a transfer of momentum from the impactor to the spacecraft (**Thorpe et al.,** 2015).

In general any release of energy through vibration would fall into this category, but again sources that are specifically due to microdynamics or thermal disturbances will be treated separately in **subsections** 2.1.4 and 2.1.8.

In general, the jitter environment of an instrument will largely determine the stiffness and damping requirements of the structure. Note that both stiffness (**Kramer et al.,** 2014) and damping (**Levine and White,** 2003) of a material are temperature dependent and therefore the dynamics of the structure are subject to change depending on its operational temperature. Measurement of these properties may also require special instrumentation able to operate at extreme temperatures (**Hinkle et al.,** 2005). In practice, a stable structure is typically as stiff as required and as lightweight as possible. These conflicting requirements define the trade-off of structural design, as more stiffness requires either more load-carrying material or a more efficient use of it. However, the specific stiffness of materials or structural depth are not easily scalable with the size of the observatory (**Baiocchi and Stahl,** 2009**; L. D. Peterson and Hinkle,** 2005). Structural depth also requires either a large volume, or complex deployment mechanisms which add hysteresis and uncertainty to the deployment.

2.1.6. THERMAL CYCLING AND CREEP

Thermal effects can produce misalignment of components. This can happen in a reversible way, as is the case of thermal expansion, or irreversibly, in case of creep. Both effects are critical to the operation of space instruments. In addition to misalignment, the refractive index of lenses, beamsplitters and other refractive elements, can change as a function of temperature. Refractive elements, however, are not usually part of the optical telescope element (OTE) of deployable space instruments, which is the focus here.

The main drivers of the thermal environment of a spacecraft are the heat dissipation of its components, its injection and operational orbits, and its ability to reject or absorb radiation. A spacecraft in orbit cannot evacuate the heat it produces or receives by any other means than radiation heat exchange. Ideally, it would be possible to size and align the structure of a space optical system such that the instrument would reach radiative equilibrium with its environment at its nominal alignment. This is not possible because of the dynamic nature of heat inputs to the system and the uncertainty in its modelling.

Thermal expansion is described by the material's Coefficient of Thermal Expansion (CTE). Thermal expansion, over wide ranges of temperature, however, does not behave linearly. CTEs reported in the literature are usually specified for a certain temperature, such as ambient temperatures. This is not necessarily the operating temperature of the structure. Some telescopes have a certain temperature range required to operate, such as thermal infrared telescopes (**Fransen et al.,** 2011), whilst others are indifferent to it, but their temperature is defined primarily by their environment. Therefore, it is of primary importance to utilise the correct temperature to linearise the thermal expansion behaviour of the material. In general, thermal expansion is an undesirable effect, which makes very low CTEs desirable when choosing materials. In some cases, high CTE materials can be used for passive compensation techniques. (**Bely,** 2003)

Another effect of thermal expansion is thermal warping or bending, which is the result of the combination of thermal expansion and the uneven distribution of temperatures in a bulk component. Even if a certain component achieves perfect radiative or conductive equilibrium with its environment, there can be a temperature gradient within the material, which makes a region expand or contract more than others. This is typical of situations where a component receives heat from one side and emits it on a colder side. This induces a global bending of the component. This bending may be completely acceptable if it has been modelled and included in the design previously. However, changes to these gradients will negate this compensation. Both the magnitude and variability of these gradients are diminished by high conductivity materials for given boundary conditions. Homogeneous temperature changes also allow an easier definition of the structure's thermal centre, which may assist in the modeling stages. Materials with high thermal conductivity, which favour a homogeneous temperature distribution, are therefore desirable.

Taking these two effects into account, a coefficient of thermal warping can be defined as α/κ, with α being the materials' CTE and κ its thermal conductivity. This provides a measure of how different materials would tend to warp (**Catanzaro et al., 2000; Feinberg et al., 2012**) for a given heat transfer situation. Another figure of merit is described by (**Bely, 2003**) and defined as $\frac{\kappa}{\alpha C_p \rho}$. This parameter includes a correction for thermal diffusivity, which is the conductivity divided over material's density ρ and its specific heat C_p. This is done in order to describe how quickly the steady state is reached after a change in the boundary conditions of the thermal property. Note the behaviour of this parameter is inverse to the aforementioned coefficient of thermal warping.

A high thermal diffusivity and therefore fast response to thermal variation may not be desirable if the system is designed to be heavily damped through the use of a large thermal mass or latent heat storage. In that case, these compound figures of merit for a material may have their meaning inverted, or may be ignored. However, use of high thermal mass systems typically imply larger inertial mass and volume, partially negating the benefits of deployable systems in space applications. A compromise solution may be found in the use of phase-change materials, which allow additional heat to be used in a reversible phase transition without the need for a large mass (**Elgafy et al., 2004**).

2.1.7. THERMAL FLUTTER

Thermal flutter can be understood as a dynamic effect caused by cycles of thermal warping, exciting vibration modes of the system. The Hubble Space Telescope famously experienced a disturbance in its pointing whenever undergoing eclipse due to quick heating and deformation of the deployable solar panels, which excited structural modes (**Foster et al., 1995; Thornton and Kim, 1993**). Deployable optics, as discussed in subsection 2.1.3, tend to have lower eigenfrequencies, possibly by two orders of magnitude, and to be more exposed to thermal fluxes than traditional monolithic telescopes which are encased in rigid bodies. A way to mitigate this effect is keeping heat fluxes steady by means of a thermal shield or particular orbit selection, or diminishing the aforementioned effects of thermal expansion. For missions which orbit Lagrange points, the solar heat flux remains constant and therefore flutter is not a concern. Thermal flutter can affect the pointing stability of instruments or cause instability of the optical system itself, introducing wavefront jitter.

The overall phenomenon can be explained with a boom exposed to solar fluxes. Limited thermal conductivity will establish a steep temperature difference between the exposed and shaded sides, which causes the former to expand more than the latter. If the process can be regarded as quasistatic, no dynamic effect will occur. However, booms might be poorly insulated and have small thermal inertia, in addition to low eigenfrequencies. Boley (**Boley, 1972**) proposed that the coupling between thermal fluxes and vibration modes may be assessed through the parameter:

$$B = \frac{t_T}{t_M} \tag{2.1}$$

where t_T is the characteristic thermal time and t_M is a characteristic time of the dynamic response, usually the inverse of the first natural frequency of the system. A way to assess this effect is to consider the amplification factor:

$$R = 1 + \frac{1}{\sqrt{1+B^2}} \tag{2.2}$$

which provides a magnitude of the dynamic effect compared to the quasistatic case. This classical approach has been cited as adequate for engineering purposes (**Kawamura et al., 2008**), but also extended to other situations such as functionally graded beams (**Malik and Kadoli, 2018**) or plates (**Alipour et al., 2016**).

2.1.8. THERMAL CREAKING

The other major coupled effect is referred to in the literature as thermal creaking or snapping. This refers to differential heating of contact interfaces causing a vibration, as stresses built up at the interface are violently released.

Kim (**Y. A. Kim, 1998**) studied the interaction between this phenomenon and the dynamics of spacecraft. This phenomenon happens primarily in the joints of deployable structures due to the presence of contact interfaces. In essence, the energy release mechanisms are the same as described in the 'Microdynamics' section, but the driver of the stress accumulation is the constrained thermal expansion. In terms of mitigation, the same recommendations as exposed in **section 2.1.4** apply.

Since differential thermal expansion is the driver of this phenomenon, limiting the temperature difference across a contact interface with the same materials on both elements, can prevent slippage. This, however, is not easily achieved in mechanisms with non-conforming contact, as it is usually the contact itself that acts as a thermal interface. These contact interfaces in precision applications usually rely on point or line contacts (**Hale and Slocum, 2001**), which minimises the effective thermal contact area. At contact interfaces which have different materials, the CTE mismatch between them will drive slippage proportional to a bulk temperature change of the whole joint, even if the temperatures across the interface are the same.

2.2. STATE OF THE ART IN DEPLOYABLE SPACE OPTICS

In this section, proposed systems implementing deployable space optics are summarised. Special attention is given to their thermal and mechanical description. This will bring insight as to the level of maturity of the project, and the focus of its researchers. There is a great diversity in both the characteristics and maturity of these projects, some of which are complex design exercises. Others have been developed to completion or have prospects of doing so.

In this section, the observatories have been categorised on three classes, namely the L2 observatories, the LEO telescopes deploying along its optical axis, and the LEO telescopes which deploy their primary mirror. No observatories have been proposed in higher Earth orbits, moon orbits or heliocentric orbits. From a mechanical perspective, these other locations negate the advantage of LEO for EO purposes, and diminish the advantages of L2 for astronomy, without foreseeable benefit. This also points to an increasing diversification in the topology of space optics missions.

2.2.1. LARGE LAGRANGE POINT 2 OBSERVATORIES

The L2 observatories are missions which employ telescopes that do not fit in existing launchers, and orbit the second Sun-Earth Lagrange point. Their mission is to look into the universe for a number of scientific enquiries. They have the largest aperture sizes, which need to be deployed in order to fit the launcher, and the largest focal length, which is also deployed. Two such missions are present in the literature: The James Webb Space Telescope (JWST) and the Large Ultravioler and Infrarred Surveryor (LUVOIR). Their thermal environment in L2 is stable save for fluctuations in solar output, which eliminates concerns of thermal flutter and mitigates temperature variations. The large structures of these missions and their use of many mirror segments, however exacerbate wavefront stability challenges. Their stringent WFE budget, resulting directly from the scientific requirements, impose the need for more complicated alignment and vibration isolation mechanisms. Due to their complexity and institutional support, these are the most well-documented and extensively researched projects reported so far in the literature.

In these missions, microdynamics are a major concern due to the large number of interfaces, joints and latches involved and much of the knowledge presented in **section** 2.1.4 is derived directly from investigations performed to develop JWST.

JAMES WEBB SPACE TELESCOPE

The JWST is the largest and most complex deployable optics instrument built so far. Here, a summary of the key thermomechanical elements of its OTE is presented. JWST is will operate in orbit around the second Earth-Sun Lagrange point (L2). This provides a stable thermal environment compared to the eclipse cycles which occur in orbit around Earth. **Figure** 2.3 shows an exploded view of the JWST's OTE plus the integrated science module and the thermal management system, and a schematic of the sunshield.

Optical design: JWST is a three-mirror anastigmat (TMA) with a segmented and actuated primary mirror (M1), 6.5 m across, an actuated secondary (M2), and a fast steering mirror incorporated in the exit pupil for line-of-sight disturbance correction. The dimensions of the primary mirror and the sunshield exceed those of the largest launchers in the market. The telescope observes at visible and infrared wavelengths, being diffraction limited at 2 μm. The need for operating wavelengths in the thermal infrared range also imposes operational temperatures in the order of 40-60 K, to prevent emissions from the telescope from affecting the signal.

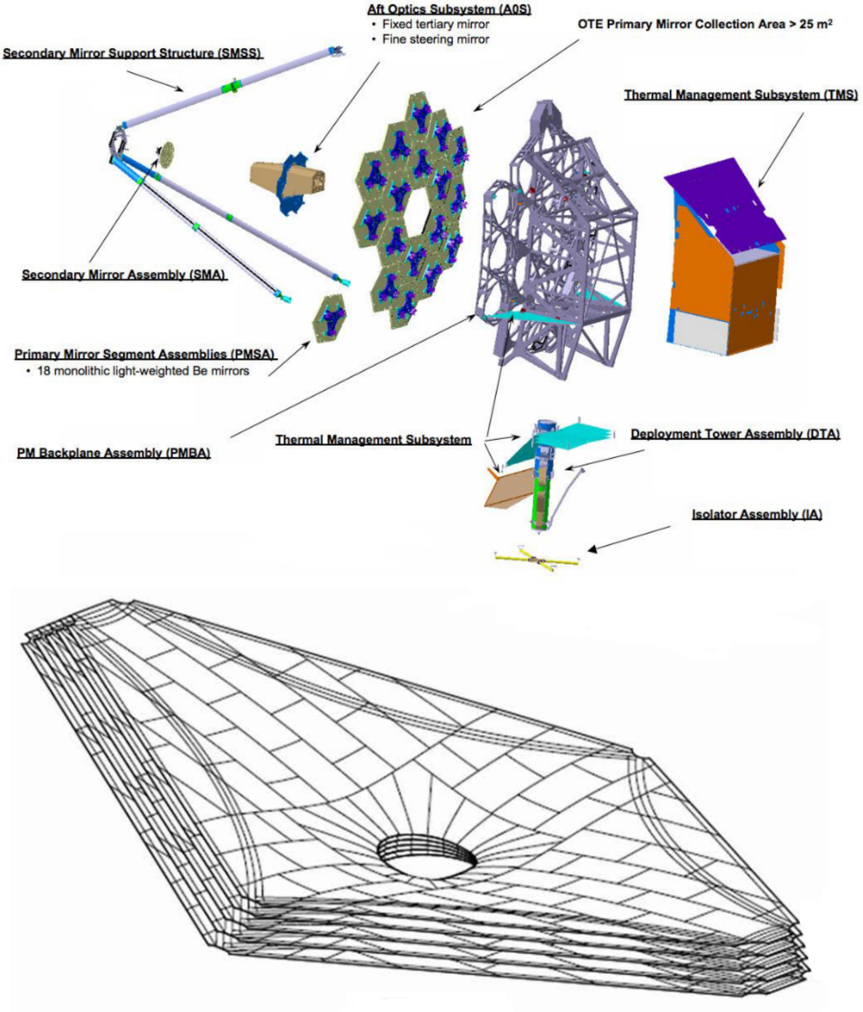

Figure 2.3: Top: Exploded view of the main elements of JWST, including the integrated science module and the thermal management unit (**Gallagher et al., 2018**). Bottom: Schematic of JWST's sunshield (**J. Arenberg et al., 2016**)

Describing JWST or any of its subsystems in full is well beyond the scope of this thesis. A wealth of information can be found in the literature. (**Howard, 2004, 2007a, 2007b; Howard and Feinberg, 2009; Howard and Ha, 2004; Howard et al., 2008**) describe in more the optical design and the linear optical model developed to run Structural Thermal Optical Performance (STOP) analysis on it (Hyde et al., 2004; Johnston et al., 2004). A summary of these papers was published in 2011 (**Howard, 2011**) Here the most relevant aspects of its design will be outlined: Mirror technology, deployment mechanisms, fine actuation mechanism, and the sunshield.

Mirror technology: The JWST mirrors are made of Beryllium O-30-H (**Stahl et al., 2004**). Whilst beryllium has a relatively poor thermal stability at ambient temperatures, its total thermal expansion is very small when cooled to JWST's cryogenic operational temperatures. It is also very lightweight, strong, and has good thermal conductivity compared to other optical materials. Material was removed from the mirror cores to produce a rib structure that is both lightweight and stiff. When compared with the competing material Ultra Low Expansion glass (ULE), Beryllium was selected for its superior technical properties. This decision was made despite the fact that Berylium posed higher risks of production delays and cost overruns (**Stahl et al., 2004**).

Deployment mechanism: The segmented mirrors are mounted in a central, static frame, and two "wings" which have to deploy over a 103-degree angle and latch in place, powered by a stepper motor. Both the fixed and mobile frames are made of carbon fibre composites, specifically tuned for thermal stability through manipulation of the material CTE (**Lightsey et al., 2012**). This is done in order to minimise temperature dependence of the final positions of the mirrors. The development team observed the principles previously laid out to avoid microdynamics response. Non-conforming interfaces were used to avoid any load transfer through friction and subsequent microslippage. However, stiffness requirements for some interfaces made it necessary to add redundant non-conforming contacts, or oversized friction joints (**Reynolds et al., 2004**).

Actuation mechanism: Deployment repeatability requirements for this system from the launch 'stowed' position to the nominally deployed operational position, are in the order of a few milimetres (**Reynolds et al., 2004**). This is a very large error compared to the allowable WFE in practice. The mirror positioning is corrected by the actuation mechanism down to a step size smaller than 10 nm. This is achieved through the use of a 2-stage actuation mechanism, with a coarse range of 20 and a fine range of 2 microns. The actuators are mounted on a beryllium delta frame, and interface with the mirror in a hexapod configuration which provides 6DOF position control. An additional actuator, coupled to beryllium struts, also provides radius of curvature correction. (**Warden, 2006**) The overall control architecture is described by (**Knight et al., 2012**). The actuators are powered by a so-called gear motor, composed of a stepper motor, a resolver and a gear head. The bearings in the motor are a limited lifetime item, sized for the expected mission lifetime (**Gallagher et al., 2018**).

Sunshield: Passive cooling of the JWST's OTE will be achieved mainly through the use of a large, deployable sunshield, shown in **Figure 2.3**, which stands between the Sun and the OTIS, which is the OTE plus the Integrated Science module. The sunshield is composed of five layers of Kapton E with a vapour deposited aluminium (VDA) coating on their inner faces. In the outer faces, the two outer layers are coated with a Silicon optical solar reflector coating, and the three inner faces with the same VDA. The layers are arranged with a dihedral angle which allows radial rejection of heat both from the spacecraft and from sunlight (**J. Arenberg et al., 2016**). The sunshield is intended to receive roughly 300 kW of thermal power on its hot side, but let less than 0.05 W pass on to the cold side (**Waldie and Gilman, 2004**). The sunshield is deployed via four hinged booms and two additional telescopic booms. These six booms are attached to tensioning mechanisms which are in charge of separating and stretching the different layers of the shield to its designated geometry.

LARGE ULTRAVIOLET OPTICAL INFRARED SURVEYOR

LUVOIR is not, strictly speaking, a definite project, but rather a response to the call for proposals initiated by NASA as part of its decadal survey on astronomy missions. The concept of LUVOIR has been embodied in several evolving proposals, most notably the Advanced Technology Large-Aperture Space Telescope (ATLAST) and the High-Definition Space Telescope (HDST) (**Bolcar et al., 2016**). At the same time, LUVOIR is one of the competing proposals for the next large observatory, alongside the Origins Space Telescope (OST), Habitable Exoplanet Imaging Mission (HabEx), and the Lynx X-ray Observatory. Of these concepts, only LUVOIR has seen extensive development in the direction of a segmented-aperture deployable architecture like that of the JWST. However,a concept for a smaller version of HabEx called HabEx Lite was proposed (**Redding et al., 2018**) featuring a segmented, but non-deployable primary mirror.

LUVOIR has been proposed in different formats, including one featuring a monolithic 8 metre primary mirror. However, most of the proposals follow the trend towards a segmented aperture reminiscent of that of JWST, but substantially larger. This would allow to employ the lessons learned during development of JWST, but also tightens the alignment requirements by a factor of approximately 4 based on a diffraction limit at 500 nm (**Baiocchi and Stahl, 2009**). Proposals exist for primary mirrors of sizes 9.2 m, 11.7 m and 16.8 m (**Tupper Hyde and Postman, 2010**) Any of these proposals exceeds the total diameter of any current launcher fairing. The latest report available (**TEAM, 2019**) further develops a 15 m aperture concept as LUVOIR-A which can be seen in **Figure 2.4**. Another possible architecture described in that report, LUVOIR-B, is based on an 8 m primary aperture, off-axis telescope

As its name implies, this telescope would operate primarily in the optical range, with capabilities in UV and shortwave IR, therefore being a true successor to the Hubble Space Telescope. This means that it would be a "warm" telescope, without the need to create a cryogenic environment. Even so, operation of this telescope will require launching it into an orbit about the L2 Lagrange point, and a large sunshade to prevent sunlight from affecting the measurements. The requirements for this sunshade are likely to be simpler than those of JWST's sunshield (**J. W. Arenberg et al., 2018**).

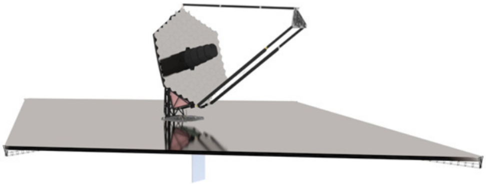

Figure 2.4: LUVOIR-A conceptual architecture. (**Team,** 2018)

The architecture for the current LUVOIR-A concept consists of a 120 segments primary mirror aperture, with all segments controlled in 6DOFs. The use of ULE segments in a closed back structure make these segments stiffer than their JWST predecessors, and so the shape actuator can be dropped (**Team,** 2018). Like in JWST, a fine steering mirror would provide line of sight correction. LUVOIR-B is an off axis three mirror anastigmatic telescope with 55 mirror segments, also controlled in 6DOFs. The deployment mechanisms of either concept are broadly based on the 'wings'

In addition to controlling the rigid body motions of the primary mirror segments and the secondary mirror, LUVOIR is also meant to control the temperature of each individual segment via the use of heater and diffuser plates mounted behind each segment (**Eisenhower et al.,** 2015).

2.2.2. EARTH-ORBITING OBSERVATORIES DEPLOYING ALONG OPTICAL AXIS

These are small satellites intended to deploy an element along its main axis with the intention of achieving longer focal lengths than would otherwise be possible in a constrained space. However, not deploying the primary aperture, the achievable aperture and therefore achievable image quality is limited. This can be mitigated by having these instruments fly on very low altitudes, which makes their service life limited.

This is the simplest possibility for deployment and it has attracted interest from companies and universities because it is potentially the cheapest and fastest technology for development purposes. From a mechanical perspective, these configurations suffer from low eigenfrequencies in the bending of elements along the optical axis. This makes it difficult to keep the alignment of the main optical elements and precisely control their attitude. However, not having a segmented aperture, these systems would not need to cope with wavefront stability issues due to alignment of mirror segments. This architecture also simplifies the design process of a baffle for straylight and thermal control, which can be simply attached to the deployable element. The reduced amount of deployment mechanisms also reduce the induced microdynamic instabilities.

DOBSON SPACE TELESCOPE

Another project which saw development during the 2000s was the Dobson Space Telescope (DoST), by a team of researches at TU Berlin. This project was reported on by (**Segert et al.,** 2006; **Segert et al.,** n.d.). They claimed VHR capabilities from a microsat platform flying at 550 km, and dual EO and Near Earth Object observation purposes. The primary mirror

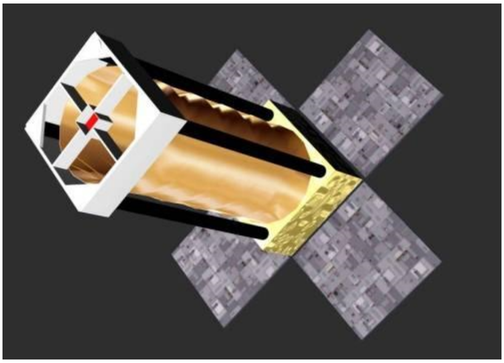

Figure 2.5: Artist impression of the deployed DoST (**EOPortal,** n.d.).

aperture was of 0.5 m for its baseline mission. The operational wavelength is not detailed in the documents, but it is understood to cover the visible range. The project was reported on over a series of papers, including several experimental set ups and a tentative launch date in 2012. The members of the team moved on to create the startup Berlin Space Technologies GmbH which aimed to take the project to the market, but the company does not list deployable telescopes as part of their product line. The project was eventually discontinued because it was not deemed commercially viable.

In the case of the DoST architecture, only the secondary mirror is stowed for launch and deployed in orbit. This allows for a longer focal length with a significant reduction in size, at least in one dimension. The deployment is achieved with a rigid deployable truss which pushes the secondary mirror 1.1 m away from its stowed position, though this mechanism is not explained in detail. The fact that there is no segmented aperture makes misalignment much less critical. The DoST implements an active optics strategy with a 6DOF actuated secondary mirror. A baffle incorporated in the secondary mirror structure also provides cover for the primary mirror, and the active optics mechanism is expected to bring the errors due to deployment repeatability and thermal expansion from 1 mm to 1 micron. The DoST concept is shown in **Figure** 2.5.

COLLAPSIBLE SPACE TELESCOPE

Yet another project for deployable optics can be found in the Collapsible Space Telescope (CST) project, a proposal for a deployable secondary mirror mounted on a coiled mast (**Agasid et al.,** 2013). The operational wavelength of this telescope is not detailed, other than covering the visible range. A baseline primary aperture of 152.2 mm was proposed to fly at an altitude of 250 km. The overall architecture of this system is similar to that of the DoST and shown in **Figure** 2.6. Once released, the strain energy stored in the coils pushes the secondary mirror away from the primary. This technique does not affect the aperture of the entrance pupil and therefore does not increase the achievable diffraction limited resolution, but makes integration of a baffle easy and dramatically increases the achievable focal length. This project is scarcely reported and does not have any continuation beyond the original paper, which is a valid conceptual design case, but lacks sufficient analysis to

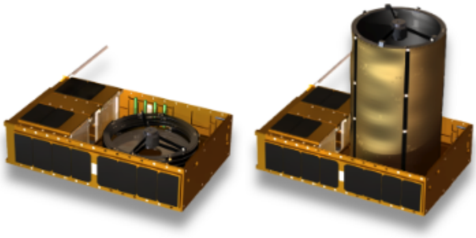

Figure 2.6: Collapsible Space Telescope concept, showing the deployment sequence. (**Agasid et al., 2013**)

Figure 2.7: Concept of the SSTL telescopic deployment barrel. (**Gooding et al., 2018**)

back up its feasibility.

SSTL DEPLOYABLE TELESCOPE

Surrey Satellite Technologies Limited (SSTL) proposed a telescopic optical barrel, shown in **Figure 2.7** coupled to the secondary mirror of a Cassegrain telescope.The system performs at a GSD of 1 m and is built upon heritage of SSTL's Carbonite-2 satellite, but with a deployable secondary mirror. This is estimated to lower the volume requirements of each system inside the launcher fairing, therefore allowing for more deployments with less launches. Gooding (**Gooding et al., 2018**) proposes a case study with a 500 km baseline orbit, though no details of operational wavelength, focal length, or primary aperture are provided.

The secondary mirror is spherical, which restricts the alignment procedure to a three DOF kinematic problem. The same optical barrel used to deploy the secondary mirror provides protection for the primary mirror and is a straylight management tool. The barrel deployment is powered by a motor which drives a lead screw per barrel section into a V groove. The primary mirror is monolithic, so the maximum aperture is still limited by the available volume within the fairing. The focal length however can be drastically increased similarly to that of the CST and the DoST.

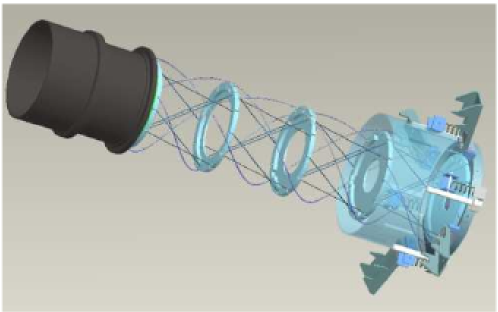

Figure 2.8: Schematic of PRISM, showing the coil booms which push the focusing lens away. The baffle is omitted.(**Komatsu and Nakasuka, 2008**)

PICOSATELLITE FOR REMOTE SENSING AND INNOVATIVE SPACE MISSIONS

The Japanese Picosatellite for Remote Sensing and Innovative Space Missions (PRISM) (**Komatsu and Nakasuka, 2008**) is, to the best of the author's knowledge, the only deployable optics spacecraft whose launch has been confirmed. It was successfully inserted in a 660 km circular orbit in 2008, as a technology demonstrator for a nanosatellite class imager. Unlike all other examples cited herein, PRISM is a refractive system with an aperture of 90 mm. (**Komatsu and Nakasuka, 2008**) The overall system is shown in **Figure** 2.8.

The optical system is pushed away from the main instrument housing by means of a collapsible boom, similar to the mechanism described in the case of the CST (**Sato et al., 2008**). This allows the system to achieve a much longer focal length that would otherwise be possible. The coils are also used to pull a baffle which provides straylight control and a degree of thermal protection to the structure. The detector array is mounted in a focusing mechanism which can adjust its position to correct for focus errors caused by the flexible deployable structure (**Komatsu and Nakasuka, 2008**). The low stiffness structure made special correction of its line of sight jitter necessary (**Inamori et al., 2013**), but successful imaging with 30 m GSD was achieved.

2.2.3. EARTH-ORBITING OBSERVATORIES WITH SEGMENTED APERTURES

These systems are proposed to deploy the primary mirror, and may or may not deploy the secondary mirror. In this way they can increase both the focal length and the aperture of the optical system beyond what is achievable with a conventional telescope of the same size. They are also smaller than the L2 observatories, although eclipses are present in their thermal environment. The alignment of primary mirror segments is therefore critical, and disturbances are frequent. The solution is generally the use of active optics mechanisms which constantly correct the alignment.

The challenges of telescopes which only deploy along their optical axis also apply here, but they are aggravated by the difficulty to integrate a baffle to mitigate the large amounts of straylight from albedo originated outside of the field of view and the thermal influence of the solar flux.

LARGE APERTURE TELESCOPE TECHNOLOGY

The Large Aperture Telescope Technology (LATT) project is reported by Marchi et al. (2008) in several papers. Its purpose was described by Hallibert and Marchi as pushing the critical Technology Readiness Level (TRL) level of large active mirrors, taking advantage of existing experience with active secondary mirrors for ground-based observatories (**Hallibert and Zuccaro Marchi, 2016**). The project was finalised in 2015, considering the technology for large-aperture active mirrors to be TRL 5 under the European Space Agency standard.

LATT proposed a design of an afocal telescope with 4 metres of aperture diameter to take Differential Absorption Lidar measurements around the 935 nm wavelength. Unlike the rest of the telescopes mentioned herein, this telescope's purpose is not imaging, and it doesn't operate within the visible spectrum. (**Simonetti et al., 2010**) The design featured a segmented primary mirror with active segments made with a CFRP core and a thin sheet of zerodur. A novel feature of the design is the use of voice coil actuators to correct the shape of the large aperture mirror. In addition, electro-static locking is proposed as a means of holding the thin sheet to the substrate, providing a strong load-path to resist launch loads.

The deployment of these mirrors relies on elastic memory composite (EMC) hinges. The authors proposed that the error inherent to this technology could be compensated by means of the actuators. In addition, the design featured an inflatable baffle which covered the entire system in order to prevent straylight from falling in the detector (**Simonetti et al., 2010**). The complete concept can be seen in **Figure 2.9**. An alternative design proposed by (**Thompson et al., 2010**).

Its purpose was to push the critical Technology Readiness Levels (TRL) for a near infrared, very large aperture telescope. Their progress reports a very lightweight active mirror, and an optical design featuring an 7 m^2, deployable collection area. Though some of the technical requirements of this project have been published, there is no publicly available information about its phasing budget. Details on its operational orbit are not explicitly reported, though calculations for straylight reported by (**Mazzinghi et al., 2006**) point to a 450 km altitude.

DEPLOYABLE PETAL TELESCOPE

Utah State University's Space Dynamics Lab built and tested the so-called Deployable Petal Telescope (DPT) (**Champagne et al., 2014**). A Cassegrain telescope which can be mounted on a 3-U CubeSat platform, deploying both its primary and secondary mirrors. This endeavour however is scarcely reported on the literature, so actual feasibility and performance of the system is difficult to ascertain. A video is still available online, in which the primary mirror segments are seen to unfold in a flower-like fashion, whilst the secondary mirror, mounted on a rail, deploys away from the instrument housing.

The DPT is a Cassegrain-type telescope with a 200 mm aperture, deployable segmented primary mirror, which unfolds in a similar fashion to flower petals. The prototype mirror is a smaller version and has flat sections at the tip to aid in alignment, which makes its effective aperture smaller. The secondary mirror is mounted on a rail, which linearly extends away from the primary. Both mechanisms are described to be fully passive via a spring

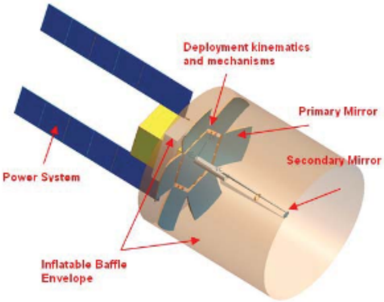

Figure 2.9: System architecture of the LATT baseline telescope, showing the cylindrical baffle. (D'Amato et al., 2017)

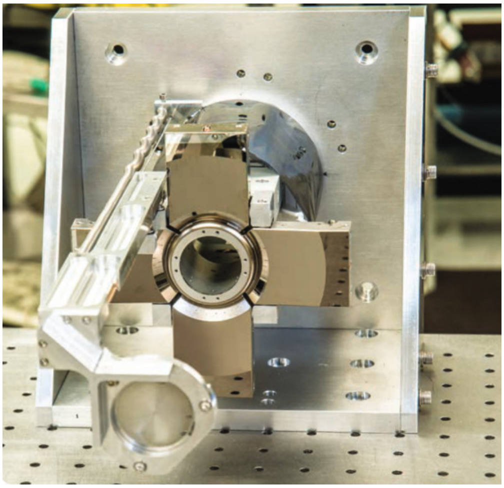

Figure 2.10: Picture of the DPT test set up, not including the internal baffles. (**Farrah et al., 2017**)

load. The conceptual imaging system is diffraction limited at 632.8 nm, achieving a 1.3 GSD from a 500 km orbital altitude. In the architecture reported by Champagne et al. there are no external baffles, but a collapsible baffle is installed in the space between the two mirrors (**Champagne et al., 2014**). This would mean the telescope is largely exposed to heat fluxes from the Sun. Unlike most of the other deployable telescopes, the DPT does not implement an active optics mechanism to correct for misalignment or non-repeatability. The authors trust the assembly to be stable enough in 5 DOFs, excluding the tip motion, which is adjusted through a mechanism attached to the back of the mirror. This mechanism was tested for deployment repeatability and the results showed that most of the surface error resulted from the individual segments, which the authors expected could be improved. The test setup for the DPT is shown in **Figure 2.10**.

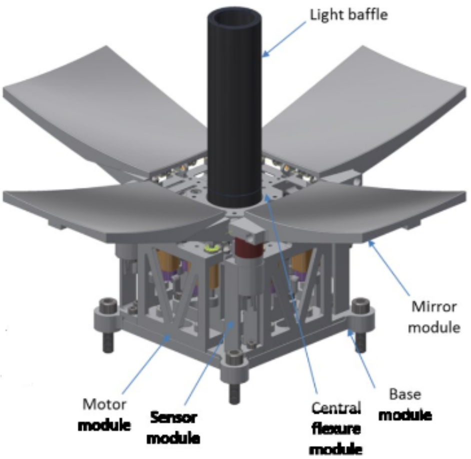

Figure 2.11: Schematic of the adjustment mechanism of the deployable telescope proposed by Schwartz et al. showing an additional internal baffle (**Schwartz et al., 2016**).

DEPLOYABLE SPACE TELESCOPE (UK ASTRONOMY TECHNOLOGY CENTRE)

A more recent attempt to use CubeSats for VHR EO is reported by (**Schwartz et al., 2016**). The purpose of this project is to reach a 39 cm Ground Sampling Distance from a CubeSat platform flying at 350 km altitude. This system is diffraction limited at 550 nm and has a 300 mm aperture. The authors provide quantified measures of the sensitivity to misalignment of the system and propose an active optics actuation system to align the mirrors within the tolerances. The necessary metrology proposed is a sharpness optimisation algorithm, which drives the active optics. The system can fit in a 1.5U CubeSat standard unit. The authors do not describe yet the sensitivity of their concept to thermoelastic deformation as a result of the orbital transients.

The primary mirror active optics acts in tip-tilt and piston directions. Three motors are coupled to the mirror by means of a flexure system connected to a steel shaft. This shaft acts as the connection to the mirror substrate, and also integrates a torsion spring which powers the deployment. The active optics strategy is able to obtain a surface error of 25 nm under laboratory conditions (**Schwartz et al., 2018**). The authors do not report on a particular deployment strategy for the secondary mirror. In the latest design, shown in **Figure 2.11**, a baffle is included in between the primary and secondary mirrors for straylight attenuation, which seems to leave the telescope exposed to thermal fluxes like in the DPT case.

DEPLOYABLE SPACE TELESCOPE (TU DELFT)

The TU Delft Deployable Space Telescope (DST) project was proposed by Kuiper in 2012 and has been running ever since. Dolkens proposed the optical design and a ray-tracing tool to assess its performance. From that, the top-down misalignment budgets were derived and presented in (Dolkens et al., 2019). In addition to the optical analysis, several Master of Science theses have been published by the TU Delft (**Corvers, 2018; Krikken,**

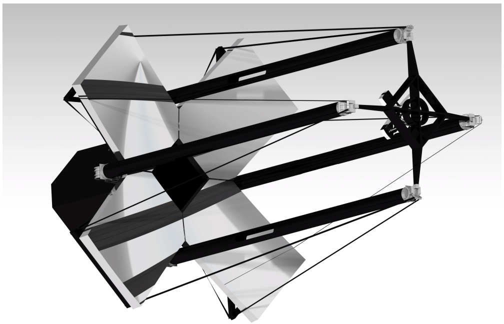

Figure 2.12: The TU Delft deployable space telescope.

2018; **Lopes Barreto,** 2017; **Pepper,** 2018; **Voorn,** 2018), detailing the evolution of the mechanical design from the first iteration by Dolkens to the latest developments reported by Dolkens et al. (**Dolkens et al.,** 2018).

The DST, shown in **Figure** 3.1 is a three-mirror anastigmat telescope with a four-segment primary mirror of 1.5 m aperture, diffraction limited at 550 nm and flying at 500 km altitude. These segments are actuated in piston and tip-tilt directions, which are regularly identified as the most critical DOFs in both this and other proposals. Aberrations caused by warping of the mirror shape are corrected by a deformable mirror installed in the exit pupil of the OTE. This deformable mirror, however, cannot correct for the wavefront error caused by a dephasing of the primary mirror. This misalignment is controlled by means of a so-called PistonCam, installed in the intermediate image plane, tracking the sharpness of the image at the mirror edges. This information is fed to a control algorithm which drives the active optics mechanism.

The mechanical design includes a baffle capable of limiting the variability in the thermal environment, and a low hysteresis compliant rolling element hinges, so as to comply with the guidelines presented in section 2 (**Krikken,** 2018; **Voorn,** 2018). This active optics mechanism was proposed by Pepper (**Pepper,** 2018). In addition to providing exact constraint and actuation of the mirror substrate to its support plate, the active optics actuator acts as a primary load path holding the mirror through launch with acceptable strength margins. The mechanism consists of four actuators in push-pull configuration which move an intermediate plate. This intermediate plate is in turn constrained by means of a hexapod mount to the mirror substrate.

Successful operation of the system relies on three layers of increasingly strict tolerances (**Dolkens et al.,** 2019). The deployment mechanism shall be accurate enough to reach a coarse alignment in the micron range. The system is then actuated to a nominal position in the order of $\lambda/20$, with short WFE jitter disturbances kept below the order of $\lambda/100$, with λ being the diffraction limited wavelength of the telescope. A deployable structure able to meet these requirements taking into consideration all the effects mentioned in this chapter and that of (**Edeson et al.,** 2010) is currently under development.

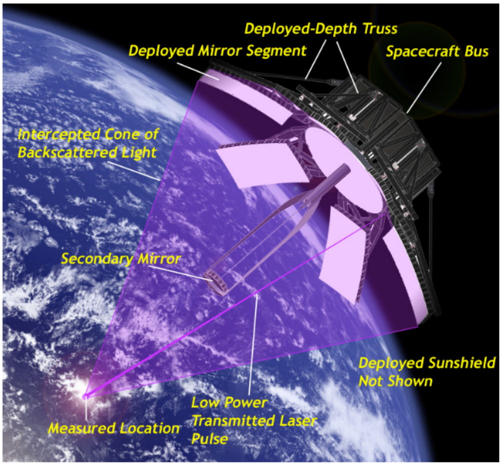

Figure 2.13: Artist impression of the Lidar telescope which was used as baseline by the DOME project (**L. D. Peterson et al., 2007**)

DEPLOYABLE OPTICS MODEL EXPERIMENT

The Deployable Optics Model Experiment (DOME), reported by Peterson and Hinkle was a structural mechanics experiment related to a concept Differential Absorption Lidar deployable telescope based on the requirements for the Ozone Research through Advanced Cooperative Lidar Experiments (ORACLE) mission (**Lake et al., 1997; Lake et al., 1999**). The baseline design was a segmented aperture telescope with 2.55 m diameter consisting of an hexagonal monolithic core and six additional petals. An artist impression of the concept is shown in **Figure 2.13**. Since this was a technology development project, no specific details of orbit or operational wavelength are available to the knowledge of the author.

The purpose of the project was to characterise the behaviour of a single deployable petal with a simple deployment mechanism. The mechanism consisted on a strutted hinge, which latched upon reaching the deployed state. Repeatability of the latch was identified as the largest source of deployment non-repeatability in the mechanism. This meant that the largest effort went to develop a latch with very stringent repeatability requirements (**L. D. Peterson and Hinkle, 2005**). The project was expected to end with the single petal test carried out on this structure coupled to an ultra-stable metrology frame. Some results were reported in (**L. D. Peterson et al., 2007**), but no definite conclusion could be found for the project.

The baseline mirror material for this system is a mixture of CFRP and ULE (**Krumweide, 1998; Lake et al., 1999**). The former provides a thermally stable and stiff base, but it does not provide a surface of enough quality. A thin layer of ULE is used for that purpose and bonded to the composite mirror core. The mirror core is protected from the effects of moisture through the use of a moisture barrier (**Krumweide, 1998**).

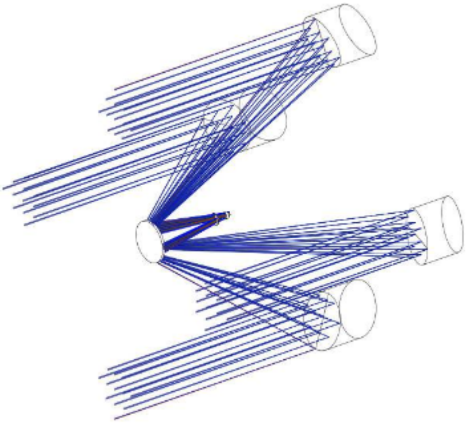

Figure 2.14: Optical ray tracing schematic of DISCIT's baseline optical architecture. (**Silver et al., 2016**)

DEPLOYABLE IN-SPACE COHERENT IMAGING TELESCOPE

The Deployable In-Space Coherent Imaging Telescope (DISCIT) is a project supported by MIT Lincoln Laboratories and the US Air Force. In contrast to the efforts in deployable optics that were discussed previously, reports related to this project are much sparser in the information about their optical design, focusing more on the development of high precision deployment mechanisms. However, a ray-trace schematic of the system can be seen in **Figure** 2.14 The researchers intend to reduce the complexity of deployment mechanisms which can meet optical precision requirements, compared to the complicated deployment mechanism of the JWST (**Silver et al., 2016**).

The baseline optical design is not thoroughly described in the literature available on this project. The objective is a 0.7 m effective sparse aperture Cassegrain telescope (**Silver et al., 2016**). The expected performance of such a system or its operational environment are not clarified either. Some renders related to this project can be found online showing a multi-mirror arrangement with non-deployable secondary mirror and a deployable, segmented primary. The results of the experiments on the tape spring hinge reported in (**Echter et al., 2018**) show that tape spring hinges can achieve micron-level repeatability, and also provide interesting results about their dimensional stability under changes in temperature and humidity.

DISCIT itself does not incorporate any type of baffle as of the current date. A previous project within MIT Lincoln Laboratories, with the involvement of Silver, does investigate the deployment of optical barrel assemblies using similar tape spring hinge technology (**Warren et al., 2009; Warren et al., 2013**). Though this is a separate development to DISCIT, it does mean the authors are aware of the need to baffle sunlight falling onto the telescope.

AUTONOMOUS ASSEMBLY RECONFIGURABLE SPACE TELESCOPE

Another notable research project is the Autonomous Assembly of a Reconfigurable Space Telescope (AAReST). It has been a long-term student project with students from Caltech

Figure 2.15: View of the re-configuration mechanism of AAReST, also showing the integrated tape spring hinge. (**Underwood et al.,** 2018)

supported by the Jet Propulsion Laboratory, and it is expected to be launched in 2019. More than a functional telescope, AAReST is a technology demonstrator for large aperture deformable mirrors, and more importantly in-orbit reconfiguration of optical segments. The proposed system has a 0.4 m aperture and operates at the wavelength range 465-615 nm. The main feature of this mission is the detachment of 3U Cubesats called "Mirrorsats" which will fly away from the main spacecraft, "Coresat", achieve reattachment to it at a different location and operate at a 650 km altitude. (**Underwood et al.,** 2015) This sequence is shown in **Figure** 2.15.

The Coresat mounts two fixed mirrors, whilst the Mirrorsats hold a thin-shell CFRP deformable mirror as described by (**Steeves et al.,** 2016). The large deformable mirrors are mounted on a 3 DOF platform (piston, tip-tilt) for coarser rigid body motions, providing very high authority control. Re-attachment of the mirrorsats is achieved through a electromagnetic docking mechanism, which makes the mirrorsats fall into a Kelvin clamp, which provides a repeatable re-attachment (**Underwood et al.,** 2018). Another valuable element to this mission is the foldable boom which holds the imaging camera. (**Mallikarachchi and Pellegrino,** 2014) described the manufacture of the hinges present on these booms. Cutouts on monolithic CFRP booms are made and then bent until the fold. Once the holding force is removed, the strain energy contained in the fold is released, making the boom go back to its original shape with acceptable repeatability.

ULTRALITE

Ultralightweight Telescope (UltraLITE) (**Huybrechts et al.,** 2000), also called Deployable Optical Telescope (DOT) (**Schrader et al.,** 2002), is a deployable three mirror anastigmat telescope developed mainly by the Air Force Research Laboratories. This proposed design spawned a series of structure experiments to validate several elements of its architecture. The design featured a deployable tower holding the secondary mirror, and three deployable circular mirrors. These mirrors were notable for their very lightweight design, owed to the use of a CFRP core and a thin ULE shell, which also acts as an active mirror (**Catanzaro et al.,** 2000). This development program focused extensively on active vibration controllers (**Lane et al.,** 2008) and the design of a very stiff deployment structure through the use of hybrid CFRP, including high and intermediate modulus fibers (**Huybrechts et al.,** 2000). Several

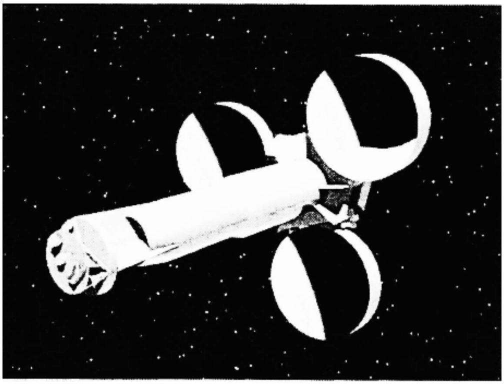

Figure 2.16: Artist impression of the UltraLITE telescope. (**Catanzaro et al., 2000**)

effective apertures of the telescope were reported throughout the technology development program, with a testbed of 1.7 m being built (**Lane et al., 2008**). More system design options are discussed by Powers et al (**Powers et al., 1997**) for a baseline size of 5 to 6 meter apertures flying on high altitudes, in the order of 15,000 km. The precise details of the final design could not be found as to its operating altitude or wavelength, though the latter is understood to be in the visible range.

Catanzaro (**Catanzaro et al., 2000**) mentions active heating as thermal control to keep the desirable stability of the telescope. There is no indication that a sunshield or baffle was proposed in the latest embodiment, although early concept schematics showed a deployable one (**Powers et al., 1997**). This is not elaborated in the texts found during this survey. An artist impression of the concept is shown in **Figure 2.16**.

2.3. EXAMINATION OF CRITICAL TECHNOLOGIES

The structural architecture of deployable space optics is determined by the optical characteristics, such as focal length or operating wavelength, and the chosen environment. The operating wavelength is the major defining factor for the alignment requirements, the aperture size and the instrument's temperature. In addition, the focal length of the system will determine the distance between the major optical elements along the optical axis. These characteristics give rise to a diversity of possible designs, but this section intends on summarising the technologies which underlie them. **Table 2.1** summarises the aforementioned projects along their main characteristics. As this table shows, most of the telescopes proposed are based either on a Cassegrain or TMA configurations, which are fully reflective and therefore avoid cromatic aberrations. The exceptions to this are AAReST and PRISM, which incorporate refractive elements.

Whilst there are many projects, not all of the institutions sponsoring them have the resources to bring them to completion. From the review performed, only JWST and LUVOIR have been extensively documented in all the aspects of design from the optics to the structural mechanics and actuation. PRISM is notable for being the first deployable optical experiment, but its documentation explains more about the control of the focusing

Table 2.1: Summary of deployable optics proposed concepts.

Program	Purpose	Wavelength	Environment	Primary aperture [m]	Active optics DOFs	Thermal control technique	Telescope type	Mirror material	Deployables
JWST	ASTRO	IR	L2	6.5	132 DOF*	Sunshield	TMA	Berylium	M1, M2, Sunshield
LUVOIR	ASTRO	VIS	L2	15 | 8	726|336 DOF**	Sunshade + Heating	TMA	ULE	M1, M2, Sunshield
DoST	ASTRO	VIS	LEO	0.5	3 DOF	Unknown	Cassegrain	Unknown	M2
CST	EO	VIS	LEO	0.15	None	Unknown	Cassegrain	Unknown	M2
SSTL	EO	VIS	LEO	Unknown	3 DOF	Telescopic baffle	Unknown	Unknown	M2
PRISM	EO	VIS	LEO	0.09	1 DOF	Telescopic baffle	Refractive	Glass	Primary lens
LATT	EO	NIR	LEO	4	Adaptive mirror	Baffle	Afocal Cassegrain	Zerodur+CFRP	M1
DPT	EO	VIS	LEO	0.2	None	Unknown	Cassegrain	Unknown	M1, M2
UK Astro DST	EO	VIS	LEO	0.3	12 DOF	Unknown	Cassegrain	Aluminum	M1
TUD DST	EO	VIS	LEO	1.5	12 DOF	Baffle	TMA	SiC	M1, M2, baffle
DOME	EO	NIR	LEO	2.55*	Unknown	Baffle	Unknown	ULE+CFRP	M1
DISCIT	EO	VIS	LEO	0.8	Unknown	Unknown	Cassegrain	Unknown	M1
AAReST	ASTRO	VIS	LEO	0.3	Adaptive mirror	Active heating	Prime focus'	Glass-Piezoelectric	M1, detector
ULTRALite	EO	VIS	LEO	1.7	9 DOF	Active heating	TMA	ULE+CFRP	M1

*DOFs not including fine steering mirrors. **Controlled DOFs are only for rigid body motions, as LUVOIR does not use radius of curvature control. 'Prime focus is corrected with additional lenses.

mechanism and attitude than the thermomechanical requirements (**Komatsu and Nakasuka, 2008**). Other projects have achieved partial hardware demonstrations, showing particular aspects of their technology, but not a systematic approach to addressing the issues highlighted herein. Some of this lack of clarity is potentially attributable to a willingness to withhold information from the public domain.

2.3.1. DEPLOYMENT MECHANISMS AND THE NEED FOR ACTIVE OPTICS

There are two orders of magnitude differences between achievable deployment repeatability and the allowable WFE for high quality imaging in visual and near infrared ranges. Deployment repeatability depends on the specific technology which locks the structure in place and on the size of the structure, with typical values in the order of a few micrometers (**Domber et al., 2002; Warren et al., 1999**). For comparison WFE requirements for diffraction limited optics are in the order of 10s of nanometers (**Lightsey et al., 2018**). In addition, in-orbit disturbances can affect the stability of the system in several timescales. Therefore there is a need for active correction of at least the most sensitive degrees of freedom, which can be determined via optical sensitivity analysis. In the most demanding applications, full 6 DOF per element control and shape control are required. The total stroke of such system must be matched to the magnitude of the foreseeable disturbances, and its resolution must be smaller than the allowable WFE.

This is indeed the overall consensus in the deployable space optics literature, with projects which either focus heavily on the development of novel active optics concepts or acknowledge it as an essential enabler to achieve its goals. This holds true regardless of the overall size of the proposed telescope and its environment. **Table 2.1** shows how the majority of systems include some type of active correction, although some do not specify whether or not they do. (**Lake et al., 2002**) highlight the importance of a trade-off between structural stiffness requirements and authority of the control system. Most active optics mechanisms allow for more DOFs than the six per element pure rigid body kinematics by exerting some control over the surface shape. This can be achieved at the primary optical element, or through the use of a deformable mirror as is the case of the TU Delft DST. JWST implements one extra DOF per mirror segment for curvature control of the primary mirror. AAReST and LATT propose a fully deformable primary mirror with an undefined number of degrees of freedom, which allows much more control authority.

Survivability of these large active mirrors can be achieved through electrostatic locking of the facesheet during launch (**D'Amato et al., 2017**). With this technology, extremely low areal densities, below 20 $\mathrm{kg/m^2}$, can be achieved at the cost of complexity of the active optics mechanisms. However, embodiments such as those in the LATT or AAReST projects are not yet capable of achieving diffraction limited performance at visible wavelengths.

2.3.2. THERMAL AND VIBRATION CONTROL

Thermo-mechanical stability is achieved through the systematic removal of external influences on the telescope at multiple stages of the mission design. Selecting the environment of the telescope is a choice with many potential variables and trades. Deployable optics in the literature are proposed for either LEO or L2 orbits, parallel to the split between Earth observation purposes and astronomy. Missions in LEO would be primarily for Earth Observation, with a focus on lightweight systems that can be produced cheaply, fast and potentially in larger numbers to provide higher temporal and spatial resolution. L2 is too far away to be a good candidate for Earth Observation, but a prime location for astronomy due to a stable thermal environment and constant Sun illumination. Astronomy requires much larger apertures with more stringent optical quality than EO systems.This results in more complex and sensitive systems in a comparatively milder environment. This divide is clear in **table 2.1**, with the largest apertures and number of controlled DOFs predictably belonging to the large observatories at L2.

In L2, a single sunshield is able to greatly reduce the straylight and thermal effects caused by sunlight, although such sunshield has been a critical part of JWST's development and represents a system of considerable complexity and scale on its own. LEO is a very dynamic environment by comparison due to the need to cope with cycles of dayside and eclipse. A notable exception to this would be the particular case of dawn-dusk sunsynchronous orbits whose illumination is constant. It is also more populated by orbital debris from previous missions. A large aperture in LEO comes with the need to deploy a baffle to protect it from sunlight if alignment is to be maintained.

In the literature, thermal stability is addressed mainly through the material choice rather than temperature control of the support structures. LUVOIR is a notable exception to this rule, where active heating is used. Active heating is the simplest way to control the temperature of the optical elements, but it has important drawbacks. Namely it adds to the power requirements of the telescope, is incompatible with cryogenic telescopes, and it increases modelling complexity due to the potential of heat radiating onto other optical assemblies. Eisenhower et al. estimated that for the ATLAST concept, 526.8 W of power would be needed to maintain the correct temperature (**Eisenhower et al., 2015**).

Though this may be attributed to the low TRL of most of the proposals in the literature, there has not been extensive description of a thermal management system and its impacts, with the exception of JWST and LUVOIR (**TEAM, 2019**). The Delft DST team also considers this a major concern for development (**Arink, 2019; Wees, 2019**). This has caused **Table 2.1** to be very incomplete on that aspect.

As for vibration control, there is a need to eliminate or insulate the sources of vibration. One area in which this may be achieved is the design of mechanisms that do not transmit any loads through friction (**Lake and Hachkowski, 2000**) and the substitution of classical bearing hinges and joints with compliant mechanisms which eliminate undesired effects cited in **subsection 2.1.4** such as creaking, backlash, freeplay and wear (**Farhadi Machekposhti et al., 2015**). Due to the need of pointing the telescope towards the target, reaction wheels will likely be always a necessity. Therefore the microvibration requirements outlined in section 2 must be observed. Deployable optics would benefit from magnetic-bearing or otherwise low-noise reaction wheels, although these are more complex and expensive.

2.3.3. LIGHTWEIGHT MIRRORS

Deployable telescopes, compared to monolithic telescopes, have more flexible structures and therefore show comparatively lower eigenfrequencies, which can be partially offset by the use of extremely lightweight, stiff mirrors. Mirror areal density is influenced by total aperture of the segment, available core depth, material choice and core geometry. Lightweight mirrors can be realized by removing material from a mirror blank which achieves bending stiffness by leaving a complex pattern of stiffeners behind the face sheet. This process is limited by manufacturability and local buckling failure modes, if the stiffeners are made excessively thin. Baiocchi and Stahl (**Baiocchi and Stahl, 2009**) cite other concerns that may dominate over areal density when deciding on a mirror design, such as stiffness, complexity and cost.

As for the thermal environment, telescopes operating at cryogenic temperatures benefit from the small cumulative shrinkage of beryllium at cryogenic temperatures, its low density and high strength (**Feinberg et al., 2012**). In the case of warm telescopes, Berylium has a relatively high CTE and is typically outperformed by other high performance materials such as Zerodur, ULE and Silicon Carbide (SiC). Zerodur and ULE have a long usage history in both ground and space telescopes due to their extremely low CTE at ambient temperature, but they present poor thermal conductivity and are brittle compared to metals or SiC. Another candidate family of materials is aluminum alloys. Aluminum has excellent programmatic and mechanical properties, but it also boasts a much higher CTE than its competitors (**East et al., 2018**). However, its good thermal conductivity and the possibility of making its supporting structure out of the same material makes it possible for a full aluminum telescope to have a degree of inherent athermalization, provided the temperature is homogeneous across the entire system. There is little evidence in the literature suggesting that this is enough to offset its high CTE in large aperture telescopes. **Table 2.2** summarises the thermal and mechanical properties of these materials where ρ is the material density, E is the Young's modulus and σ_{Max} the maximum allowable stress.

CFRP is used as a base material which can be mixed with an ultra low CTE material that can be polished in order to profit from the high specific stiffness and thermal stability whilst preserving the optical surface quality.

The alternative to these stiff mirrors are large active mirrors with very small structural depths, which are controllable through electro-mechanical actuation to correct for its large initial surface errors, as shown by the LATT and AAReST projects. These are a prime exam-

Table 2.2: Properties of typical mirror materials. (**Bely, 2003; Feinberg et al., 2012**)

Mirror materials	$\rho[kg/m^3]$	$E[GPa]$	$\sigma_{Max}[MPa]$	$\kappa[W/m/K]$	$\alpha[ppm/K]$	$E/\rho[10^6 m^2/s^2]$	$\sigma_{Max}/\rho[10^3 m^2/s^2]$	$\alpha/\kappa[m/W]$
Borosilicate	2230	63	78	1.2	3.3	28	34,98	2.75
Fused Silica	2200	73	48	1.3	0.52	33	21.82	0.4
ULE	2210	68	50	1.3	0.03	30	22.62	0.023
Zerodur	2530	91	57	1.5	0.05	36	22.53	0.033
CVD SiC	3210	466	440	190	2.2	145	137.07	0.012
Reaction-bonded SiC	2910	360	325.5	155	2.6	124	111.86	0.017
O-30 Beryllium	1850	300	240	216	11.3	162	129.73	0.052
Aluminum	2700	70	310	210	24	26	114.81	0.114
CFRP*	1600	160	2100	2	-0.3	100	1312.50	NA

* CFRP data is very strongly dependent on the type of fibre and resin, as well as the direction, and it cannot be polished to mirror quality. The numbers for this material are only for comparison purposes to the state of the art, in a direction of interest.

ple of the trade-off between mass and control complexity shifting to the latter. So far this approach of very high authority mirror control has not been demonstrated in flight, but experiments have been performed.

2.4. SUMMARY

In this chapter, the main thermomechanical challenges for deployable space optics are described, along with the implementations proposed in 14 diffferent deployable optics missions. Whilst there are large potential gains in mass and volume, system complexity increases substantially. Earth Observation systems compensate this drawback through the possibility of multiple deployment or standardised production, whilst astronomical telescopes are enabled to pursue primary apertures beyond the launcher shroud diameter. The fundamental thermomechanical challenges remain the same, although different projects have studied different aspects with special emphasis. The main challenges in thermomechanical design of deployable space optics, from this point of view, are the repeatability of the deployment mechanism, thermal stability, and the use of active optics to compensate for the lack of stiff structures. It is found that thermal stability in particular has been the least extensively described aspect in these projects. The presented results can serve as a starting point on these design considerations. However, system requirements have a large impact on the key drivers of the design process. The findings presented in this study are being used to direct the development of the Delft University of Technology's Deployable Space Telescope. In this respect, the development is being steered towards four main technologies: a deployable baffle which is axisymmetric and acts as thermal shield, compliant element hinges, which are expected to deliver greater deployment repeatability, a fine actuation mechanism for primary mirror segments, and thermal control techniques for passive secondary mirror spiders.

BIBLIOGRAPHY

Addari, D., Aglietti, G. S., & Remedia, M. (2017). Experimental and numerical investigation of coupled microvibration dynamics for satellite reaction wheels. *Journal of Sound and Vibration*, *386*, 225–241. https://doi.org/10.1016/j.jsv.2016.10.003

Agasid, E. F., Ennico-Smith, K., & Rademacher, A. T. (2013). Collapsible Space Telescope (CST) for Nanosatellite Imaging and Observation. *Proceedings of the 27 th Annual AIAA/USU Conference on Small Satellites*, 1–5.

Alipour, S. M., Kiani, Y., & Eslami, M. R. (2016). Rapid heating of FGM rectangular plates. *Acta Mechanica*, *227*(2), 421–436. https://doi.org/10.1007/s00707-015-1461-9

Arenberg, J., Flynn, J., Cohen, A., Lynch, R., & Cooper, J. (2016). Status of the JWST sunshield and spacecraft. *Space Telescopes and Instrumentation 2016: Optical, Infrared, and Millimeter Wave*, *990405*(August 2016), 990405. https://doi.org/10.1117/12.2234481

Arenberg, J. W., Pohner, J., Harpole, G., Hylan, J., Crooke, J. A., Matonak, B. D., Bolcar, M. R., & Park, S. A. (2018). LUVOIR thermal architecture. *Space Telescopes and Instrumentation 2018: Optical, Infrared, and Millimeter Wave;* https://doi.org/10.1117/12.2312375

Arianespace. (2004). Ariane 5 user's manual.

Arianespace. (2014). Vega User's manual Issue 4 - Revision 0.

Arink, J.-W. (2019). *Thermal-Mechanical Design of a Baffle for the Deployable Space Telescope*.

Baiocchi, D., & Stahl, H. P. (2009). *Enabling Future Space Telescopes : Mirror Technology Review and Development Roadmap*. http://www8.nationalacademies.org/astro2010/DetailFileDisplay.aspx?id=540&origin=publication_detail

Bely, P. Y. (2003). *The Design and Construction of Large Optical Telescopes*. Springer.

Bihl, T. J., Pham, K. D., & Murphey, T. W. (2007). Modeling and control of active gravity offloading for deployable space structures. *6555*(April), 655515. https://doi.org/10.1117/12.717410

Bloemhof, E. E., Lam, J. C., Feria, V. A., & Chang, Z. (2009). Extracting the zero-gravity surface figure of a mirror through multiple clockings in a flightlike hexapod mount. *Applied Optics*, *48*(21), 4239–4245. https://doi.org/10.1364/AO.48.004239

Bolcar, M. R., Balasubramanian, K., Crooke, J., Feinberg, L., Quijada, M., Rauscher, B. J., Redding, D., Rioux, N., Shaklan, S., Stahl, H. P., Stahle, C. M., & Thronson, H. (2016). Technology gap assessment for a future large-aperture ultraviolet-optical-infrared space telescope. *Journal of Astronomical Telescopes, Instruments, and Systems*, *2*(4), 041209. https://doi.org/10.1117/1.JATIS.2.4.041209

Boley, B. A. (1972). Survey of recent developments in the fields of heat conduction in solids and thermo-elasticity. *Nuclear Engineering and Design*, *18*(3), 377–399. https://doi.org/10.1016/0029-5493(72)90109-4

Catanzaro, B. E., Keane, D., Connell, S. J., Baiocchi, D., Burge, J. H., Maji, A. K., & Powers, M. K. (2000). *UltraLITE glass/composite hybrid mirror* (tech. rep. July 2000). https://doi.org/10.1117/12.394003

Champagne, J. A., Hansen, S. M., Newswander, T. T., & Crowther, B. G. (2014). CubeSat Image Resolution Capabilities with Deployable Optics and Current Imaging Technology. *28th Annual AIAA/USU Conference on Small Satellites*.

Coppolino, R. N., Adams, D. S., & Levine, M. B. (2004). Midfrequency band dynamics of large space structures. *Optical Science and Technology, the SPIE 49th Annual Meeting, 2004*, *5528*(September 2004), 150–161. https://doi.org/10.1117/12.563339

Cordero Machado, J., Heinrich, T., Schuldt, T., Gohlke, M., Lucarelli, S., Weise, D., Johann, U., Peters, A., & Braxmaier, C. (2008). Picometer resolution interferometric characterization of the dimensional stability of zero CTE CFRP. *Proceedings of SPIE - The International Society for Optical Engineering*, *7018*(June), 183. https://doi.org/10.1117/12.789495

Corvers, M. (2018). *Design of the Deployment Mechanism for the Primary Mirror of a Deployable Space Telescope*.

D'Amato, F., Gallieni, D., Biasi, R., Molina, M., Duò, F., Ruder, N., Simonetti, F., Zuccaro Marchi, A., Salinari, P., Lisi, F., Riccardi, A., Gambicorti, L., & Pereira do Carmo, J. P. N. (2017). Technological developments for ultra-lightweight, large aperture, deployable mirror for space telescopes. *International Conference on Space Optics — ICSO 2010*, *10565*(October), 80. https://doi.org/10.1117/12.2309213

Dolkens, D., Kuiper, J., de Goeij, B., & Gill, E. (2019). Design and Optimization of a Deployable Telescope for Earth Observation. *Draft journal paper*.

Dolkens, D., Kuiper, H., & Villalba Corbacho, V. M. (2018). The deployable telescope: a cutting-edge solution for high spatial and temporal resolved Earth observation. *Advanced Optical Technologies*, *7*(6).

Domber, J. L., Hinkle, J. D., Peterson, L. D., & Warren, P. A. (2002). Dimensional Repeatability of an Elastically Folded Composite Hinge for Deployed Spacecraft Optics. *Journal of Spacecraft and Rockets*, *39*(5), 646–652. https://doi.org/10.2514/2.3877

East, M. J., Knight, J. S., Mooney, T., Havey, K., & Allen, L. N. (2018). Material selection for far Infrared telescope mirrors. *Space Telescopes and Instrumentation 2018: Optical, Infrared, and Millimeter Wave*, (July 2018), 58. https://doi.org/10.1117/12.2314310

Echter, M. A., Silver, M. J., D'Elia, E., & Peterson, M. (2018). Recent Developments in Precision High Strain Composite Hinges for Deployable Space Telescopes. *2018 AIAA Spacecraft Structures Conference*, (January). https://doi.org/10.2514/6.2018-0939

Edeson, R., Aglietti, G. S., & Tatnall, A. R. (2010). Conventional stable structures for space optics: The state of the art. *Acta Astronautica*, *66*(1-2), 13–32. https://doi.org/10.1016/j.actaastro.2009.06.015

Eisenhower, M. J., Cohen, L. M., Feinberg, L. D., Matthews, G. W., Nissen, J. A., Park, S. C., & Peabody, H. L. (2015). ATLAST ULE mirror segment performance analytical predictions based on thermally induced distortions. *UV/Optical/IR Space Telescopes and Instruments: Innovative Technologies and Concepts VII*, *9602*(September 2015), 96020A. https://doi.org/10.1117/12.2188008

Elgafy, A., Mesalhy, O., & Lafdi, K. (2004). Numerical and experimental investigations of melting and solidification processes of high melting point PCM in a cylindrical enclosure. *Journal of Heat Transfer*, *126*(5), 869–875. https://doi.org/10.1115/1.1800492

EOPortal. (n.d.). Dobson Space Telescope. https://directory.eoportal.org/web/eoportal/satellite-missions/content/-/article/dobson-2

Farhadi Machekposhti, D., Tolou, N., & Herder, J. L. (2015). A Review on Compliant Joints and Rigid-Body Constant Velocity Universal Joints Toward the Design of Compliant Homokinetic Couplings. *Journal of Mechanical Design*, *137*(3), 032301. https://doi.org/10.1115/1.4029318

Farrah, D., Smith, K. E., Ardila, D., Bradford, C. M., Dipirro, M., Ferkinhoff, C., Glenn, J., Goldsmith, P., Leisawitz, D., Nikola, T., Rangwala, N., Rinehart, S. A., Staguhn, J., Zemcov, M., Zmuidzinas, J., Bartlett, J., Carey, S., Fischer, W. J., Kamenetzky, J., . . . Stierwalt, S. (2017). Review: Far-Infrared Instrumentation and Technology Development for the Next Decade. http://arxiv.org/abs/1709.02389

Feinberg, L., Cohen, L., Dean, B., Hayden, W., Howard, J., & Keshi-Kuha, R. (2012). *Space telescope design considerations* (Vol. 51). https://doi.org/10.1117/1.oe.51.1.011006

Findley, W. N. L., & James S. Onaran, K. (1978). *Creep and Relaxation of Nonlinear Viscoelastic Materials - With an Introduction to Linear Viscoelasticity*. Dover Publications.

Foster, C. I., Tinker, M. I., Nurre, G. S., & Till, W. A. (1995). *The solar array-induced disturbance of the Hubble Space Telescope Pointing System* (tech. rep.). NASA.

Fransen, S., Doyle, D., & Catanzaro, B. (2011). Opto-mechanical modeling of the Herschel Space Telescope at ESA/ESTEC. *833604*(November 2011), 833604. https://doi.org/10.1117/12.915669

Gallagher, B. B., Smith, K. Z., Knight, J. S., Sullivan, J., Rudeen, A., Babcock, K., Hardy, B., Barto, A., Wolf, E., Coppock, E., Davis, C. R., & Chonis, T. S. (2018). JWST mirror and actuator performance at cryo-vacuum. *Space Telescopes and Instrumentation 2018: Optical, Infrared, and Millimeter Wave*, *1069808*(July 2018), 7. https://doi.org/10.1117/12.2312872

Gerlach, B., Ehinger, M., & Seiler, R. (2006). Low noise five-axis magnetic bearing reaction wheel. *IFAC Proceedings Volumes (IFAC-PapersOnline)*, *4*(PART 1), 572–577. https://doi.org/10.3182/20060912-3-DE-2911.00100

Gooding, D., Richardson, G., Haslehurst, A., Smith, D., Saunders, C., Aglietti, G., Blows, R., Shore, J., Hampson, K., & Booth, M. (2018). A novel deployable telescope to facilitate a low-cost < 1m GSD video rapid-revisit small satellite constellation. *International Conference on Space Optics*, (0).

Greschik, G., & Belvin, W. K. (2007). High-Fidelity Gravity Offloading System for Free-Free Vibration Testing. *Journal of Spacecraft and Rockets*, *44*(1), 132–142. https://doi.org/10.2514/1.21454

Hale, L. C., & Slocum, A. H. (2001). Optimal design techniques for kinematic couplings. *Precision Engineering*, *25*(2), 114–127. https://doi.org/10.1016/S0141-6359(00)00066-0

Hallibert, P., & Zuccaro Marchi, A. (2016). Developments in active optics for space instruments: an ESA perspective. (July 2016), 99121H. https://doi.org/10.1117/12.2232096

Han, O., Kienholz, D., Janzen, P., & Kidney, S. (2010). Gravity-Offloading System for Large-Displacement Ground Testing of Spacecraft Mechanisms. *Proceedings of 40th aerospace mechanisms symposium*, (May).

Hinkle, J., Peterson, L., Klein, K., Levine, M., & Peng, C.-Y. (2005). Submicron friction mechanics at ambient and cryogenic temperatures. *Optics and Photonics*, *5899*(August 2005), 589910. https://doi.org/10.1117/12.626173

Howard, J. M. (2004). Optical modeling activities for the James Webb Space Telescope (JWST) project: I. The linear optical model. (January 2004), 82. https://doi.org/10.1117/12.507735

Howard, J. M. (2007a). Optical modeling activities for NASA's James Webb Space Telescope (JWST): III. Wavefront aberrations due to alignment and figure compensation. *667503*(Septemb 2007). https://doi.org/10.1117/12.735069

Howard, J. M. (2007b). Optical modeling activities for NASA's James Webb Space Telescope (JWST): IV. Overview and introduction of MATLAB based toolkits used to interface with optical design software. https://doi.org/10.1117/12.735046

Howard, J. M. (2011). Optical integrated modeling activities for the James Webb Space Telescope (JWST). (November 2011), 83360E. https://doi.org/10.1117/12.916844

Howard, J. M., & Feinberg, L. D. (2009). Optical modeling activities for NASA's James Webb Space Telescope (JWST): VI. secondary mirror figure compensation using primary mirror segment motions. *Proc. SPIE 7436, UV/ Optical/IR Space Telescopes: Innovative Technologies and Concepts IV, 74360C,* (August 2009). https://doi.org/10.1117/12.825420

Howard, J. M., & Ha, K. (2004). Optical modeling activities for the James Webb Space Telescope (JWST) project: II. Determining image motion and wavefront error over an extended field of view with a segmented optical system. https://doi.org/10.1117/12.552032

Howard, J. M., Ha, K. Q., Shiri, R., Smith, J. S., Mosier, G., & Muheim, D. (2008). Optical modeling activities for NASA's James Webb Space Telescope (JWST): Part V. Operational alignment updates. (July 2008), 70170X. https://doi.org/10.1117/12.790237

Huybrechts, S., Wegner, P., Maji, A., Kozola, L. B., Griffin, S., & Meink, T. (2000). Structural Design for Deployable Optical Telescopes. *2000 IEEE Aerospace Conference. Proceedings (Cat. No.00TH8484)*. https://doi.org/10.1109/AERO.2000.878448

Hyde, T. T., Ha, K. Q., Johnston, J. D., Howard, J. M., & Mosier, G. E. (2004). Integrated modeling activities for the James Webb Space Telescope: optical jitter analysis. (October 2004), 588. https://doi.org/10.1117/12.551806

Inamori, T., Shimizu, K., Mikawa, Y., Tanaka, T., & Nakasuka, S. (2013). Attitude Stabilization for the Nano Remote Sensing Satellite PRISM. *Journal of Aerospace Engineering*, *26*(3), 594–602. https://doi.org/10.1061/(asce)as.1943-5525.0000170

Ingham, M. D., & Crawley, E. F. (2001). Microdynamic Characterization of Modal Parameters for a Deployable Space Structure Introduction. *Aiaa Journal*, *39*(2), 331–338. https://doi.org/10.2514/2.1309

Johnston, J. D., Howard, J. M., Mosier, G. E., Parrish, K. A., McGinnis, M. A., Bluth, M., Kim, K., & Ha, K. Q. (2004). Integrated modeling activities for the James Webb Space Telescope: Structural-Thermal-Optical Analysis, 588. https://doi.org/10.1117/12.551806

Kawamura, R., Tanigawa, Y., Kusuki, S., & Hamamura, H. (2008). Fundamental thermoelasticity equations for thermally induced flexural vibration problems for inhomogeneous plates and thermo-elastic dynamical responses to a sinusoidally varying surface temperature. *Journal of Engineering Mathematics*, *61*(2-4), 143–160. https://doi.org/10.1007/s10665-007-9190-2

Kim, D. K. (2014a). Micro-vibration model and parameter estimation method of a reaction wheel assembly. *Journal of Sound and Vibration*, *333*(18), 4214–4231. https://doi.org/10.1016/j.jsv.2014.04.032

Kim, D. K. (2014b). Micro-vibration model and parameter estimation method of a reaction wheel assembly. *Journal of Sound and Vibration*, *333*(18), 4214–4231. https://doi.org/10.1016/j.jsv.2014.04.032

Kim, Y. A. (1998). *Thermal Creak Induced Dynamics of Space Structures* (Doctoral dissertation November). Massachusetts Institute of Technology. http://mechanicaldesign.asmedigitalcollection.asme.org/article.aspx?doi=10.1115/1.4029318

Knight, J. S., Acton, D. S., Lightsey, P., Contos, A., & Barto, A. (2012). Observatory alignment of the James Webb Space Telescope. *Space Telescopes and Instrumentation*, *8442*(September 2012), 84422C. https://doi.org/10.1117/12.926816

Komatsu, M., & Nakasuka, S. (2008). University of Tokyo Nano Satellite Project "PRISM . *Trans. JSASS Space Tech. Japan*, *7*, 19–24. https://doi.org/10.2322/tstj.7.Tf{_}19

Kramer, E., Kellaris, N., Daal, M., Sadoulet, B., Golwala, S., & Hollister, M. (2014). Material selection for cryogenic support structures. *Journal of Low Temperature Physics*, *176*(5-6), 1103–1108. https://doi.org/10.1007/s10909-013-1052-x

Krikken, A. (2018). *Design of the Secondary Mirror Support Structure for the Deployable Space Telescope.*

Krumweide, G. C. (1998). Issues to be addressed in the design and fabrication of ultra-lightweight meter-class optics. *1998 Space Technology & Applications International Forum*. https://doi.org/10.1117/12.324460

Lake, M. S., Fung, J., Gloss, K., & Liechty, D. S. (1997). Experimental Characterization of Hysteresis in a Revolute Joint for Precision Deployable Structures. *38th AIAA Structures, Structural Dynamics, and Materials Conference, Kissimmee, Florida*, 1–12. https://ia800501.us.archive.org/14/items/nasa_techdoc_20040105599/20040105599.pdf

Lake, M. S., & Hachkowski, M. R. (2000). *Design of Mechanisms for Deployable , Optical Instruments : Guidelines for Reducing Hysteresis* (tech. rep. March).

Lake, M. S., Peterson, L. D., & Levine, M. B. (2002). Rationale for Defining Structural Requirements for Large Space Telescopes. *Journal of Spacecraft and Rockets*, *39*(5), 674–681. https://doi.org/10.2514/2.3889

Lake, M. S., Phelps, J. E., Dyer, J. E., Caudle, D. A., Tam, A., Escobedo, J., & Kasl, E. P. (1999). A deployable primary mirror for space telescopes. *SPIE International Symposium on Optical Science, Engineering, and Instrumentation*, (3785-02).

Lake, M. S., Warren, P. A., & Peterson, L. D. (1996). A Revolute Joint With Linear Load-Displacement Response for Precision Deployable Structures. *37th AIAA/ASME/ASCE.AHS.ASC Structures, Structural Dynamics and Materials Conference*. https://doi.org/10.2514/6.1976-755

Lane, S. A., Lacy, S. L., Babuska, V., Hanes, S., Schrader, K., & Fuentes, R. (2008). Active Vibration Control of a Deployable Optical Telescope. *Journal of Spacecraft and Rockets*, *45*(3), 568–586. https://doi.org/10.2514/1.30838

Levine, M. B. (1998). The Interferometry Program Flight Experiments : IPEX I & II. *3350*(March), 1–12. https://doi.org/10.1117/12.317128

Levine, M. B., & White, C. (2003). Material damping experiments at cryogenic temperatures. *Optical Materials and Structures Technologies*, *5179*(December 2003), 165. https://doi.org/10.1117/12.506838

Lightsey, P. A., Atkinson, C., Clampin, M., & Feinberg, L. D. (2012). James Webb Space Telescope: large deployable cryogenic telescope in space. *Optical Engineering*, *51*(1), 011003. https://doi.org/10.1117/1.OE.51.1.011003

Lightsey, P. A., Knight, J. S., Bolcar, M. R., Eisenhower, M. J., Feinberg, L. D., Hayden, W. L., & Park, S. C. (2018). Optical budgeting for LUVOIR. *Space Telescopes and Instrumentation 2018: Optical, Infrared, and Millimeter Wave*, *1069813*(July 2018), 38. https://doi.org/10.1117/12.2312256

Liu, K.-C., Maghami, P., & Blaurock, C. (2008). Reaction wheel disturbance modeling, jitter analysis, and validation tests for Solar Dynamics Observatory. *AIAA Guidance, Navigation and Control Conference and Exhibit*, (August), 1–18. https://doi.org/doi:10.2514/6.2008-7232

Lopes Barreto, J. W. (2017). *Deployable Space Telescope: Optimal Boom Design for High Precision Deployment of the Secondary Mirror.*

Maaß, R., & Derlet, P. M. (2017). Micro-plasticity and recent insights from intermittent and small-scale plasticity. *Acta Materialia*, *143*, 338–363. https://doi.org/10.1016/j.actamat.2017.06.023

Malik, P., & Kadoli, R. (2018). Thermal induced motion of functionally graded beams subjected to surface heating. *Ain Shams Engineering Journal*, *9*(1), 149–160. https://doi.org/10.1016/j.asej.2015.10.010

Mallikarachchi, H. M. Y. C., & Pellegrino, S. (2014). Design of Ultrathin Composite Self-Deployable Booms. *Journal of Spacecraft and Rockets*, *51*(6), 1811–1821. https://doi.org/10.2514/1.A32815

Masterson, R. A., Miller, D. W., & Grogan, R. L. (2002). Development and validation of reaction wheel disturbance models: Empirical model. *Journal of Sound and Vibration*, *249*(3), 575–598. https://doi.org/10.1006/jsvi.2001.3868

Mazzinghi, P., Bratina, V., Ferruzzi, D., Gambicorti, L., Simonetti, F., Zuccaro Marchi, A., Salinari, P., Lisi, F., Olivier, M., Bursi, A., & Pereira do Carmo, J. (2006). An ultra-lightweight, large aperture, deployable telescope for advanced lidar applications. *International Conference on Space Optics — ICSO 2006*, *10567*(June). https://doi.org/10.1117/12.2308098

Ostrem, F. E. (1971). *Transportation and Handling Loads* (tech. rep.).

Pepper, S. (2018). *Design of a Primary Mirror Fine Positioning Mechanism for a Deployable Space Telescope.*

Peterson, L. D., Hinkle, J. D., Footdale, J. N., & Jeon, S. K. (2007). Technology for an Earth Observing Deployed Lidar Telescope. *48th AIAA/ASME/ASCE/AHS/ASC Structures, Structural Dynamics, and Materials Conference<.*

Peterson, L., & Hinkle, J. (2003). Microdynamic Design Requirements for Large Space Structures. *44th AIAA/ASME/ASCE/AHS/ASC Structures, Structural Dynamics, and Materials Conference*, (April), 1–11. https://doi.org/10.2514/6.2003-1451

Peterson, L. D., & Hinkle, J. D. (2005). What Limits the Achievable Areal Densities of Large Aperture Space Telescopes? *Proc. SPIE 58990A, UV/Optical/IR Space Telescopes: Innovative Technologies and Concepts II*, *58990A*(August 2005). https://doi.org/10.1117/12.619878

Powers, M., Leitner, J., Bell, K. D., Boucher, R., Hackney, E., Robertson, L., & Schrader, K. (1997). *Assessment of a large aperture telescope trade space and active opto-mechanical control architecture.*

R. Hardaway, L. M., & Peterson, L. D. (2002). Nanometer-Scale Spontaneous Vibrations in a Deployable Truss Under Mechanical Loading. *AIAA Journal*, *40*(10), 2070–2076. https://doi.org/10.2514/2.1540

Redding, D., Coste, K., Polanco, O., Pineda, C., Hurd, K., Tseng, H., Quezada, J., Martin, S., Nissen, J., Schulz, K., Tesch, J., Cady, E., Rodgers, M., East, M., Mooney, J., & Stark, C. (2018). HabEx Lite: a starshade-only habitable exoplanet imager alternative. *Space Telescopes and Instrumentation 2018: Optical, Infrared, and Millimeter Wave*, (July 2018), 32. https://doi.org/10.1117/12.2310058

Reynolds, P., Atkinson, C., & Gliman, L. (2004). Design and Development of the Primary and Secondary Mirror Deployment Systems of the Cryogenic JWST. *37th Aerospace Mechanisms Symposium*, (Figure 1), 29–44.

Sato, Y., Kim, S. K., Kusakawa, Y., Shimizu, K., Tanaka, T., Komatsu, M., Lambert, C., & Nakasuka, S. (2008). Extensible Flexible Optical System for Nano-scale Remote Sensing Satellite " PRISM ". *Trans. JSASS Space Tech. Japan*, *7*, 13–18. https://doi.org/https://doi.org/10.2322/tstj.7.Tm{_}13

Schenk, M., & Guest, S. D. (2014). On zero stiffness. *Journal of Mechanical Engineering Science*, *228*(10), 1701–1714. https://doi.org/10.1177/0954406213511903

Schrader, K. N., Fetner, R. H., Donaldson, J., Fuentes, R. J., & Erwin, R. S. (2002). Integrated control system development for phasing and vibration suppression for a sparse-array telescope. (December 2002), 134. https://doi.org/10.1117/12.460572

Schwartz, N., Pearson, D., Todd, S., Milanova, M., Brzozowski, W., Vick, A., Lunney, D., MacLeod, D., Greenland, S., Sauvage, J.-F., & Gore, B. (2018). Laboratory Demonstration of an Active Optics System for High-Resolution Deployable CubeSat. *The 4S Symposium*, (1), 1–15. https://doi.org/10.1016/S0168-9274(99)00108-7

Schwartz, N., Pearson, D., Todd, S., Vick, A., Lunney, D., & MacLeod, D. (2016). A Segmented Deployable Primary Mirror for Earth Observation from a CubeSat Platform. *Proceedings of the AIAA/USU Conference on Small Satellites, SSC16*, SSC16-WK–23.

Segert, T., Danziger, B., Gork, D., & Lieder, M. (2006). Dobson space telescope: development of an optical payload of the next generation. *International Conference on Space Optics — ICSO 2006*, *10567*(June 2006). https://doi.org/10.1117/12.2308063

Segert, T., Danziger, B., & Lieder, M. (n.d.). *Dobson Space Telescope the Future of Microsat Based Observation* (tech. rep.). DLR. Berlin.

Silver, M. J., Echter, M. A., Reid, B. M., & Banik, J. (2016). Precision High Strain Composite Hinges for the Deployable In-Space Coherent Imaging Telescope. *3rd AIAA Spacecraft Structures Conference*, (January), 1–21. https://doi.org/10.2514/6.2016-0969

Simonetti, F., Zuccaro Marchi, A., Gambicorti, L., Bratina, V., & Mazzinghi, P. (2010). Large aperture telescope for advanced lidar system. *Optical Engineering*, *49*(7), 073001. https://doi.org/10.1117/1.3461976

Stahl, H. P., Feinberg, L. D., & Texter, S. C. (2004). JWST primary mirror material selection. (October 2004), 818. https://doi.org/10.1117/12.549582

Steeves, J., Jackson, K., Pellegrino, S., Redding, D., Wallace, J. K., Bradford, S. C., & Barbee, T. (2016). Multilayer active shell mirrors for space telescopes. *Proc. SPIE 9912, Ad-*

vances in Optical and Mechanical Technologies for Telescopes and Instrumentation II, (July 2016), 99121K. https://doi.org/10.1117/12.2233594

Stohlman, O., & Pellegrino, S. (2010). Shape Accuracy of a Joint-Dominated Deployable Mast. *51st AIAA/ASME/ASCE/AHS/ASC Structures, Structural Dynamics, and Materials Conference
 18th AIAA/ASME/AHS Adaptive Structures Conference
 12th*, 1–15. https://doi.org/10.2514/6.2010-2605

TEAM, L. (2019). *LUVOIR Final Report* (tech. rep.). NASA.

Team, L. (2018). *LUVOIR Interim Report* (tech. rep.). NASA.

Thompson, S. J., Doel, A. P., Whalley, M., Edeson, R., Tosh, I., Atad-Ettedgui, E., Montgomery, D., & Nawasra, J. (2010). Large aperture telescope technology: a design for an active lightweight multi-segmented fold-out space mirror. *International Conference on Space Optics — ICSO 2010*, *10565*(October), 78. https://doi.org/10.1117/12.2309210

Thornton, E. A., & Kim, Y. A. (1993). Thermally Induced Bending Vibrations of a Flexible Rolled-Up Solar Array. *34th Structures, Structural Dynamics and Materials Conference*. https://doi.org/10.2514/6.1993-1554

Thorpe, J. I., Parvini, C., & Trigo-Rodriguez, J. (2015). Detection and Characterization of Micrometeoroids with LISA Pathfinder. *Astronomy & Astrophysics*, *107*, 1–6. https://doi.org/10.1051/0004-6361/201527658

Tupper Hyde, T., & Postman, M. (2010). *Technology development plan for the Advanced Technology Large Aperture Space Telescope (ATLAST): A Roadmap for UVIOR Technology, 2010-2020.* (tech. rep.). NASA Goddard Space Flight Centre.

Underwood, C., Pellegrino, S., Lappas, V. J., Bridges, C. P., & Baker, J. (2015). Using CubeSat/micro-satellite technology to demonstrate the Autonomous Assembly of a Reconfigurable Space Telescope (AAReST). *Acta Astronautica*, *114*, 112–122. https://doi.org/10.1016/j.actaastro.2015.04.008

Underwood, C., Pellegrino, S., Priyadarshan, H., Simha, H., Bridges, C., Goel, A., Talon, T., Leclerc, A. P. C., Wei, Y., Royer, F., Ferraro, S., Sakovsky, M., Marshall, M., Jackson, K., Sommer, C., Vaidhyanathan, A., Vijayakumari Surendran Nair, S., & Baker, J. (2018). AAReST Autonomous Assembly Reconfigurable Space Telescope Flight Demonstrator. *69th International Astronautical Congress (IAC)*.

United Launch Alliance. (2010). Atlas V Launch Services User's Guide. http://www.ulalaunch.com/uploads/docs/AtlasVUsersGuide2010.pdf

Villalba, V., Kuiper, H., & Gill, E. (2020). Review on thermal and mechanical challenges in the development of deployable space optics. *Journal of Astronomical Telescopes, Instruments, and Systems*, *6*(1). https://doi.org/10.1117/1.JATIS.6.1.010902

Voorn, M. (2018). *Initiating the Testing Phase of a Deployable Space Telescope: An Experimental Characterisation of Hysteresis in CORE Hinges.*

Waldie, D. D., & Gilman, L. N. (2004). Technology development for large deployable sunshield to achieve cryogenic environment. *AIAA Space 2004 Conference and Exposition*, *2*(September), 1396–1405. https://doi.org/10.2514/6.2004-5987

Warden, R. M. (2006). Cryogenic Nano-Actuator for JWST. *38th Aerospace Mechanisms Symposium.* http://esmats.eu/amspapers/pastpapers/pdfs/2006/warden.pdf

Warren, P. A., Person, L. D., & Miller, F. (1999). Submicron Mechanical Stability of a Prototype Deployable Space Telescope Support Structure Introduction. *Journal of Spacecraft and Rockets*, *36*(5). https://doi.org/10.2514/2.3492

Warren, P. A., Silver, M. J., & Dobson, B. J. (2009). Lightweight optical barrel assembly structures for large deployable space telescopes. *Proceedings of SPIE - The International Society for Optical Engineering, 7436*(August 2009). https://doi.org/10.1117/12.826992

Warren, P. A., Silver, M. J., Dobson, B. J., & MacEwen, H. A. (2013). Experimental characterization of deployable outer barrel assemblies for large space telescopes. *886008*(October 2013), 886008. https://doi.org/10.1117/12.2025577

Wees, T. v. (2019). *Thermal Modelling & Analysis of the Deployable Space Telescope.*

White, C. V., & Levine, M. B. (2001). Microdynamic issues in large deployable space telescopes. (March 2001), 163–171. https://doi.org/10.1117/12.417338

Wijker, J. (2008). *Spacecraft Structures.* Springer. https://doi.org/10.1007/978-3-540-75553-1

3

DEVELOPMENT OF MECHANISMS FOR ACTIVE OPTICS MECHANISMS

Around the world the nations wait
For some wise words from their leading light
You know it's not only madmen who listen to fools

Iron Maiden - Total Eclipse

Deployable space telescopes with segmented primary mirrors need to be aligned with nanometre precision in order to minimise wavefront error. This level of alignment cannot currently be achieved with a deployment mechanism alone in the dynamic space environment. Therefore an active optics mechanism is required. In this chapter, a design rationale for such technology is described, illustrated by the development of a 3 degrees-of-freedom mechanism. The design and modelling approach presented here integrates thermal, mechanical and optical models with simple interfaces so that new iterations of the design can be produced and evaluated end-to-end. The tool can be used to allocate misalignment budgets, conduct mechanical sensitivity analyses, or perform preliminary Structural Thermal Optical Performance (STOP) analysis.

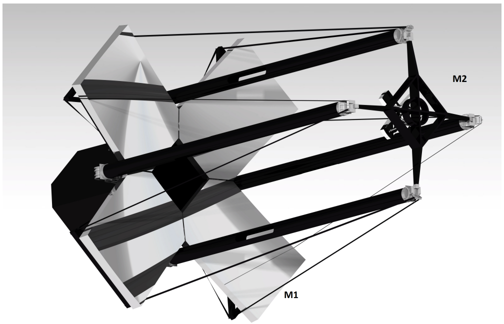

Figure 3.1: Artistic impression of the TU Delft Deployable Space Telescope.

3.1. INTRODUCTION

The main mechanical challenges of deployable telescopes arise from the need to align the segments to a fraction of the operating wavelength. In order to achieve this, a mechanism which repeatably positions the mirror within the required tolerance is needed. In addition to its positioning role, the mechanism needs to be insensitive to temperature variations experienced over the orbit, which complicates modelling activities and concept evaluations. This complication may result in a suboptimal systems engineering process which does not account for these effects until a latter stage. In the design and modelling approach presented herein, all aspects of mechanism development are taken into consideration from the beginning. In this chapter, the design process for active optics in the TU Delft Deployable Space Telescope (DST) is described. The procedure described and analysed integrates mechanical, structural and thermal considerations, and allows flexible early development of a mechanism concept which can be further developed at a later stage. This method is particularly well-suited for early development and feasibility studies with limited resource availability. In this thesis, the focus is in the mechanical aspects of the design. Electrical compatibility with the other spacecraft systems, power or control aspects are not extensively considered here. An artistic rendition of the complete instrument can be seen in **Figure** 3.1.

The overall system architecture of the DST was already introduced in **Chapter** 2. The four M1 segments have a tapered rectangle shape and are estimated to have a mass of 6 kg each. The primary mirror segments are supported by a plate which falls into a kinematic mount during deployment (**Corvers,** 2018). The interface between this plate and the mirror is the mechanism described here, which is referred to as Primary Mirror Active Optics (PMAO) mechanism. The mechanism is in turn bolted to a support structure with a hinge to the instrument housing. This support structure locks into a cantilever position during the deployment of the telescope and remains in that position thereafter. A physical architecture diagram of this instrument was made by Pepper (**Pepper,** 2018) and is shown in **Figure** 3.2.

The top level functional analysis of the primary mirror deployment sequence is as follows:

1. Support structure deploys.

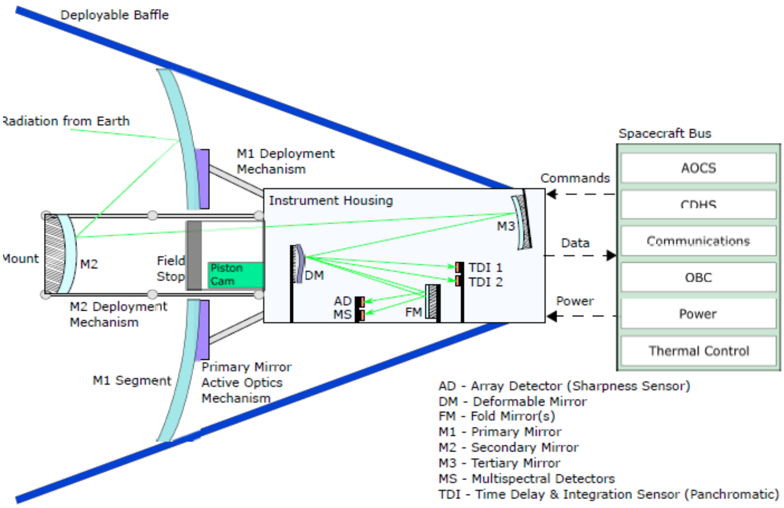

Figure 3.2: Physical architecture diagram showing the main optical and structural elements. (**Pepper,** 2018)

2. Optical quality metrics are evaluated and a correction calculated.
3. PMAO receives a pose from its control system and reaches said pose.
4. Optical quality metrics are re-evaluated and the PMAO reaches new poses until image quality is satisfactory.
5. PMAO holds correct pose during the orbit.
6. PMAO corrects drifts and short-term vibrations as needed.

3.2. BASIC REQUIREMENTS AND INITIAL DESIGN.

The design process described here aims to derive possible solution concepts based on the top-down subsystem requirements, and select the best one based on objective criteria. The sources of these requirements can be found on the mechanism's context diagram presented in **Figure** 3.3, which shows the conceptual interactions of the mechanism with its environment.

The elements of the context diagram are sources of requirements:

- Assembly environment: At this stage, specific requirements are not derived from assembly considerations such as corrosion or handling and manufacturing loads, but
- Launch environment: Since the launch is a very structurally demanding event, some requirements need to be defined and used for initial sizing. These are the launch survivability requirements, and they take a significant portion of the sizing and modelling efforts.
- Space environment: The main contributions to requirements are related to thermal cycling, microvibration, and degradation due to radiation and operation.

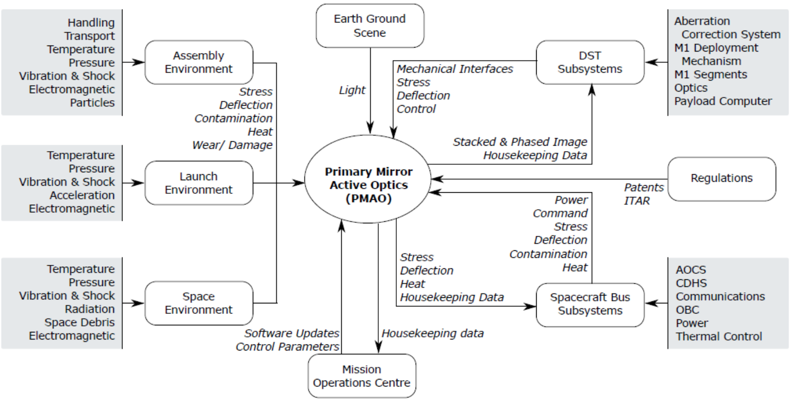

Figure 3.3: Context diagram for the PMAO mechanism. Reprinted from (**Pepper, 2018**).

- Earth Ground Scene: The ground scene has a significant impact in the use of sharpness optimization techniques as control driver for the active optics mechanisms. No requirements can be derived as of yet for the PMAO itself, but there could be bounds to how quickly the system needs to react based on using the image for segment pose corrections.

- Missions operation centre: Ground operations can provide software updates and collect housekeeping data, but from the perspective of the mechanical or thermal design, it is not expected to generate requirements.

- DST subsystems: The PMAO must be mechanically, electrically and electronically compatible with the rest of the instrument. This includes mechanical and electrical interfaces, control electronics and transfer of loads between DST subsystems. However, as part of the bottom up systems engineering approach, only some margins are needed until other systems are better defined than they are.

- Regulations: The system and its manufacturing needs to be compliant with any applicable environmental or trade regulations. One decision made on the basis of regulation is that the system should not rely on any components listed in the International Traffic in Arms Regulations (ITAR).

- Spacecraft bus subsystems: Other subsystems are not expected to have direct mechanical interfaces to the PMAO, but may have an impact in generating loads, such as reaction wheel microvibration.

A more thorough list of requirements can be found in Pepper's thesis (**Pepper, 2018**) or the DST general requirements document. The most determining requirements for a mechanism early in the design are those that affect its operating capabilities, namely its stroke, resolution, and degrees-of-freedom (DOF) of actuation. Those requirements are derived from the mission science requirements defined by Dolkens **Dolkens, 2015**, as an error in the pose of the M1 segments produces a decrease in image quality.

The analysis of specific launch loads is too complex and specific for practical early design. For early design purposes, an equivalent quasi-static acceleration, coupled with a minimum eigenfrequency requirement, may be used instead of a full vibration response (**Wijker, 2008**). In this case, these were set as a 30 times gravity quasi-static load in any given axis, and a minimum 100 Hz first eigenfrequency. The first it to withstand low frequency vibration with sufficient margin of safety, the second to avoid resonance with launcher vibration. Survival of loads during assembly, transportation and operations need to be verified. However, these do not drive the early design to the same extent. These loads are typically lower than those experienced during launch and therefore, as a first approximation, fulfilling launch survival requirements implies fulfilling these. This is not necessarily true for all cases, such as in the presence of thermal loads, which cause very high thermal stresses on overconstrained structures. However, studying such cases requires a baseline configuration to evaluate.

Once the system requirements are defined, the design procedure needs to be established.This comprises the tasks of selecting the constraint and actuation kinematics via the Freedom And Constraint Topologies (FACT) analysis, selection of the actuator type, material choice, and concept generation and trade-off. The design process is illustrated in **Figure 3.4**.

After the trade-off, the selected concept is iterated upon to find the correct element sizing. Then the verification and validation processes will demonstrate that the design complies with the requirements and is feasible. Other modelling activities and procedures are needed for a complete mechanism design, verification and validation, to verify other aspects of a control system. Examples of these other aspects are the controller, electrical interfaces, or surface degradation. These activities are out of the scope of this thesis.

3.2.1. PMAO DESIGN REQUIREMENTS

The PMAO is meant to offer 10 nm resolution as per the allowable wavefront error in three DOFs, specifically piston and tip-tilt directions, with x-y decenter and clocking motions not corrected. **Figure 3.5** defines the naming convention for the six degrees of freedom of an optical element. define The stroke is determined by the repeatability requirements of the deployable structure, because the PMAO must be able to compensate for the allowable deployment error (**Dolkens, Kuiper, et al., 2018**). The misalignment and shape deformation budgets allowed for the primary mirror are shown in **Table 3.1**. Finally, the PMAO shall contribute to stabilising the mirror segments to the drift and stability budgets.

Strength requirements are based on the aforementioned equivalent quasi-static load approach. At an early stage in the development, a detailed mirror design may not be available. A mirror mass estimate of 6 kg is used here, which amounts to a mirror areal density of 21.5 kg/m^2. This is deemed conservative compared to the state of the art. As an example, the ALADIN telescope mounted on the Aeolus mission had a mass of 75 kg with a primary mirror of 1.5 m diameter. (**Morançais et al., 2006**) The latest proposal for LUVOIR (**TEAM, 2019**) calls for a 19 kg/m^2 areal density but noted figures as low as 10 kg/m^2 were achievable. The quasi-static load is a combined 30 g acceleration in two axes combined. The minimum

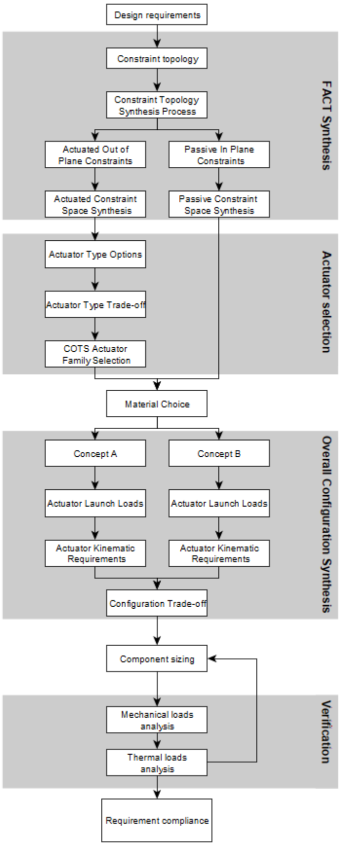

Figure 3.4: Sequence of design tasks performed for the PMAO.

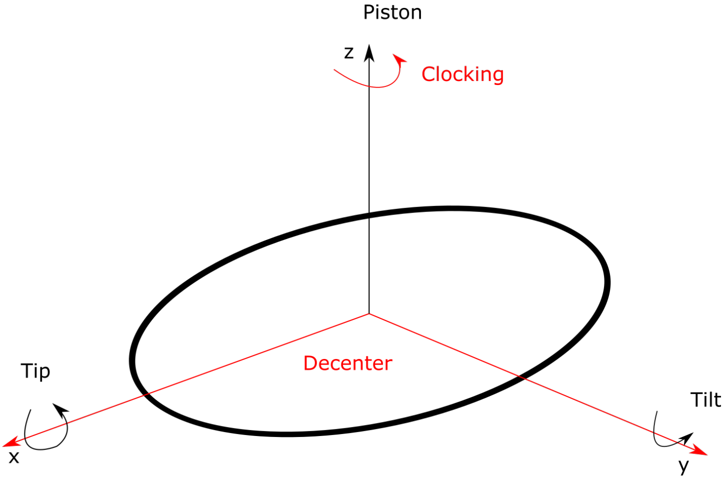

Figure 3.5: Definition of axis convention. The Z axis of the element coincides with the optical axis of the system. Non-controllable DOFs in the PMAO are shown in red.

Table 3.1: Primary mirror tolerances of the DST, broken down by time scale.

Position [μm]			**Tilt [μrad]**			**Radius [%]**	**Shape Error [nm]**
X	**Y**	**Z**	**X**	**Y**	**Z**		
Deployment and Coarse alignment Tolerances							
2	2	2	2	4	50	$1*10^{-3}$	50
In-Orbit Drifts							
$2*10^{-2}$	$2*10^{-2}$	$2*10^{-2}$	$1*10^{-2}$	$2*10^{-2}$	5	$1*10^{-4}$	5
Stability Budgets							
$5*10^{-3}$	$5*10^{-3}$	$5*10^{-3}$	$2.5*10^{-3}$	$1*10^{-2}$	$5*10^{-1}$	n/a	n/a

allowable eigenfrequency for this mechanism is set at 100 Hz. This is considered compatible with the Vega launch vehicle. (**Arianespace, 2014**)

3.2.2. CONCEPT GENERATION

With this approach, the design space is reduced in stages up to the generation of two feasible concepts. The two concepts are then traded off, and the final concept will be further developed and modelled under the expected loads.

In the first step, Freedom and Constraint (FACT) (**Hopkins and Culpepper, 2010a, 2010b**) analysis is applied to discover what the possible arrangements of constraints which deliver the intended DOFs are. FACT allows a complete exploration of the design space. The method as presented here is applied to the synthesis of a parallel mechanism. A serial mechanism can also be analysed with FACT (**Hopkins and Culpepper, 2011**), but is not advantageous for this case. The main reason for this is the small range of motion, in the order of a few microns, required of the mechanism. Other mechanisms for comparable applications, such as the James Webb Space Telescope nanoactuator (**Warden, 2006**) use a two-stage approach due to the need of a larger range of motion, in the order of milimetres, and comparable step size. This is not deemed necessary for the DST, which greatly simplifies mechanism design.

The actuator selection process and material choices follow this analysis. With this information, two concepts were generated and finally traded off. The winning concept was simulated further to check for compliance with the aforementioned requirements and derive further requirements.

3.2.3. MECHANISM CONFIGURATION

The PMAO is a three DOF mechanism for piston, tip and tilt, as required by the top-down system design. FACT allows the designer to discover the potential configurations of constraints for a desired set of DOFs by using a catalogue of different space topologies. For a given set of desired DOFs, the catalogue lists the configuration of complementary freedom and constraints topologies. Within the constraint topology, the designer needs to choose the most convenient combination of constraints. These freedoms and constraints are only

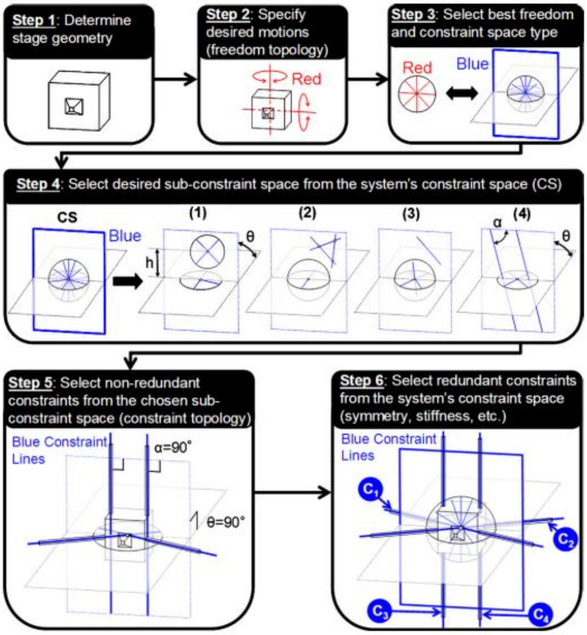

Figure 3.6: Summary of the FACT flexure system design method. (**Hopkins and Culpepper, 2010b**)

valid under the hypothesis of small displacements. The complete synthesis process is illustrated in **Figure** 3.6. Each freedom may be thought of as a free rotation about an axis, whilst each constraint represents an ideal constraint on only one degree of freedom.

The FACT methodology facilitates the selection of the constraint and actuation sets. The former is a set of ideal constraints embodied in wire flexures, whilst the latter represents the actuators, also as ideal constraints. Therefore, the process for the full synthesis needs to be applied twice to find what will be called the 'constraint' set and the 'actuation' set. The juxtaposition of the constraint set and the actuation set of flexures will provide the desired degrees of freedom, but these two are not complementary topologies in FACT terminology.

Regarding the constraint set, piston tip-tilt is a common freedom set in optomechanics, which contains two rotations and one translation. In the FACT terminology, this means a freedom set which contains two intersecting freedom lines and a hoop which intersects both of them at infinity. This freedom set is contained in a hoop and plane topology. The complementary topology is a plane in constraint space. The two complementary topologies are shown in **Figure** 3.7.

For the actuation set, the reasoning is repeated. In this case, the constraint set is the geometric arrangement of the actuators. The shape of this constraint set is a priori unknown, but its freedom set is one that does not contain the previously eliminated piston and tip-tilt DOFs. This freedom set contains two translations and one rotation perpendicular to them. Looking at the FACT library, the actuation constraint set is obtained. Both the constraint

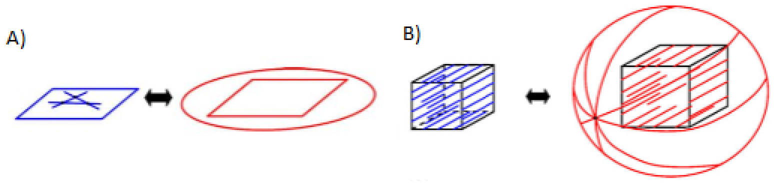

Figure 3.7: Constraint (blue) and freedom (red) topologies for a set constraining the mirror (left) and actuating it (right). (**Hopkins and Culpepper,** 2010a)

and freedom topologies are shown in **Figure** 3.7.

According to this analysis, the PMAO will need to implement at least three independent constraints arranged in the same plane to prevent in-plane translations and out of plane rotations. In addition, it needs to have at least three linear actuators perpendicular to the plane. Redundant constraints violate the principle of exact constraint (**Blanding,** 1999**; Hale,** 1999) and are therefore undesirable. However, redundant constraints are routinely added to precision machinery to control other system parameters such as stiffness or thermal response. It is worth noting that violating exact constraint typically comes at the cost of either internal stresses in the mechanism due to loads introduced to fit different parts together, or higher production costs to produce extremely tight tolerances. These isssues can be offset by manufacturing the overconstraining structure in a monolithic part, therefore negating the need for preloading during assembly.

At this point, other considerations apply to the kinematics of the PMAO. Considering the geometry of the DST, implementing rigid in-plane constraints directly at the centre of mass of the mirrors is impractical. To solve this problem, a moving intermediate frame is introduced in the design. The moving frame is constrained in the manner developed here, and in turn coupled to the mirror via a 6 DOF connection. In this way, controlling the frame's position on 3 DOFs, provides also 3 DOF control of the mirror, with a repeatable and predictable error due to the offset between the two. Another issue is the thermal expansion which the mechanism will experience during operation, and which cannot be constrained by the in-plane constraint flexures. In order to counteract a rotation within the plane of the in-plane constraints, which produces a clocking motion of the mechanism, the flexures will need to be doubled in a symmetric fashion, adding more degrees of overconstraint. A possible schematic for the in-plane constraints is shown in **Figure** 3.8.

This arrangement is free to thermally expand in radial direction, but its thermal centre does not move in this case. Therefore, it is athermal on the constraint plane.

3.2.4. ACTUATOR SELECTION

In order to actuate three degrees of freedom, at least three separate actuators are needed. The actuators produce the prime motion which is transmitted by the mechanism to act on the required DOFs. The type of actuator is based on balancing the demands in terms of power, size and performance. The process to select an actuator is a down-selection from a

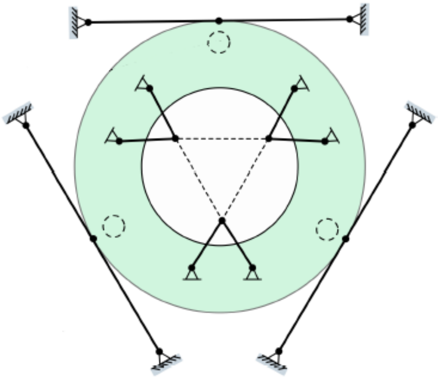

Figure 3.8: In-plane constraint arrangement preventing the clocking motion under thermal stress. In this way, two opposing flexures under the same thermal load will mutually cancel out. (**Pepper, 2018**)

list of candidate technologies. A rigorous systems engineering approach demands that all types of possible solutions be considered. In this process, several types of actuators were quickly discarded as impractical. Very inferior concepts were actuators based on bi-stable materials such as phase-change materials or shape memory alloys. These mechanisms are hardly controllable, much less to the resolution required.

Electrical DC motors or any kind were also rejected because they are more suited for steady state rotatory operation, which is not adequate in this type of mission. Lastly, voice coils were considered due to their large range of motion, linear behaviour and fine resolution. However, voice coils are difficult to cool down in vacuum, and have no inherent stiffness, so they cannot hold a position without constant power draw. In addition, no examples of voice coil actuation were found in the literature, which indicates a low Technology Readiness Level (TRL).

Stepper motors have been the technology of choice for many precision applications in space (**Artiagoitia et al., 2017; Koski, 2008; Urgoiti et al., 2005; Warden, 2006**). They are reliable, have a high TRL and provide power-off hold. Stepper motors however require additional gears, which gives rise to non-linear behaviour, namely backlash and hysteresis. With the ancillary gears and reducers needed, stepper motors are typically massive. The reducer stages also need to be designed, which adds to the design complexity.

The other two candidates are linear piezoelectric and stepper piezo-electric motors. These two types of actuators share the advantages of not requiring lubrication, high power density, high stiffness and strength, high TRL, and magnetic cleanliness. They differ in the type of drive used to move the end effector. A linear piezoelectric stack uses the expansion and contraction components of the piezoelectric effect to drive motion, whilst the steppers alternate either bending or shear modes to 'step' over a surface rigidly connected to the end effector, producing either linear or other types of motion (**Howald et al., 1992**). Both concepts can provide sub-nanometer resolution levels and are commercially available.

Table 3.2: Trade-off criteria for actuator selection as determined by the AHP.

Criteria	**Weight**	**Considerations**
Total Mass	0.180	Mass of the actuator and auxiliary components (additional electronics, transmission) if any.
Volume	0.208	Physical size influences the accommodation that must be made in other parts.
Range and resolution	0.273	Ability to meet actuation needs.
Cost	0.196	Measure of complexity, non-standard interfaces and components required, sensing, or thermal control. Difficulty of integration and testing.
Driving force or torque	0.053	Greater force production is advantageous so that a stiffer mechanism may be used to improve dynamic performance of the mechanism.
Holding force or torque	0.049	The ability to hold a position without power draw eases requirements on the power and thermal subsystems.
Risk	0.041	Lower risk components require less resources for testing and qualification. Improves reliability of the system. Includes auxiliary components/

A preliminary analysis of the performance of these three concepts was performed, to assess the selection criteria described in **Table** 3.2. The analysis is based on a representative actuator model that can be found in the market per actuator type [1]. In this study, commercially available actuators were desired because the authors have no capability to build their own. A tailored actuator would be a potential choice that broadens the design space. This is a choice which is not driven by technical criteria, but rather by programmatic ones.

The trade-off may be structured using the Analytical Hierarchy Process (AHP) (**Zahedi, 1986**). AHP is a decision-making method comprised of four steps: Setting up a breakdown of decision elements, comparing them pair-wise, estimating the relative weight of those elements, and adding them for each decision alternative. Typically the pairwise comparisons are applied to selection criteria to find the criteria ranking, and the different decision alternatives are compared based on these criteria. It is also possible that the criteria can be objectively assessed for each alternative, which removes the need for those comparisons.

Based on the alignment and stability requirements of the DST, resolution in the order of 5 nanometres and range in the order of 10 micron are potentially sufficient to fulfill the requirements, depending on the final configuration of the mechanism. This is highly dependent on the final configuration of the mechanism, which will determine its direct kinematics, but knowledge of the order of magnitude is important to match requirements to components in a first approximation.

Finally the linear piezoelectric actuator was selected based on the AHP trade-off method. None of the concepts were deemed unfeasible. However the stepper motor, despite its considerable heritage was dragged down by the need of a reducing transmission system, which was expected to severely increase mass, volume, and potentially resolution. Of the piezoelectric options, the linear piezoelectric won over the stepper on the basis of its simpler construction, higher rated force, and wider availability of information. Another advantage compared to a stepper motor is the possibility of holding the mirror through launch due to its higher blocked force. A severe deficiency of the linear concept is the lack of power off hold, which could be worked around. A summary of the characteristics of each type of actuator in the trade-off is shown in **Table** 3.3.

More specific requirements flow down on the actuator, such as stroke, size, resolution

---

[1] Cedrat Technologies catalog 5.1 2019.
Physik Instrumente PiezoWalk® Piezomotors
phySPACE StepperMotor Series

Table 3.3: Characteristics of the different types of actuators and final scores.

	Linear Piezoelectric	**Stepper Piezoelectric**	**Stepper motor**
Mass	Good	Good	Minor deficiencies
Volume	Good	Good	Minor deficiencies
Range & Resolution	Excellent	Excellent	Serious deficiencies
Cost	Neutral	Neutral	Neutral
Driving force	Excellent	Good	Good
Holding force	Serious deficiencies	Good	Good
Risk	Good	Neutral	Minor deficiencies
Final AHP score	0.433	0.355	0.212

and operating voltage. This process however requires examination of the mechanism kinematics, which is to be examined in **section** 3.4.

In the process of integration, the actuators need to be bolted to the rest of the mechanism. This procedure introduces a 6 DOFs constraint at the interface, which, for the desired 3 DOFs actuation, would introduce 12 undesired constraints, transmitting high loads both to the fixed frame of the mechanism and to the moving frame. This is typically solved with a flexure joint which releases the unwanted constraints. These joints can be realised as two blade flexures in series, which only share a constraint of one direction along the actuation axis (**Hale, 1999**). With two of these joints, the actuator stack can provide an exact constraint of the motion.

Piezoelectric actuators suffer from severe hysteresis when driven in open-loop voltage control, which is very detrimental for precision applications. The two main approaches to solving this limitation are closed-loop control, and controlling in charge rather than voltage. The closed loop approach can be conveniently implemented via strain gauges bonded to the piezoelectric material, by measuring the strain as a function of voltage (**Fleming and Leang, 2010; Porchez et al., 2016**). Following the same design philosophy as presented in (**Porchez et al., 2016**) to separate the strain gauge signal caused by thermal expansion of the actuators and the intentional piezoelectric effect, it was decided to use two concepts taking advantage of actuators in push-pull configuration.

3.3. MATERIAL CHOICE

The material for this application is expected to provide repeatable deformation behaviour, high stability, and the ability to withstand the launch loads, with minimal mass. In order to fulfil these diverse objectives, several candidate materials are compared to a fictitious material with good properties across the different figures of merit selected for the application. (**Smith and Chetwynd, 1994**) Although this procedure still has an element of subjective choice, it removes the possibility of considering a particular material as the standard choice before due analysis. It is desirable for the design and manufacture procedures to use one material for the entire mechanism. This removes concerns of differential thermal expansion at material interfaces and it is easier to manufacture with minimal contact interfaces. The exception to this rule is the actuator itself. The physical properties of this virtual material (**Smith and Chetwynd, 1994**) are presented in **Table** 3.4.

Table 3.4: Properties of virtual standard material.

Property	**Value**
Young's Modulus E	200 GPa
Yield strength S_Y	300 MPa
Density ρ	4000 kg/m^3
Coefficient of thermal expansion α	7e-6 K^{-1}
Thermal conductivity κ	150 W/m-K
Specific heat capacity c_p	750 J/kg K

Table 3.5: Figures of merit for material selection.

Figure of merit	**Impact on behaviour**	**Desired trend**
S_Y/ρ	Increases strength to weight ratio.	High
S_Y/E	Increases flexure repeatability.	High
E/ρ	Increases natural frequency and decreases self-weight deflection.	High
$\kappa/c_p\rho$	Increases homogeneity of temperatures in the material.	High
$\alpha/\rho c_p$	Decreases dimensional stability in presence of unsteady heat sources for free members.	Low
$\alpha E/\rho c_p$	Increases thermal stresses in presence of unsteady heat sources in clamped members.	Low
α	Decreases dimensional stability in free members for a change of bulk temperature.	Low
αE	Increases thermal stresses in clamped members for a change of bulk temperature.	Low
α/κ	Decreases dimensional stability in presence of steady state heat sources for free members.	Low
$\alpha E/\kappa$	Increases thermal stresses in clamped members in presence of steady state heat sources for clamped members.	Low

The figures of merit are defined from simple characterizations for the different physical situations that the material experiences during operation. The method was devised by Chetwynd (**D. G. Chetwynd, 1987, 1989**) for applications in precision engineering where the thermal properties are as important as the elastic properties of materials. The figures of merit provide a quantitative characterization of the performance of a material in a particular circumstance which can be found in precision engineering applications. These figures of merit are summarised in **Table 3.5**.

The candidate materials are mostly metals used widely in the aerospace industry, which are known to have good performance in similar applications. Aluminium and titanium alloys are contenders due to their high specific strength. Beryllium is also considered because it is lightweight, stiff, and thermally conductive. Beryllium also has the advantage of very low cumulative shrinkage when cooled to cryogenic temperatures, but this is only relevant for cryogenic observatories such as the James Webb Space Telescope. Magnesium is very lightweight and has high specific strength and high thermal capacity. Stainless steel is not a conventional aerospace material due to it's high density, but it is strong and easy to work into shape. The final material is Invar-36, which has a very small coefficient of thermal expansion compared to the other materials. **Table 3.6** shows the material properties of the candidate materials.

The material characterization method can be complemented with the AHP to make a decision. In this case, since the figures of merit are defined from physical characteristics compared to a fictional material, only the weights of the different criteria need to be determined via pairwise comparisons. This is a hybrid approach, as AHP is a relative method and the figures of merit are absolute. The wide disparity of the material profiles tilts the trade-off heavily to extreme values in some characteristics whilst the material may have poor properties in all other characteristics. In order to avoid this effect, a cap on the maximum score per category was set as five times better than the reference fictional material. With this, the

Table 3.6: Candidate construction materials.

	ρ[kg/m^3]	E [GPa]	ν	S$_Y$	$\alpha[x10^{-}6/K]$	κ[W/(m K)]	c$_p$ [J/kgK]
Aluminium 6061	2680	68	0.33	276	23.6	167.0	896
Aluminium 7075	2790	72	0.33	503	23.4	142.0	896
Beryllium I-70	1850	303	0.08	350	11.3	194.0	1900
Beryllium-Copper	8250	127	0.35	1340	17.8	100.0	380
Invar 36	8050	141	0.26	276	1.26	10.4	460
Magnesium AZ31B	1770	45	0.35	255	25.2	97.0	1000
304 Stainless Steel	8000	193	0.27	276	14.7	16.2	500
Titanium 6Al-4V	4400	115	0.33	1060	8.6	7.2	565

final score for each alternative can be calculated as:

$$FS_j = \sum W_i FOM_{ij} \tag{3.1}$$

where W_i are the weights calculated via pairwise comparison and FOM are the figures of merit for alternative j. With this trade-off methodology, the winning material was Ti6Al4V.

3.4. CONCEPT TRADE-OFF

The two concepts use a moving intermediate frame which effectively acts as mechanism end effector. With a six DOF rigid connection between the moving frame and the mirror, the kinematics of the mirror are fully determined knowing those of the moving frame. From now on, the moving frame's inverse kinematics will be the main interest. The introduction of the moving frame adds a repeatable offset between the intended degrees of freedom as defined at the mirror's centre of mass and the centre of the moving frame.

This offset is tolerable for a small range of tip/tilt actuation. The largest error introduced by this offset δY_S is a decentre motion which can be calculated as:

$$\delta Y_S = h \sin \theta_{XMF}. \tag{3.2}$$

Figure 3.10 defines the terms in equation 3.2. The error introduced here was later confirmed to be acceptable during end-to-end modelling (**Pepper, 2018**).

The moving frame is constrained in three degrees of freedom as explained in **section 3.2.3**. It is also connected to the mirror via six flexured struts forming a hexapod mount that transmits no bending loads to the mirror.

3.4.1. CONCEPT A: THREE LINEAR ACTUATORS.

The first concept proposed uses three assemblies of coupled push-pulled actuators mechanically connected in series (**Porchez et al., 2016**). These assembly are referred to as a Nanometric Linear Actuators (NLA) by their creators at Cedrat Technologies. The strain gauges used for closed loop control are connected in a Wheatstone bridge configuration. As long as there is no significant thermal gradient between the piezoelectric elements in the assembly, these are insensitive to temperature changes. These assemblies connect the

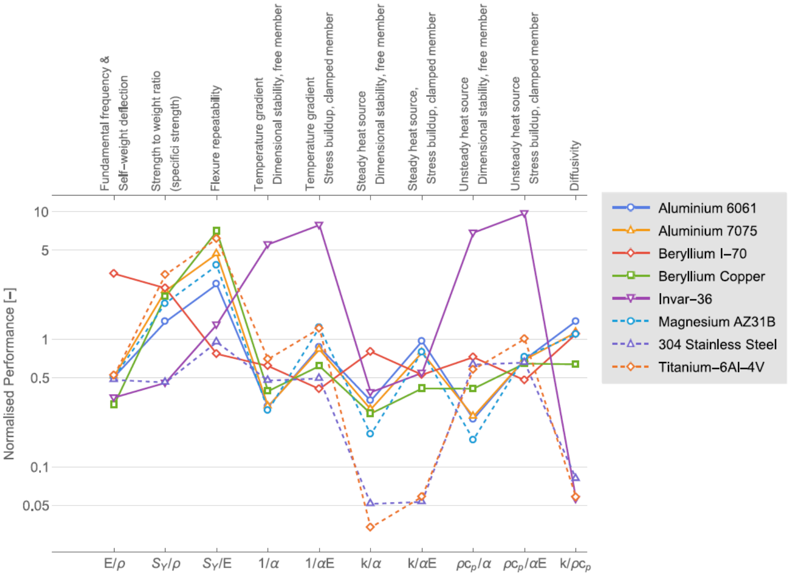

Figure 3.9: Figures of merit for the different candidate materials. Note the lines joining the dots are only for visual emphasis and have no physical meaning. Reprinted from (**Pepper, 2018**) using a method reported in **Smith and Chetwynd, 1994**.

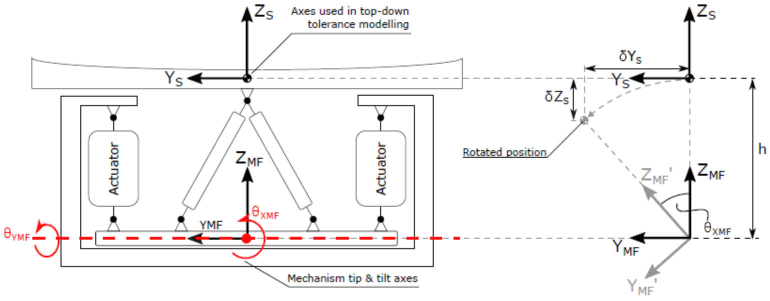

Figure 3.10: Schematic showing the systematic error in mirror pose for a given tip/tilt motion of the moving frame. (**Pepper, 2018**)

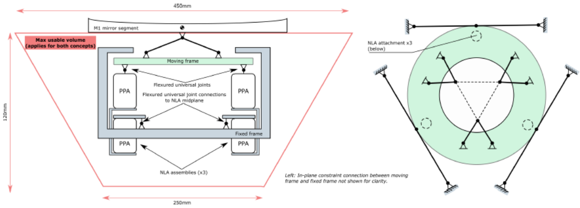

Figure 3.11: Schematic of concept A. (**Pepper,** 2018)

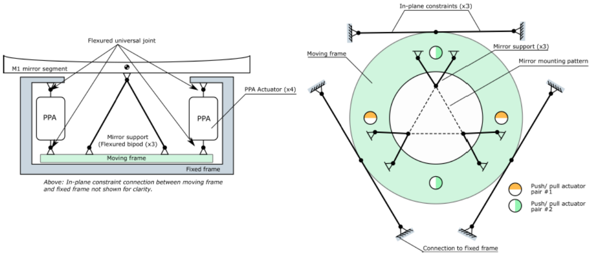

Figure 3.12: Schematic of concept B. (**Pepper,** 2018)

fixed and moving frames through flexure joints which ensure pure piston input. The three assemblies are arranged at 120^o intervals on the moving frame circumference. A schematic of concept A is shown in **Figure** 3.11.

3.4.2. CONCEPT B: FOUR LINEAR ACTUATORS.

The competing concept uses four parallel pre-stressed actuators (PPA) actuators directly connecting the fixed and moving frame. In this case the push-pull pairs are on opposing sides of the moving frame. The need to maintain a small temperature difference remotely may be a killer requirement for this concept. This limitation could be off-set with the use of a temperature sensor on the strain gauge. However, this would negate the point of the Wheatstone bridge configuration and the actuators could be moved independently This concept however does not rely on a custom-made assembly to provide the sensing needed.

This configuration introduces an overconstraint in the piston tip-tilt actuation set, but it is less overconstrained than concept A, since the nanometric linear actuator assembly relies on two actuators per actuated degree of freedom. It was therefore deemed likely lower cost because avoiding overconstraint is one of the factors in reducing manufacturing costs (**Blanding,** 1999). In addition, the four actuators in parallel allow more spread of the launch loads if the actuators act as load carrying, because of the presence of four load paths as opposed to three. The schematic of concept B is shown in **Figure** 3.12.

Table 3.7: Trade-off summary for the two concepts.

	Concept NLA	Concept PPA
Mass	Good	Good
Volume	Minor deficiencies	Good
Performance	Good	Good
Cost	Serious deficiencies	Minor deficiencies
Risks	Serious deficiencies	Neutral
Final AHP score	0.481	0.519

3.4.3. TRADE-OFF

The two concepts were evaluated for mass, volume, kinematic and structural performance, cost and risks. Again, the AHP is used to structure the trade-off. Both concepts were estimated to have similar masses because the mass of the actuators is a very small part of total system mass. Control electronics are expected to have similar mass. At this stage it is no apparent which of the two concepts would have a more massive ancillary structure. Stowed volume for concept A, compared to concept B, was expected to be larger due to the need to accommodate the NLA in the critical piston direction. Both concepts are expected to be able to meet kinematic performance requirements and survive launch and operations. In the categories of cost and risk, the NLA was deemed likely to drive costs higher due to the additional complexity of coordinating six actuation stacks as opposed to four. Also, these assemblies are custom parts which are not easily found in as commercial off the shelf components, so they are also worse for programmatic considerations. Concept B was finally selected. The final trade-off table is shown in **Table** 3.7.

3.4.4. INITIAL SIZING

The overall size of the mechanism is determined by the allowable space behind the mirror that is not allocated for other systems. This is limited by the DST requirements on total cross section in stowed configuration, combined with the space needed for the deployment struts which support the secondary mirror. The first sizing parameters can be iterated upon later when the sensitivities of the system performance are calculated, but some considerations need to be taken into account to produce a reasonable first approximation and constrain the design space.

One of these considerations for this mechanism is the gravity sag of the mirror when supported by the mechanism. A detailed analysis of the tapered area of the mirror was not possible at this stage. Yoder and Vukobratovich (**Yoder and Vukobratovich,** 2015) provide a design rule for back mounting of circular mirrors. In the case of homogeneous circular mirrors the sag can be minimised with a three-point mount placed at a 0.645 fraction of the radius. Minimising gravity sag is advantageous for ground testing and alignment operations, although not so important in space operations. Applying their design rule, the mirror support radius was set by using the inscribed circumference in the mirror segment. A bigger support radius for the actuation stacks is beneficial to increase the effectiveness of the actuator on tip-tilt, but is limited by the need to avoid clashing with the bipods.

Other lower level parameters, such as flexure thickness and length, were set using rough estimates of the loads on the mechanism during launch or thermal expansion. In addition, elements which are too thin may not be practical for manufacturing.

The linearised inverse kinematics of interest for this study are those of the moving frame, because the mirror is rigidly connected to it with the repeatable offset shwon in **Figure** 3.10. These are given by:

$$\Delta L_I = R_M\theta_y + \Delta z \tag{3.3}$$

$$\Delta L_{II} = R_M\theta_x + \Delta z \tag{3.4}$$

$$\Delta L_{III} = -R_M\theta_y + \Delta z \tag{3.5}$$

$$\Delta L_{IV} = -R_M\theta_x + \Delta z \tag{3.6}$$

where Δz is the piston displacement and θ_x and θ_y are the in-plane rotation angles. The ΔL are the changes in length of the four actuators.

3.5. MECHANISM MODELLING

Mechanical modelling has the objective of assessing survival of the mechanism during testing, launch and operational situations, as well as checking its kinematic performance. The software SPACAR (**van Soest et al.,** 1992), which is implemented as a toolbox for MATLAB, was used to perform this modelling. SPACAR is built upon non-linear finite element theory and is intended to analyse mechanisms with multiple DOFs and has been used on prior research work. (**Meijaard et al.,** 2010**; Meijaard et al.,** 2007**; Naves et al.,** 2020). For this application, the main limitations of SPACAR are the lack of implemented shell or solid elements in its finite element formulation. For this study, this limitation is not relevant since the elements which cannot reasonably be approximated as thin flexures are meant to act as rigid bodies. Therefore these rigid bodies are substituted in the model with a rigid connection between flexible elements. SPACAR can accurately model blade flexures with small aspect ratios. This was verified with a separate model for the actuator flexure joint. Results given by SPACAR were similar to those provided by commercial FEA software Ansys in terms of buckling load, deflection and first eigenfrequency, with deviations between the two in the order of 5% (**Pepper,** 2018).

The actuators are modelled as a single element with the stiffness reported by the manufacturer. Actuator commands are simulated with the application of a virtual preload. The value of this preload P_{act} is calculated as:

$$P_{act} = S_{act}\delta. \tag{3.7}$$

With S_{act} being the stiffness of the actuator and δ is the desired stroke of the actuator. In an experimental setup, the real input would be a voltage or a current which would translate to a force through a transfer function. The specifics of the control system are outside of the scope of this work. Here, the assumption is that such force can be controlled precisely.

In this section, mechanical modelling is concerned with the integrity of the mechanism under launch loads, and its performance during operations. On the topic of performance, the flexibility of SPACAR allows for verification of the linearised kinematics presented in **subsection** 3.4.4 and therefore it can show that the mechanism works as intended within the limitations of the model.

3.5.1. DYNAMIC CHARACTERIZATION

Characterising the dynamics of the mechanism serves the dual purpose of evaluating the survival of the mechanism, and define requirements for the controller. In this section, this information is only used to assess the survivability as per the criterion described in **section** 3.2. In this case, the criterion is simply a first eigenfrequency above 100 Hz. A linear eigenfrequency analysis was conducted on SPACAR to find this eigenfrequency and the first vibration modes. The results show a first eigenfrequency of 198 Hz, and the first mode associated is a clocking motion of the moving frame about the mechanism's piston motion. The next two modes are translations of the moving frame in its own plane.

3.5.2. STATIC LOAD SURVIVAL

The setup was simulated when subjected to a static load equivalent to a combined acceleration of 30 g on two axes simultaneously. Twelve cases were ran to cover all combinations of two axes with positive and negative loads respect to the chosen reference frame. The first criterion was that the stresses shall be below the yielding stress of the material. Each element of the model was evaluated on the worst case tension and worst case compression stresses. In compression of slender elements, the buckling stress was used as failure criterion. Actuators were not analysed as bulk materials because they are complex parts with several components. Instead the total axial force was computed and compared to the rated blocked force reported by the manufacturer. The Margin Of Safety (MOS) was calculated as

$$MOS = \frac{\sigma_{failure}}{\sigma_{max}} - 1 \tag{3.8}$$

where $\sigma_{failure}$ is the maximum stress a component can resist and $\sigma_m ax$ is the worst case stress computed by the model. The minimum margin of safety found in this procedure was of 0.33 corresponding to the actuators, which is acceptable.

3.5.3. OPERATIONAL LOADS

The purpose of the operational loads analysis is to verify the operational kinematics of the mechanism, as well as confirming that the operation does not produce stresses beyond the yield stress of the material. It is also the only operational regime in which the actuators are powered on. In order to assess these loads, the actuators were be driven to the boundaries of the range of motion of the mechanism. The stresses in these cases were verified to be below those of the static loads and this is therefore confirmed not to be a limiting case.

An interesting implementation of these simulations is the integration of these loads with the ray-tracing software FORTA (Fast Optical RayTrace Application) (**Dolkens, Marrewijk, et al.,** 2018), which allows end-to-end modelling of the effect of the mirror pose with the final image quality. A more complete version of this analysis was previously presented by

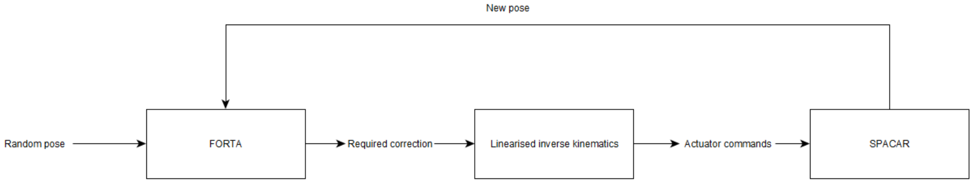

Figure 3.13: Structure of the integrated simulation control loop with FORTA and SPACAR simulations.

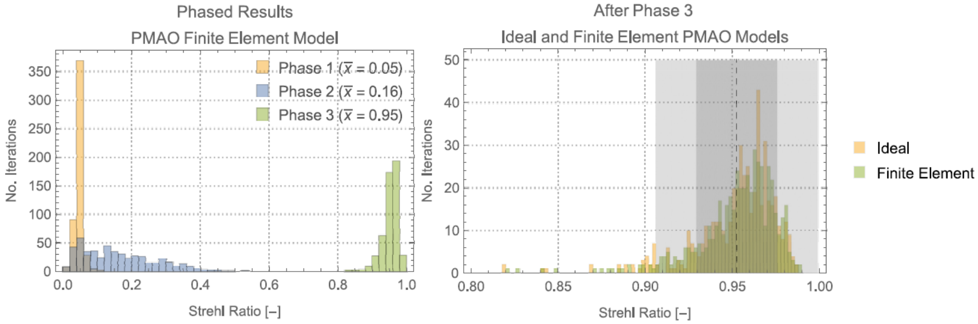

Figure 3.14: Results of MonteCarlo simulations after each phase of the phasing strategy for the DST. The results on the left show the image quality (**Pepper,** 2018).

Pepper (**Pepper,** 2018) as executed by Dennis Dolkens. A disturbance to a desired pose is introduced to the optical ray tracer, which produces commands which are in turn translated into actuator strokes. These are an input for SPACAR, which calculates the final pose of the mechanism, and this is the new input for FORTA. the process is ilustrated in **Figure** 3.13. The SPACAR model of this mechanism was compared to an ideal mechanism. The Strehl ratio of the optical system was computed for a number of randomly generated initial mirror poses over the course of the phasing procedure. **Figure** 3.14 shows that the performance of the mechanism, as modelled, is sufficient to provide the desired final image quality, as defined by a Strehl ratio greater than 0.8.

3.5.4. THERMAL MODELING

Temperature changes are a classical problem when designing optical instruments. Three usual approaches are described by Bely (**Bely,** 2003) to athermalise an optical system: Passive athermalization, passive compensation, and active compensation. These are mentioned here in order of preference, because of their increasing impact in system complexity or power requirements. These strategies are designed for a bulk temperature change for which the system is free to expand, but with the essential elements remaining in place to the desired accuracy.

In order to assess the need for these techniques, the first step is finding the temperature distribution within the mechanism in its real environment. The environment of the mechanism was therefore simulated with a top-down thermal model of the telescope, de-

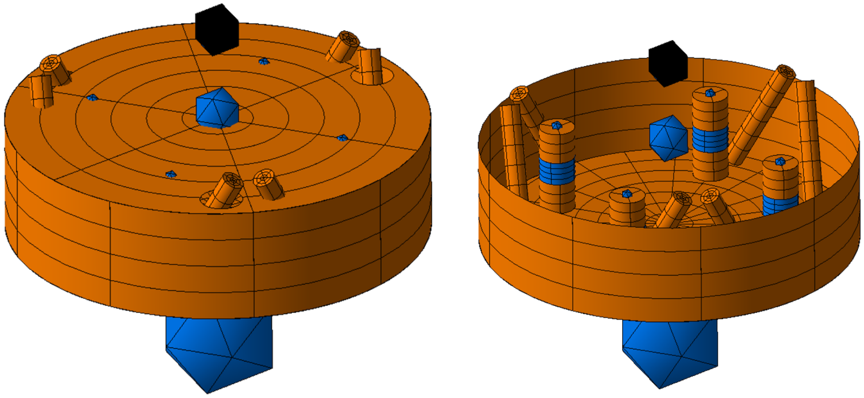

Figure 3.15: Geometry of the thermal model. The colour orange corresponds to parts made out of Al7075 and the blue parts are the actuators. The floating "balls" represent non-geometric thermal nodes in the model.

veloped over several stages by MSc students at the Delft University of Technology (**Arink,** 2019**; Wees,** 2019). The top down model is built on the software ESATAN. In this software, the geometry, materials and attachments of the telescope are introduced as input parameters. The geometry is broken into isothermal nodes, which act as lumped thermal masses. The software calculates the radiative exchange factors (**Gebhart,** 1961) and the conductive coupling coefficients. Convective couplings are not present in this model. The top down model also implements the operational orbit of the telescope, and the view factor of all the nodes to the cold space. With this, the boundary conditions of the model are established and the temperature is calculated by integrating the system of heat equations for all the nodes. The geometry used for this model is shown in **Figure** 3.15.

The resulting temperature field is taken as the input for the bottom-up thermal model of the PMAO. The fundamental assumption in this step is that the temperature distribution in the PMAO does not affect that of the telescope, because it is a system with larger heat inputs and thermal mass. This uncoupling permits the analysis of the temperature distribution in the mechanism in a separate model independently from the orbital parameters.

The PMAO thermal model uses the same underlying physics as the top down model, but it interacts with virtual heat reservoirs which represent the temperature field found in the top-down model. The only expected internal heat production of the mechanism is related to the self-heating of the actuators. This self-heating is related to the force required of the actuators at different working frequencies. Several models exist to approximate this heating effect (**Lu and Hanagud,** 2004) from first principles, but they are complex and dependent on boundary conditions, which limits their applicability. The impact of actuator in a system like this is not known at this point, and will be explored in **Chapter** 5. The baseline thermal case does not include self heating.

Another significant source of uncertainty in this computational approach to thermal design is estimating the conductances of the joints present in the design. To offset these

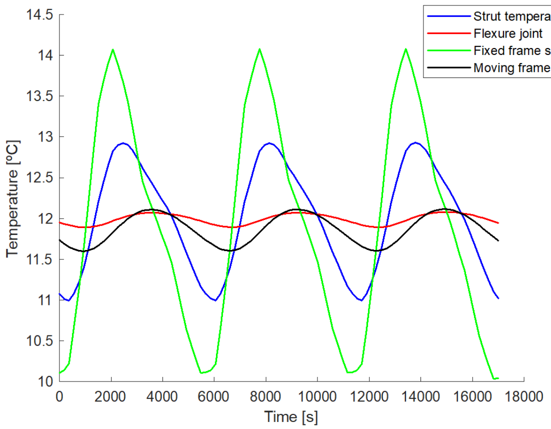

Figure 3.16: Temperature profiles for different parts of the mechanism, showing the delay between the maxim of the different temperature profiles.

issues, a sensitivity analysis implementing a sweep of both actuator heat production and joint conductance values was performed. Joint conductance is notoriously difficult to estimate a priori due to the large amount of parameters involved which are not available at early design stages.

The results of the sensitivity analysis show that temperature in the PMAO, as designed, is not homogeneous. This is not surprising because the top-down model predicted different temperatures for the several heat reservoirs that act as boundary conditions to the model, and therefore a homogeneous temperature would be inconsistent. Different temperature profiles for different parts of the mechanism are shown in **Figure** 3.16 The only thermal requirements at this stage is for the actuators to remain below their rated temperature and that the two actuator in push-pull configurations have a 0.01 K difference. These requirements were met in the thermal model currently available, but there is not enough information to verify them. In this section, an effort will be presented to comply with thermo-elastic stability requirements, that is to keep thermal deformations below requirements.

3.5.5. THERMAL-MECHANICAL MODEL

The mechanism does not have imposed requirements on its temperature. Thus the first task is to assess how much misalignment the expected temperature field produces. In order to do this, a thermal internal stress can be introduced in the SPACAR model presented in **section** 3.5:

$$P_T = \alpha L \Delta T \tag{3.9}$$

where α is the material coefficient of thermal expansion, L is the element length, and ΔT is the temperature difference between each time step and the average temperature of the mechanism over a cycle. This case is analogous to the virtual preload introduced to model actuation loads, but it is applied to all elements in the system. A thermally induced bending moment could also be introduced in the model, if large radial temperature differentials were observed in the thermal model.

For the analysis, thermal deformation of the mechanism was broken down into six thermoelastic modes in which different elements expand independently, according to the temperatures of the involved parts. Note that these modes are chosen as part of the modeling and are not inherent thermal modes of the mechanism (**Morishima et al., 2015**). Each case's influence on the mirror's final pose **M** is linearly superposed with the others to calculate a total displacement as:

$$\mathbf{M}_T = \sum_i \mathbf{M}_i. \tag{3.10}$$

This breakdown helps with validating the model, as each of these cases can be compared to a simplified analytical model. These elements are based on reducing the mechanism to a one degree of freedom model in which the expanding elements behave as prismatic actuators and are connected by rigid bodies, ignoring the effect of stiffness or stress relief in the flexures. This was done as the main model validation activity in which the piston displacement of the mechanism for each case was compared to a quick model achieving comparable results.

This load case breakdown also helps in diagnosing a non-compliance, as the influence of the different load cases relates to specific system parameters, and therefore guides the changes needed for compliance. The temperature change process is assumed to be quasi-static over the orbit, as its characteristic period is much longer than the actuation cycle, which is in the order of hundredths of a second.

A limitation of this approach is the mapping of temperature fields to the mechanical mesh, because these are generated on different softwares without a simple interface. The process of matching those meshes can be time intensive. In order to provide a faster way to integrate the design, and using the beam element properties, the average element temperature is used in the thermoelastic model. The underlying assumption here is that given a cantilever beam of length L which expands longitudinally subjected to a temperature field $\Delta T(x)$, with x being a coordinate along the beam, the total expansion is given by:

$$\Delta L = \int_L \alpha \Delta T(x) dx. \tag{3.11}$$

If α is constant and $\Delta T(x)$ is a continuous and integrable function, then using the mean value theorem for definite integrals:

$$\Delta L = \alpha \Delta T_{mean} L \tag{3.12}$$

with ΔT_{mean} being the mean value along the beam.

CASE 1: FLEXURE JOINTS

Expansion of the joint flexures and frustum produces a similar change in pose similar to a change in length of the actuator. Since the flexure joint does not have a large stiffness, the motion is in principle a pure piston motion. Different temperature profiles apply to each joint, so tip-tilt motion may happen if the temperature field is not symmetrical across the mechanism. **Figure 3.17** shows the piston deviation caused by the flexure joints calculated in SPACAR and in the analytical model.

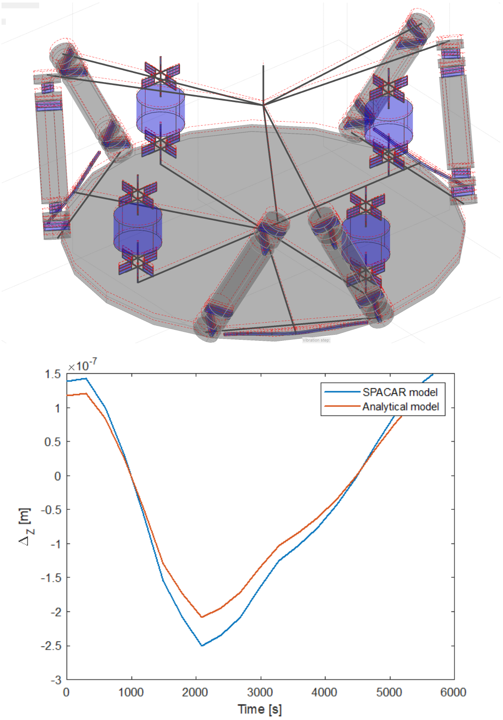

Figure 3.17: Deviation over time caused by thermal fluctuations of the flexure joints (case 1). Top figure displays the case shape, the bottom figure shows computed piston values with SPACAR and analytical models.

CASE 2: HEXAPOD EXPANSION.

The hexapod is a 6 DOF connection realised with flexured struts. Solving the kinematics of this type of connection is not the focus of this work, although solutions exist for both the direct and inverse kinematics of a Stewart platform (**Furqan et al., 2017; Stewart, 1965**). Here the pose calculation is solved using SPACAR, and analytical verification is only valid for piston motion. **Figure 3.18** shows the piston deviation caused by the bipods temperature change.

CASE 3: ACTUATION STACK EXPANSION

This load case is analogous to the regular actuation of the mechanism, the influence of which is described already by the mechanisms' kinematics. However it is a useful case for verification of the model. The three actuation DOFs are affected by this mode, but note that, in the critical DOF of the piston, this load case runs contrary to cases 2 and 4, which for a positive increment of temperature cause a positive piston motion, as shown in Figure. This means that cases 1 and 4 provide a measure of passive athermalization. The same is true for case 5. The effect of the temperature of the actuators on the pose is shown in **Figure 3.19**.

CASE 4: FIXED FRAME EXPANSION

The fixed frame is not designed in detail here, and only the condition that it should be much stiffer than the rest of the mechanism is present. Given this condition, its expansion is ide-

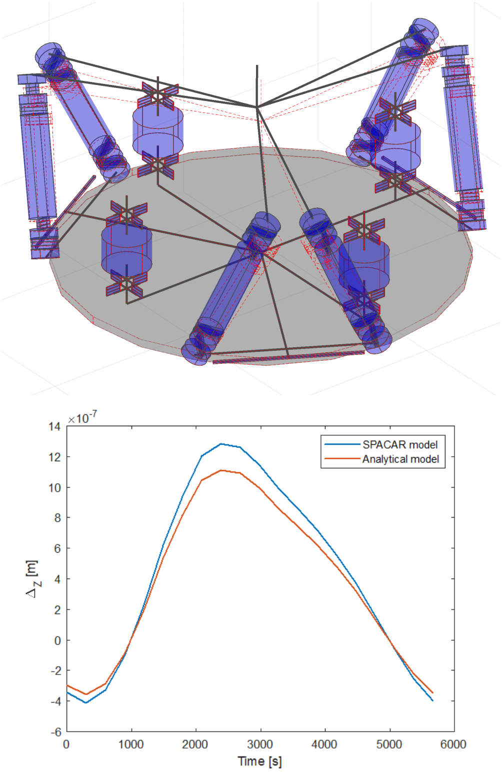

Figure 3.18: Deviation caused by thermal expansion of the flexured bipods (case 2).Top figure displays the case shape, the bottom figure shows computed values with SPACAR and analytical models.

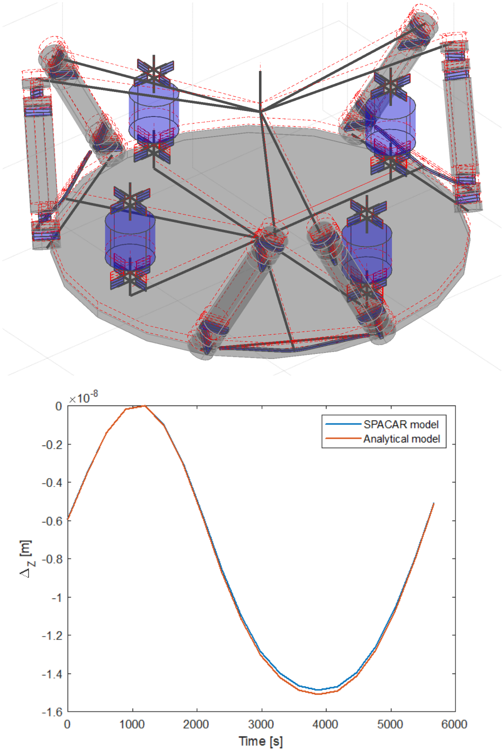

Figure 3.19: Deviation caused by actuators' expansion (case 3). Top figure displays the case shape, the bottom figure shows computed values with SPACAR and analytical models.

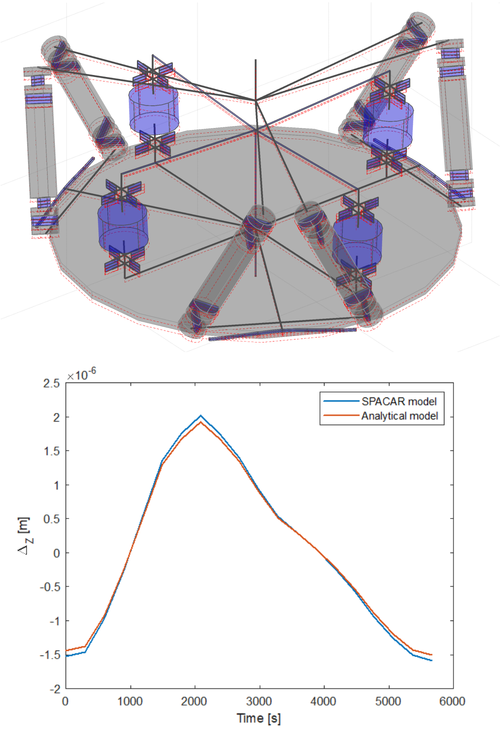

Figure 3.20: Deviation caused by a shift in boundary conditions (mode 4), reproducing expansion of the fixed frame.

alised via a construction that allows radial and vertical deformations, but no other motions. SPACAR is unable to deal with shell or solid elements in its formulation, so the validity of this model is difficult to assess. Here a reason why this model is accepted is because the temperature field in the moving frame was deemed sufficiently uniform that although hoop stresses may develop, these would not cause a clocking motion of the attachment points of the joint flexures. **Figure** 3.20 shows the modelled piston displacement caused by the fixed frame.

CASE 5: MOVING FRAME RADIAL EXPANSION

The limitations mentioned in the case of the fixed frame also apply to the moving frame, since it is a plate which cannot be approximated with one beam element. However the temperature was also homogeneous and the same arguments apply for its validity. Load case 5 was difficult to validate analytically, due to the greater moment absorbed by the flexures at the bottom of the struts, the top flexures behave nearly like rigid bodies in the numerical model. Such behaviour produces zero displacements if the mirror connection is modelled rigid. Displacements in this case are very small compared to the others and due to the top hinges not being perfectly rigid.

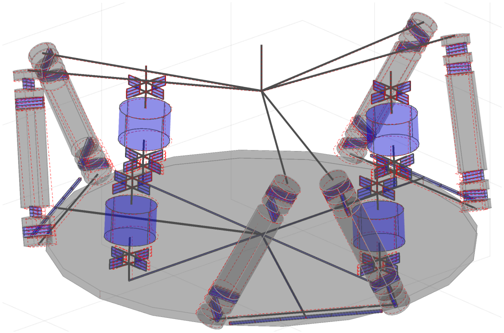

Figure 3.21: Deviation caused by the moving frame thermal expansion.

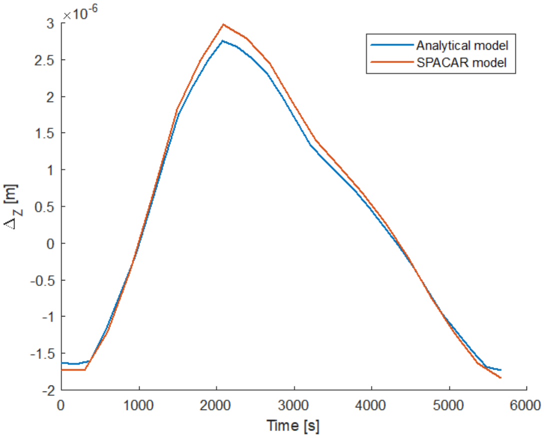

Figure 3.22: Combined deviation calculated as superposition of cases in SPACAR and analytically.

ATHERMALIZATION APPROACHES.

The total pose change in piston over an orbit is shown in **Figure 3.22**. No change in the other pose parameters was proven beyond Matlab's numerical precision. In order to accommodate the deformations caused by temperature fluctuations, the interface between the mirror and the flexured struts may be used. Other interfaces, such as the fixed frame with the flexure joints, or the moving frame with the bipods, can also be used, but the temperature fluctuations are highest when closest to the mirror, and therefore a smaller spacer can be used to greater effect. The implementation of such spacers can be visualised in **Figure 3.23**.

The length of the spacer can be simply found as:

$$h_{spacer} = \frac{\Delta Z_{Max}}{\alpha_{Sp}\Delta T_{Spacer}}. \tag{3.13}$$

ΔZ_{Max} is the largest thermal displacement modelled without spacer, α_{Sp} is the coefficient of thermal expansion of the spacer material, and ΔT_{Spacer} is the temperature differential corresponding to the largest displacement. Pepper (**Pepper, 2018**) suggested this idea,

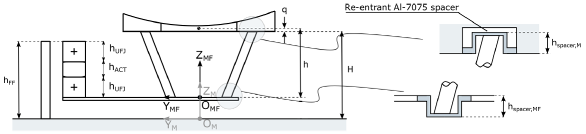

Figure 3.23: Schematic showing the implementation of aluminum spacers to compensate for piston deviation.

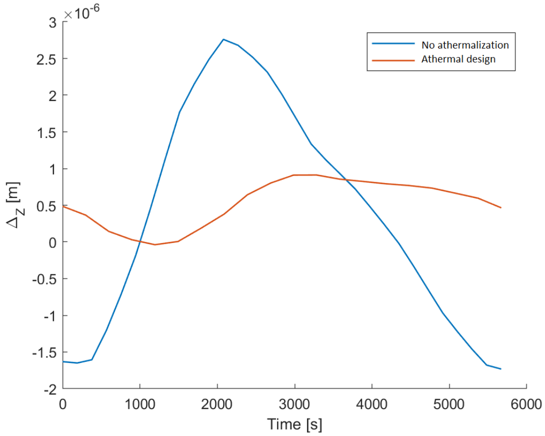

Figure 3.24: Drift produced by orbital thermal fluctuations with and without athermalisation.

but had no quantitative metrics for the spacer temperature or an estimate of performance. A spacer used in this way needs to be integrated with the mirror back. This is easy to do with an open back mirror structure, but may cause integration problems with a closed back mirror. In this project, no specific requirements were set in this regard.

This approach is not sufficient in practice to bring total thermal drift to zero, but it is sufficient to bring it within calibration range by the actuators. This means thermal disturbances can be rejected, but at the cost of actuation stroke available for other disturbance rejection. The reason for this is the difference in thermal response times between different components. The drift accommodated by the spacers compared to the mechanism without spacers is shown in **Figure 3.24**.

In this case however, the spacer needed to compensate for the maximum displacements is too large to be practically integrated with the design. This can be solved with active temperature control of the interface, ensuring a larger temperature swing which makes the spacer more effective at accommodating thermal fluctuations. This involves heat leaking to the rest of the system, altering the total misalignment, so several iterations are required to find a compliant solution. Other passive modifications to the temperature field can be used, such as insulating part of the mechanism to confine heat to the spacers o other areas used for compensation. An easier possibility is identifying the modes with the largest influence in the total misalignment figures, and changing them to a lower CTE material. Note that strength metrics need to be re-evaluated if this is done.

Table 3.8: Requirement compliance matrix for the PMAO.

Requirement	**Computed value**	**Compliance (Y/N)**
Eigenfrequency >100 Hz	198 Hz	Y
30g loads with MoS >0.2	0.23	Y
Stroke >4 μm piston	4 μm	Y
Stroke >4 μrads tip/tilt	4 μrads	Y
Resolution <10 nm	10 nm	Y
Actuator temperature difference <0.01 K	0.0037 K	Y

Note that all the results are only valid to the level of accuracy of these models.

3.6. FUTURE WORK

Once the models are set up and verified, it is possible to perform multiple analyses that lead to an optimal configuration to take to following design stages. Given such baseline configuration, following analysis steps may focus on changing kinematic, thermal, or structural elements in the design. The first step is to check compliance with the requirements via a requirement compliance matrix as presented in **Table** 3.8.

A possible approach to this process is proposing a list of small changes and evaluating their effect on the final performance of the mechanism, creating a sensitivity matrix for each one of the design parameters. As of the current iteration, the design can meet the requirements laid out initially. However, passive thermal-mechanical stability depends on the possibility of integrating a high CTE spacer into the connection to the mirror, which imposes restrictions on the geometry of the mirror back plane.

3.7. CONCLUSIONS

A systematic design process for early stage mechanism development has been presented and applied to an active optics mechanism for deployable telescopes. This can serve as a guideline for early development of mechanisms whilst taking into account the multidisciplinary nature of a real design process. Straightforward systems engineering tools are used to facilitate the construction of arguments for or against different design choices. The main tools needed to evaluate the physical behaviour of the mechanism are presented, as well as their limitations. They also allow for relatively easy iteration for optimisation purposes. This work illustrates the use of these tools for proposing mechanism configurations in the case of a deployable space telescope's active optics mechanism. Future work will need to investigate the thermal behaviour of piezoelectric actuators and investigate if their self heating can cause misalignment problems.

BIBLIOGRAPHY

Arianespace. (2014). Vega User's manual Issue 4 - Revision 0.

Arink, J.-W. (2019). *Thermal-Mechanical Design of a Baffle for the Deployable Space Telescope*.

Artiagoitia, A., Compostizo, C., & Rivera, L. (2017). Euclid M2 mirror mechanism. *ESMATS 2017*, (September).

Bely, P. Y. (2003). *The Design and Construction of Large Optical Telescopes*. Springer.

Blanding, D. L. (1999). *Exact constraint : machine design using kinematic principles*. ASME Press.

Chetwynd, D. G. (1987). Selection of structural materials for precision devices. *Precision Engineering*, *9*(1), 3–6. https://doi.org/10.1016/0141-6359(87)90002-X

Chetwynd, D. G. (1989). Materials classification for fine mechanics. *Precision Engineering*, *11*(4), 203–209. https://doi.org/10.1016/0141-6359(89)90030-5

Corvers, M. (2018). *Design of the Deployment Mechanism for the Primary Mirror of a Deployable Space Telescope*.

Dolkens, D. (2015). *A Deployable Telescope for Sub-meter resolution from MicroSatellite Platforms*.

Dolkens, D., Kuiper, H., & Villalba Corbacho, V. M. (2018). The deployable telescope: a cutting-edge solution for high spatial and temporal resolved Earth observation. *Advanced Optical Technologies*, *7*(6).

Dolkens, D., Marrewijk, G. V., & Kuiper, H. (2018). Active correction system of a deployable telescope for Earth Observation. In Z. Sodnik, N. Karafolas, & B. Cugny (Eds.), *International conference on space optics—icso 2018* (pp. 1–11). https://doi.org/10.1117/12.2535929

Fleming, A. J., & Leang, K. K. (2010). Integrated strain and force feedback for high-performance control of piezoelectric actuators. *Sensors and Actuators, A: Physical*, *161*(1-2), 256–265. https://doi.org/10.1016/j.sna.2010.04.008

Furqan, M., Suhaib, M., & Ahmad, N. (2017). Studies on Stewart platform manipulator: A review. *Journal of Mechanical Science and Technology*, *31*(9), 4459–4470. https://doi.org/10.1007/s12206-017-0846-1

Gebhart, B. (1961). Surface temperature calculations in radiant surroundings of arbitrary complexity—for gray, diffuse radiation. *International Journal of Heat and Mass Transfer*, *3*(4), 341–346. https://doi.org/10.1016/0017-9310(61)90048-5

Hale, L. C. (1999). *Principles and Techniques for Designing Precision Machines* (Doctoral dissertation). Massachusets Institute of Technology.

Hopkins, J. B., & Culpepper, M. L. (2010a). Synthesis of multi-degree of freedom , parallel flexure system concepts via Freedom and Constraint Topology (FACT) – Part I : Principles. *Precision Engineering*, *34*(2), 259–270. https://doi.org/10.1016/j.precisioneng.2009.06.008

Hopkins, J. B., & Culpepper, M. L. (2010b). Synthesis of multi-degree of freedom , parallel flexure system concepts via freedom and constraint topology (FACT). Part II : Practice. *Precision Engineering*, *34*(2), 271–278. https://doi.org/10.1016/j.precisioneng.2009.06.007

Hopkins, J. B., & Culpepper, M. L. (2011). Synthesis of precision serial flexure systems using freedom and constraint topologies (FACT). *Precision Engineering*, *35*(4), 638–649. https://doi.org/10.1016/j.precisioneng.2011.04.006

Howald, L., Rudin, H., & Güntherodt, H. J. (1992). Piezoelectric inertial stepping motor with spherical rotor. *Review of Scientific Instruments*, *63*(8), 3909–3912. https://doi.org/10.1063/1.1143290

Koski, K. (2008). Focus Mechanism for Kepler Mission. In E. A. Boesiger (Ed.).

Lu, X., & Hanagud, S. V. (2004). Modeling for Self-Heating and Dissipation in Piezoelectric Ceramics. *IEEE transactions on ultrasonics, ferroelectrics, and frequency control*, *51*(12), 1582–1592.

Meijaard, J. P., Brouwer, D. M., & Jonker, J. B. (2010). Analytical and experimental investigation of a parallel leaf spring guidance. *Multibody System Dynamics*, *23*(1), 77–79. https://doi.org/10.1007/s11044-009-9172-4

Meijaard, J. P., Papadopoulos, J. M., Ruina, A., & Schwab, A. L. (2007). Linearized dynamics equations for the balance and steer of a bicycle: A benchmark and review. *Proceedings of the Royal Society A: Mathematical, Physical and Engineering Sciences*, *463*(2084), 1955–1982. https://doi.org/10.1098/rspa.2007.1857

Morançais, D., Mazuray, L., & Barthès, J.-C. (2006). ALADIN, the first wind lidar in space: development status. *International Conference on Space Optics — ICSO 2006*, *10567*(June 2006), 57. https://doi.org/10.1117/12.2308091

Morishima, T., Van Ostayen, R., Van Eijk, J., & Schmidt, R. H. (2015). Thermal displacement error compensation in temperature domain. *Precision Engineering*, *42*, 66–72. https://doi.org/10.1016/j.precisioneng.2015.03.012

Naves, M., Nijenhuis, M., Hakvoort, W. B., & Brouwer, D. M. (2020). Flexure-based 60 degrees stroke actuator suspension for a high torque iron core motor. *Precision Engineering*, *63*, 105–114. https://doi.org/10.1016/j.precisioneng.2020.02.001

Pepper, S. (2018). *Design of a Primary Mirror Fine Positioning Mechanism for a Deployable Space Telescope.*

Porchez, T., Barillot, F., & Belly, C. (2016). Nanometric Linear Piezo-Actuator with Integrated Strain Gages for High Stability Positioning. *International Conference on New Actuators*, (13-15 June). https://www.cedrat-technologies.com/fileadmin/user_upload/CTEC/Publications/Publications/2016/Nanometric_linear_piezo_actuator_with_integrated_strain_gages_for_hifh_stability_positioning.pdf

Smith, S., & Chetwynd, D. (1994). *Foundations of Ultraprecision Mechanism Design.* (2nd). Gordon; Breach Science Publishers S.A.

Stewart, D. (1965). A Platform with Six Degrees of Freedom. *Proceedings of the Institution of Mechanical Engineers*, *180*(1), 371–386. https://doi.org/10.1243/pime{_}proc{_}1965{_}180{_}029{_}02

TEAM, L. (2019). *LUVOIR Final Report* (tech. rep.). NASA.

Urgoiti, E., Ramirez, A., & Coste, P. (2005). Gaia M2M Positioning Mechanism. *roceedings of the 11th European Space Mechanisms and Tribology Symposium, ESMATS 2005.*

van Soest, A. J., Schwab, A. L., Bobbert, M. F., & van Ingen Schenau, G. J. (1992). SPACAR: A software subroutine package for simulation of the behavior of biomechanical systems. *Journal of Biomechanics*, *25*(10), 1219–1226. https://doi.org/10.1016/0021-9290(92)90078-F

Warden, R. M. (2006). Cryogenic Nano-Actuator for JWST. *38th Aerospace Mechanisms Symposium*. http://esmats.eu/amspapers/pastpapers/pdfs/2006/warden.pdf

Wees, T. v. (2019). *Thermal Modelling & Analysis of the Deployable Space Telescope*.

Wijker, J. (2008). *Spacecraft Structures*. Springer. https://doi.org/10.1007/978-3-540-75553-1

Yoder, P. R., & Vukobratovich, D. (2015). *Opto-mechanical systems design Volume 2: Design and analysis of large mirrors and structures* (Fourth edi). CRC Press.

Zahedi, F. (1986). The Analytic Hierarchy Process — A Survey of the Method and its Applications. *Interfaces*, *16*(4). http://www.jstor.org/stable/25060854.

4

VERIFICATION AND VALIDATION OF COMPUTATIONAL MODELS IN ACTIVE OPTICS MECHANISMS

Just by looking through your eyes
He could see the future penetrating right in through your mind
See the truth and see your lies
But for all his power couldn't foresee his own demise

Iron Maiden, The Clairvoyant

Development of active optics mechanisms is supported by the use of computational models of the physical phenomena which affect their behaviour. If models are to be reliably used in design, there must be a robust validation and verification approach to confirm their predictive performance. In this chapter, verification and validation of the dynamic and thermoelastic models presented in previous chapters will be performed.

4.1. OVERVIEW OF MODEL VERIFICATION AND VALIDATION

In order to build confidence that the models used to support the development process described in Chapter 4 are accurate, proper verification and validation (V& V) are required. Here model verification is understood to be the process of checking that the model performs as intended. Model validation is the process of checking if the conceptual basis of the model predicts the behaviour of the system studied. Computational models may be verified and validated following methodologies described in (**Kleijnen, 1995**). This is a general classification of V&V methods in computational models, but not all of them are relevant to the application described here. As a summary, the methods proposed for verification are good programming practice, verification of intermediate outputs, and animation of the model. The methods used for validation are the comparison to real world data, and sensitivity analysis. In this chapter, the efforts to apply these V&V strategies to the models described in **Chapter 4** will be described.

Good programming practice is cited as a verification tool because it enables several other verification activities. The code that generates the computational models should be modular, clear, and documented. This makes it possible to maintain, update and verify code with the smallest amount of work. Modularity in code refers to splitting the computer program in different, exchangeable modules which each perform one function that can be independently verified and validated.

As a summary, the models address four main problems: Static load, linear buckling loads, dynamic response, and thermoelastic behaviour. In this chapter the focus will be the latter two problems because they can be experimentally validated. Static loading and buckling need to be validated separately, but if the model can predict dynamic and thermoelastic behaviour, it is likely those other problems could be modelled too. Dynamic characterisation is performed by modal analysis, which intends to find the eigenfrequencies and eigenmodes of the system. The purpose of the thermoelastic model is to find the pose of the mirror given a temperature field on the system. The functions in the thermoelastic model and their interactions are shown in **Figure 4.1**. The dynamic model is only comprised of runManager, datBuilder, and SPACAR.

The use of these functions are:

- runManager defines the model parameters. It declares the geometry, material properties and assigns a temperature field to the different parts.
- datBuilder takes the geometry, properties and element declarations from runManager and generates the .dat file which constitutes the input to the SPACAR solver.
- SPACAR is the extended finite element method solver, which outputs the displacement of the nodes defined in the input file and the element deformations.
- poseanalysis is a function which extracts the pose of the end effector from the SPACAR output.
- data_calibration is used with experimental data. It structures measured temperatures so that they can be accessed by Thermloop to analyse a test case.

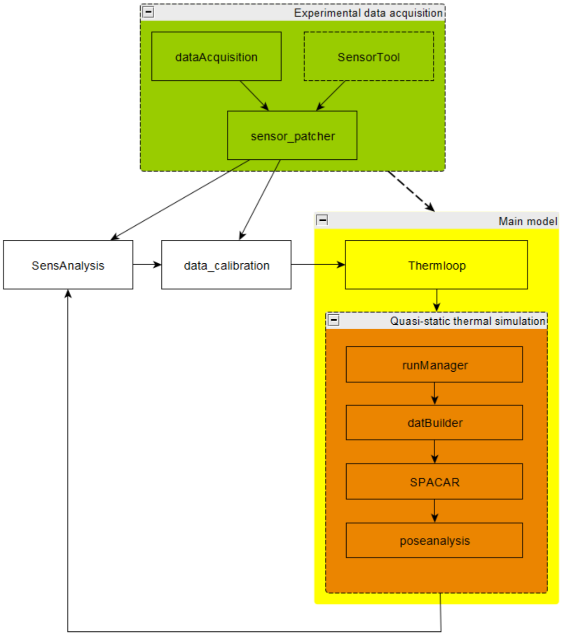

Figure 4.1: Breakdown of component functions of the thermoelastic computer model with modules which incorporate experimental data.

- Thermloop interpolates time-dependent temperature data and calls runManager for a quasi-static thermoelastic solution in each point in time. Thermloop can also select different sets of degrees of freedom of the model so that they can be independently verified.

- SensAnalysis runs an instance of Thermloop for different sensitivity parameters. Therefore it is possible to find sensitivities of the model to different uncertain characteristics.

These functions can be independently tested for intermediate outputs of the model. The details as to how these functions can be accepted will be discussed in coming sections. As for validation, a test item was designed in order to produce real time data. An additional verification activity was carrying out independent modelling using Ansys Workbench. Workbench allows lumped mass thermal analysis and structural finite element method. Ansys was expected to better predict the eigenfrequencies and eigenmodes of the structure, because of its ability to model flexible bodies of any shape. The overview of activities is shown in **Figure** 4.2.

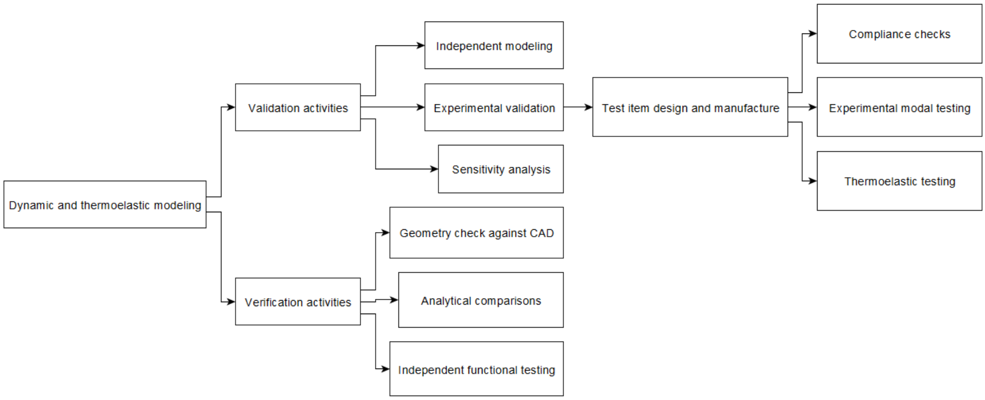

Figure 4.2: Overview of model V&V activities for computational model performance.

4.2. PROTOTYPING

Generating experimental data which can be used for validation purposes requires a test item. Manufacturing the complete PMAO system, including mirror and piezoactuators, was unfeasible. However, a flexured frame with a dummy mirror and dummy actuators could be made. This does not allow to test the final performance as a mechanism, but it can build confidence in the models used to design it. The test item designed for this purpose includes the passive elements of the PMAO and a mass to represent the mass of the mirror.

In order to manufacture a test item which could validate the models, the first step was making a computer model in commercial Computer Assisted Design (CAD) software Catia V5. This also required defining the joining methods between flexural parts, as the setup could not be practically manufactured from a single metallic piece. Joints were realised either with pins or bolts. The other major decision to be made at the prototype stage was the structure of the fixed frame, which in the original SPACAR model is treated as a boundary condition. The requirements for dynamic characterization tests require that the fixed frame provide a rigid boundary condition, which is difficult to implement in practice. In contradiction to this requirement, there was a need for an open structure in which many temperature sensors could be attached. The final design favoured the latter need, with an open structure for the fixed frame which is easily accessible. This also necessitated changes in the geometry as defined in the SPACAR model.

After the first CAD design of the test item was made, its parts were 3D-printed to check for manufacturability. After compiling the lessons that could be learned from such rapid prototyping, a final CAD design was produced. From this, the technical drawings were made and sent to manufacturing. Though the selected material of the trade-off was Ti6Al4V, this material caused very high costs due to both the market price of the material and the required tooling for working it. Instead, the second material choice, Al7075, was selected for all parts except the dummy mass which represents the mirror. This dummy was made with stainless steel 403 and has a mass of 6 kg. The reasons for using stainlesss steel was that the target mass could be achieved with a smaller item, coefficient of thermal expansion is

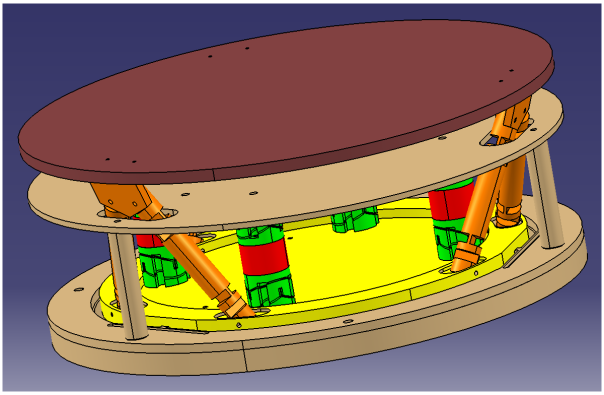

Figure 4.3: CAD model of the test item. Fixed frame in light brown, moving frame in yellow, actuator dummies in red, flexure joints in green, flexured bipods in orange and dummy mass in dark brown.

smaller, and stiffness is higher than the rest of the item. The computational models were adjusted to check their predictive capability with this material. The final CAD design is shown in **Figure** 4.3.

4.3. EXPERIMENTAL MODAL ANALYSIS

Modal analysis is one of the most common methods of characterisation of structures and its full description is out of the scope of this work. The basics of modal decomposition for the analysis of vibration can be studied in vibration theory textbooks (**Beards,** 1995**; He and Fu,** 2001). The specific implementation followed the guidelines of the Siemens Simcenter documentation because Simcenter Testlab was used to collect the data (**Siemens,** 2020).

The modal analysis was performed with a modal hammer. The test setup is shown in **Figure** 4.4 Data was collected via nine tri-axial accelerometers placed at the different structures of the mechanism frame. Three of them were placed at the dummy mass, three in the top part of the fixed frame, and three in the moving frame. Data samples were collected by hitting the test item with the hammer ten times to get a representative average response. The frequency response functions (FRF) of the twenty-seven channels were collected. The frequency band that was studied was between 20 and 650 Hz. The reason for this choice is that coherence figures at low frequencies (20 to 50 Hz) were very low, and higher frequencies were not of interest since models were expected to be unable to predict them regardless. The most likely explanation for bad coherence at these frequencies is the fact that the reference frequency response of the hammer is not flat at low frequencies, so the FRF is difficult to define.

The dataset was processed in Simcenter Teslab in order to extract the modal shapes found in each test. This step is needed because the modes predicted had mostly either components in horizontal or in vertical directions. Modes that are primarily horizontal do not appear clearly when the system is excited vertically and viceversa. Modes found in different modal hammer strikes were then combined to find the final experimental modal shapes.

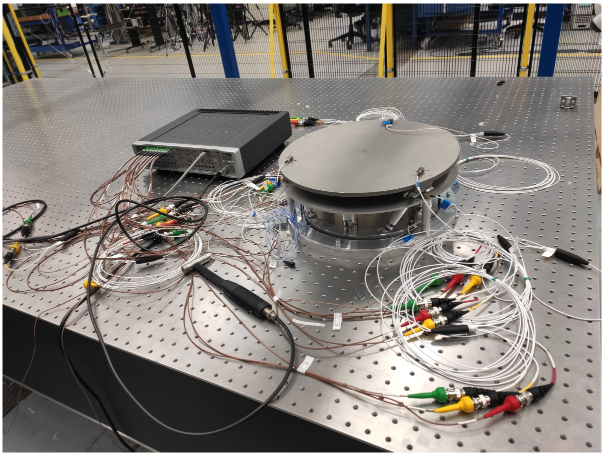

Figure 4.4: Test setup for experimental modal analysis, showing the data acquisition system (left), the modal hammer (front centre) and the test item (right).

This process is called modal synthesis. The first six eigenfrequencies were found in SPACAR and in the modal analysis. SPACAR is unable to predict the first six eigenfrequencies as shown in **Table** 4.1, though the first experimental mode shape is predicted. This was attributed to the difficulty in representing the real boundary conditions in SPACAR, as a result of the choice of keeping an open structure of the fixed frame, which reduced its stiffness. In order to support this explanation, an additional FEM model was made in Ansys.

The Ansys FEM model was created by meshing the CAD files and assigning the respective materials. This model allows implementation of the real boundary conditions found in the test, which was in practice not possible in SPACAR. The Ansys model offers good prediction of the mode shapes at low frequency. All six first modes predicted in Ansys are well approximated in the experimental data, but they appear at considerably higher eigenfrequency as shown in **Table** 4.1. Both Ansys and SPACAR predict a local twisting mode of the actuator pillars, which was difficult to excite experimentally due to lack of access, and appears at 512 Hz in SPACAR and 650 Hz in Ansys. The pillar twisting mode repeats four times for the four pillars at the same frequency. Other than this, SPACAR overestimates the stiffness of the mechanism and many modes include deformation of plates which could not be implemented in SPACAR. In order to discard that the limited predictive power of SPACAR in modal characteristics were resulting of errors in the program, the boundary conditions in Ansys were modified to reflect the calculations in SPACAR, and check if they are still useful to compare with requirements. Indeed, introducing equivalent boundary conditions between Ansys and SPACAR, the first eigenfrequencies predicted are 168 Hz and 173 Hz respectively with similar mode shapes, but SPACAR continues to overestimate the stiffness of the setup in piston direction.

Interestingly, there is a multiplicative bias between the Ansys prediction of each eigenfrequency ω_{Ansys} and the experimental result, ω_{exp}. The experimental result is in the order of 25% lower than the Ansys prediction. It is likely that Ansys systematically overestimates

Table 4.1: Comparison of modal analysis results between experiments and different models.

Mode number	Experimental result [Hz]	SPACAR prediction [Hz]	Ansys prediction [Hz]	$\frac{\omega_{exp}}{\omega_{Ansys}}$	Experiment description	Accurate shape prediction?
1	27.4	172.1	39.8	0.688	Tilting motion	Ansys/SPACAR
2	29.1	172.3	40.5	0.718	Tilting motion	Ansys
3	40.6	268.3	52.8	0.770	Piston motion	Ansys
4	99.3	512.2	125	0.794	Combined tip-tilt motion	Ansys
5	105.8	512.2	147.3	0.718	Tilting motion	Ansys
6	127.7	512.2	171.07	0.746	Moving frame displacement	Ansys

the stiffness of the system.

4.4. THERMOELASTIC CHARACTERIZATION

Whilst modal analysis is a well-known technique to characterise the dynamic behaviour of a structure, there is no such standard for thermoelastic behaviour. Research in precision mechanisms includes a variety of approaches for thermoelastic characterisation, in particular for reduction and compensation strategies, both deterministic and statistical (**Vanherck et al.,** 1997**; Weck et al.,** 1995). Reduction in this context is the use of thermal control to reduce thermally induced errors, compensation is athermalization of a machine tool. The thermal behaviour of the end effector of mechanisms is difficult to evaluate deterministically in general. In the context of machining centres, models based on regression or neural networks outperform physics based modeling in predicting the spindle's position error (**Hatamura et al.,** 1993**; Li et al.,** 2015). However, efforts in physics-based modelling of thermoelastic problems have been made in different contexts. Morishima investigated the thermoelastic behaviour of a plate under moving point thermal loading for the purpose of thermoelastic compensation (**Morishima et al.,** 2015). Morishima uses thermal modal analysis to find optimal control strategies for the end effector, and validates the model with both analytical solutions and experimental results (**Morishima,** 2016). Saathof used similar techniques to thermally control an active mirror (**Saathof et al.,** 2016) for photolithography applications. Published work on thermoelastic modelling of complex structures has focused on optimal arrays of sensors to characterise the position of the end effector (**Evers et al.,** 2019**; Evers et al.,** 2020**; Herzog and Riedel,** 2015**; Koevoets et al.,** 2007).

An experiment has been proposed to address the validation of the thermoelastic model. The test item is the prototype as described in **section** 4.2. Since the conditions in orbit cannot be easily reproduced on the ground, the test item will be heated with an array of heaters distributed over the prototype. This shall generate an uneven temperature distribution which can be detected with a temperature sensor array. The thermoelastic displacement can be measured at the end effector as a measure of what the displacement of a mirror placed on this mechanism would be. Linear sensors will be used to measure the pose of the dummy mirror. The functional diagram for this setup is shown in **Figure** 4.5 and a simplified schematic is shown in **Figure** 4.6.

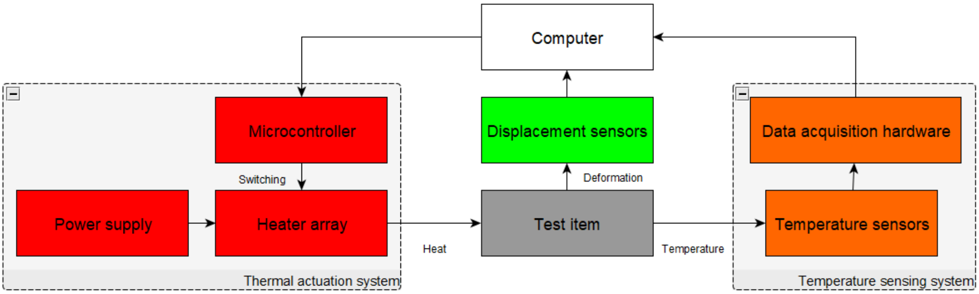

Figure 4.5: Block diagram of thermoelastic test setup.

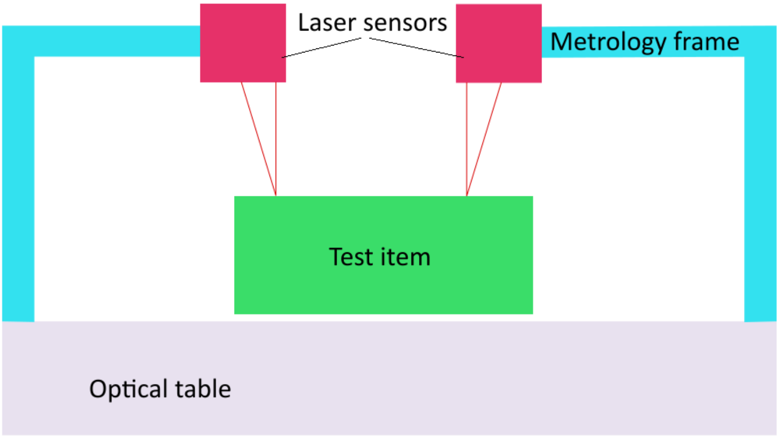

Figure 4.6: Simplified schematic of the displacement measurement concept.

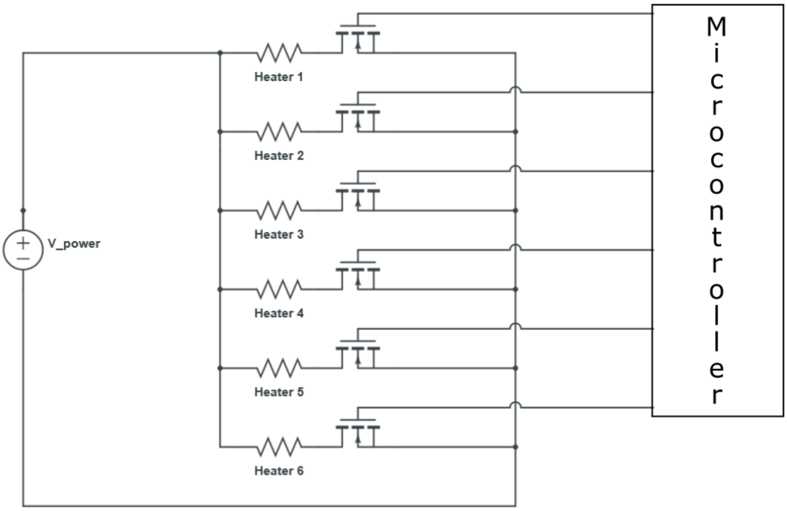

Figure 4.7: Electrical diagram of the heating system.

4.4.1. HEATER SYSTEM

The heaters are silicon flexible heaters with a rated power of 1.25 W when powered at 12 V_{DC} and manufactured by RS Components [1]. Safety rules mandate that they be operated under 30 V_{DC}, so the maximum operating voltage of the experiment was set at 25 V_{DC}. The heaters are connected to a power supply that delivers the control voltage. The circuit is closed via N-channel MOSFETs [2] which separate the heaters from the electrical ground. The gate of the MOSFETS is connected to the digital output pins of an Arduino MEGA 2560 R3 [3] which can be programmed to be HIGH or LOW. Current flows through the heaters when the pin is HIGH, whilst the circuit is effectively open when the pin is LOW. The heater control circuit is shown in **Figure** 4.7.

The parts where the different heaters were attached are shown in **Figure** 4.8. The heaters were glued on different elements setup according to the following scheme:

- Centre of the moving frame plate.
- Dummy actuator stack, placed on positive X axis.
- Dummy actuator stack, placed on negative Y axis.
- Dummy actuator stack, placed on positive Y axis.
- Flexured strut AA1.
- Flexured strut CC1.

---

[1] Data available at: https://uk.rs-online.com/web/p/heater-pads/0245499
[2] Data available at: https://nl.rs-online.com/web/p/mosfets/6714871
[3] Data available at: https://store.arduino.cc/products/arduino-mega-2560-rev3

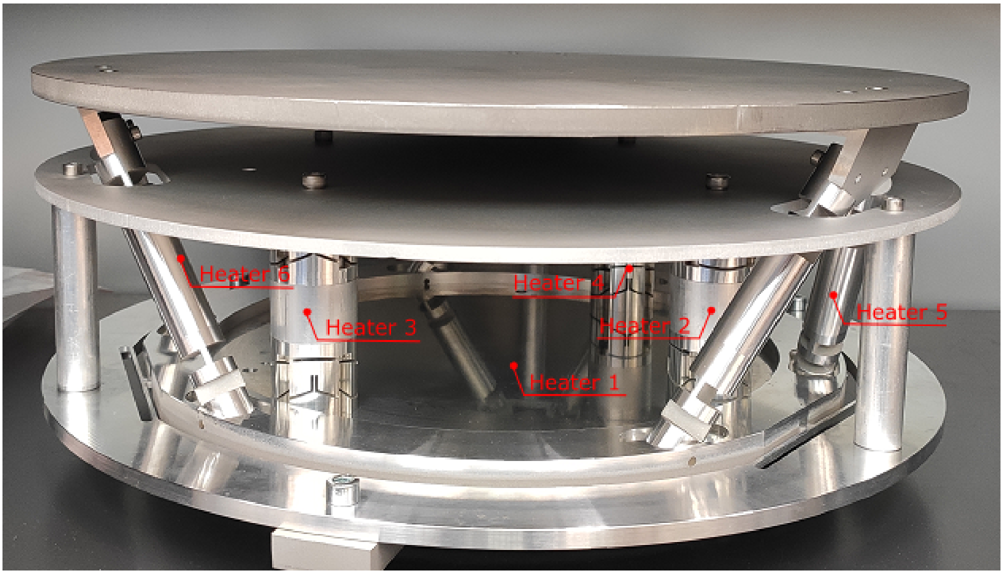

Figure 4.8: Picture indicating where the flexible heaters were attached to the setup.

This scheme was chosen as a non-symmetric arrangement, so that the thermoelastic behaviour cannot be athermalised. This was expected to yield a more generic thermoelastic behaviour. A symmetric arrangement of the available heaters would have yielded, except for workmanship variability, a symmetric temperature field. In that case, there would be a displacement along the *Z-axis*, but no tip-tilt rotations. The heaters resulted to be excessively thick for the curvature needed to adapt to the setup, which makes the interface unreliable. This was an accepted limitation because as long as the measurement of temperature is accurate, the arrangement and workmanship of the heaters should have no influence on the ability of the model to predict displacements. If the model is accurate, given a temperature field, the displacements will be accurately predicted.

4.4.2. TEMPERATURE MEASUREMENT SYSTEM

To measure the temperature, an array of 43 Negative Temperature Coefficient thermistors (NTCs) was built, although one of them was eliminated due to a malfunction. NTCs are electrical resistances which show a strong dependence with temperature. The NTCs are connected in a voltage divider configuration, with a resistance to ground of 12 kΩ and connected at a direct current voltage of 10 V. The output is connected to a National Instruments Analog-to-Digital converter (ADC) which in turn connects to a computer. ADCs used had input voltages between -10 and 10 volts and 16 bit conversion. The voltage divide circuit is shown in **Figure** 4.9. The main challenge with NTCs for thermometry is the non-linear nature of the resitance's dependency with temperature (**Rudtsch and Von Rohden,** 2015). One approach used to calculate the resistance-temperature relation the β curve

$$R_T = R_0 e^{\beta\left(\frac{1}{T_{Measured}} - \frac{1}{T_{ref}}\right)}. \tag{4.1}$$

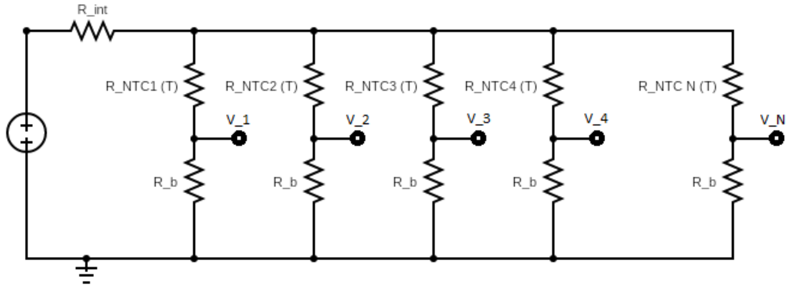

Figure 4.9: Electrical circuit for multi-channel temperature sensing using NTCs.

With R_0 being the resistance at a reference temperature T_{ref} and $T_{Measured}$ is the temperature of the NTC. For the NTCs used in this experiment, the reference resistance is 10 kΩ at 25^oC [4]. The other main approach is the use of logarithmic power expansions of the form

$$\frac{1}{T_{Measured}} = \Sigma_{i=0}^{n} C_i \left[\ln\left(\frac{R_T}{R_S}\right)\right]^i . \tag{4.2}$$

Where R_S is an arbitrary resistor, which does should not be confused with the NTC resistor value at a given temperature. If $C_2 = 0$ and $n = 3$, this expression is called the Steinhart-Hart equation, which requires one less calibration point than the four-term expansion, but is less accurate (**Rudtsch and Von Rohden,** 2015). The order of this expansion was chosen as $n = 3$. The constants of the series expansion were determined by immersing the NTCs in three phase-changing substances with well defined phase transition temperatures. The substances used were water-ice at 273.15 K, boiling acetone at 329.2 K, and boiling ethanol at 351.52 K, all at ambient pressure. A fourth calibration point was chosen as the room temperature measured with an independent thermal camera. Using room temperature as additional calibration point is known to be less accurate than having a phase transition as fourth calibration point, but it improved the spread of temperature measurements in the operating range.

Given the output voltage as measured by the ADC, the resistance value at a given time can be calculated as

$$R_i(T) = R_{Bi}\left(\frac{V_B}{V_{oi}(T)} - 1\right). \tag{4.3}$$

R_i is the resistor value of the i-th NTC, V_B is the voltage set by the power supply and R_{Bi} the resistance between the output and the ground. Here R_{Bi} varies between branches because commercial resistors can deviate from their nominal value by as much as 5%, but combining equations 4.3 and 4.2, it can be shown that the final temperature value does not depend on the different R_{Bi} once the constants C_i are chosen with known calibration points.

The NTCs were integrated on the surface of the test item using commercially available thermally conductive paste between the NTC and the surface, and secured with kapton

---

[4] Data available: https://www.te.com/usa-en/product-GA10K3A1IA.html

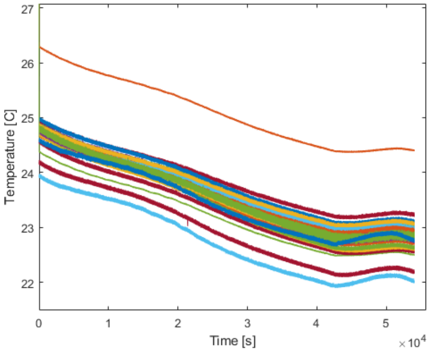

Figure 4.10: Temperature variation of the setup with no loads over 14 hours, as measured by the array of 42 functioning NTCs.

Table 4.2: Characteristics of ILD 1900-10 laser triangulation sensors.

Characteristics	Value
Nominal range	10 mm
Minimum stand-off	24 mm
Linearity	0.2 μm
Repeatability	<0.4 μm
Temperature stability	0.0125 % /^{o}C
Operational temperature	0 to 50$^o C$

tape. The test environment is an air conditioned room, with some level of natural temperature variation over time. This was tested over 14 hours, with the stability of the setup being better than 0.16 K/hour. The test was performed three times, the most unstable of which is shown in **Figure** 4.10.

4.4.3. DISPLACEMENT SENSORS

Displacement at the end effector is measured with a couple of laser triangulation sensors. Only two sensors were available at any one time, which limits the amount of DOFs which can be measured at once to two. These were chosen to be piston displacement, and either tip or tilt, as those are controllable degrees of freedom in the mechanism concept. These can be characterised with the lasers pointed down towards the test item, parallel to its *Z-axis*. In an initial embodiment of the experiment, Micro-Epsilon optoNCDT ILD 2200-2 sensors were used, but they were replaced by ILD 1900-10 sensors [5] for the final iteration. The main sensor characteristics are listed in **Table** 4.2. These characteristics were accepted based on a rough order of magnitude estimate based on expected displacements of 40 μm.

In the initial embodiment of the experiment, the sensors were clamped to an aluminum T-slotted frame which was in turn bolted to the same optical table as the test item. However,

---

[5] Data available at: https://www.micro-epsilon.com/download/manuals/man–optoNCDT-1900–en.pdf

thermal expansion of the frame was overconstrained, which made it difficult to model and compensate for the deformation of this frame in the analysis of the data (**Hale,** 1999). In the final setup, the sensors were bolted to magnetic kinematic bases, which were in turn bolted to independent L-shaped beams so that the only significant thermal expansion is in Z direction. A flat mirror was used to align the laser so that it was perpendicular to the surface of the test item with a cosine error θ_{align} of less than 0.026 radians. The alignment error affects the sensor readout $\Delta Z_{measured}$ for a real displacement ΔZ as

$$\frac{\Delta Z}{\Delta Z_{measured}} = \cos\theta_{align} \geq 0.99969. \tag{4.4}$$

The magnetic kinematic bases are reported by the manufacturer to have a repeatability better than 30.96 μrad [6], which yields a negligible cosine error. Both the first iteration of the experiment and the complete testing setup are shown side by side on **Figure** 4.11. Note the original frame has indeterminate thermal displacement, whilst the final version only requires piston direction compensation. Thermal bending of the frame could happen, but it yields a negligible cosine error. The magnetic bases allow easy swapping of the sensors between four different locations, so that piston, tip and tilt can be detected, albeit in different tests. The main differences between the two test setups used are:

- Environment changed from aircraft structures lab to cleanroom.
- Laser triangulation sensors ILD2200-2 changed to ILD1900-10.
- Overconstrained frame substituted for L-frames.
- Active optical table changed for passive optical table.
- Sensor analog readout converted with 16-bit ADC changed for digital operation.
- Language of data acquisition software changed from LabView to Matlab.
- Temperature sensors recalibrated.
- ADC cards changed form NI6211 to NI PCI 6229.

All data used in the elaboration of this chapter corresponds to the second iteration of this experiment.

4.4.4. TEST PROTOCOL

- Setup is initially in thermal equilibrium with its environment.
- Initialization of temperature data acquisition, controlled by a code in MATLAB.
- Initialization of displacement data acquisition, controlled by proprietary Micro-Epsilon software sensorTool.exe.
- Initialization of heating script, which waits 300s before turning the heaters on, controlled by Arduino script.

---

[6] Data available at: https://www.thorlabs.com/newgrouppage9.cfm?objectgroup_id=15469453

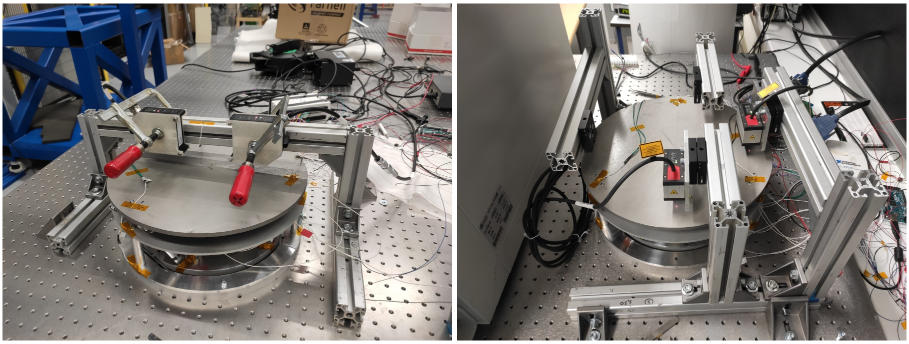

Figure 4.11: First iteration of thermoelastic test setup (left) and final iteration showing magnetic kinematic bases and separate beams.

- Test has a standard heating duration of three hours.
- After the standard duration has elapsed, heaters are switched off automatically.
- Temperature data acquisition stops after five hours. Data is stored in a MAT file.
- Displacement data acquisition is stopped manually by the operator. Data is stored in a CSV file.
- Displacement and temperature data are combined in a second MAT file by a MATLAB script.

In order to begin the test protocol, at least 5 hours are left between tests so that the system can reach the environmental temperature. Since data acquisition of temperature and displacement are not acquired by the same software, the first samples of both datasets have different timestamps, and samples are acquired at different frequencies. The MATLAB script mentioned in the last step of the protocol, which combines the two datasets, synchronises the initial samples. Records of thermistors and laser triangulation sensors during a test are shown in **Figure** 4.12 as an example of the output of this process. In these graphs, the test can be divided in three parts: Initial waiting time at room temperature, heating of the test item, and cooldown.

4.5. COMBINED MODEL AND EXPERIMENT VERIFICATION AND VALIDATION

A comparison between model predictions and experimental measurements has been proposed as a good validation tool for the model. If this compliance is not found, there needs to be a procedure to diagnose whether the conditions of the test have been faithfully translated to simulation conditions. The criterion for compliance is an absolute error between sensor readout and model predictions in the order of 1 μm, which is considered reasonable with an expected sensor accuracy of 0.4 μm. The verification process necessary to build confidence in this link between experiments and models comprises both verifying that the test conditions are well known and the models are correctly set up.

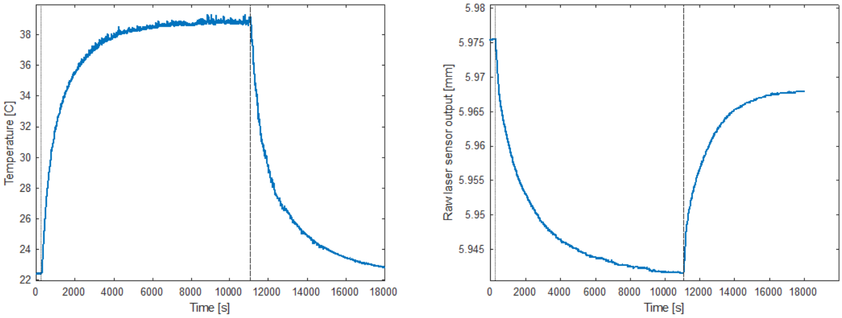

Figure 4.12: Typical temperature records of one of the thermistors (left) and typical displacement sensor record (right) during a standard test. Vertical lines represent the moments when heaters are turned on (left side of the graph) and off (right side of the graph).

Four main branches can be responsible for non-compliance between models and experiments: model parameters, experiment parameters, wrong interface between different data streams, and wrong interpretation of results. In this subsection, the objective is to systematically discuss and present mitigation measures for different sources of error. However, not all possible errors could be rigorously eliminated. These are included for completeness, but are acknowledged as potential weaknesses of the modelling and testing approach. A fault detection tree including all the errors that were examined is shown in **Figure 4.13**.

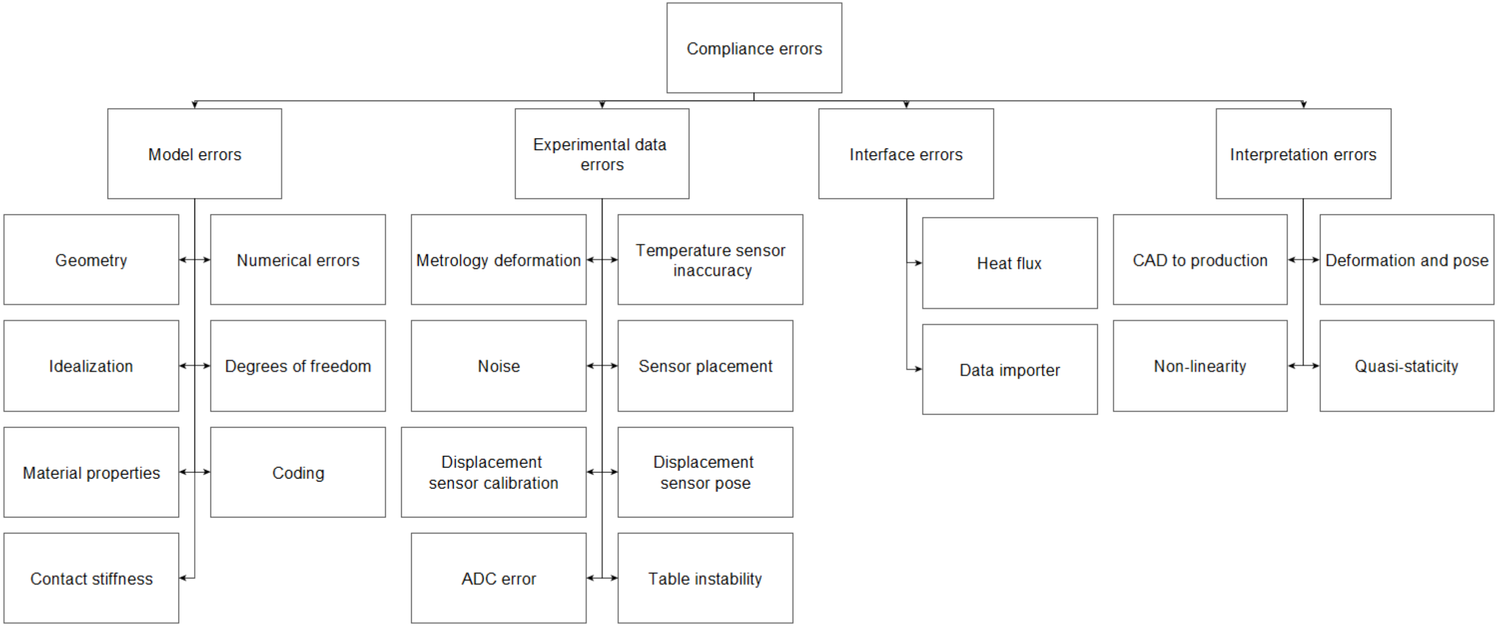

Figure 4.13: Combined fault detection tree for the experiment and model.

4.5.1. ERRORS IN MODEL

GEOMETRIC REPRESENTATION

Lack of direct geometry import tools or a centralised repository of geometric characteristics makes it difficult to translate design parameters across the different models of the mechanical design. From the original design made by Pepper (**Pepper, 2018**), some dimensions needed to be changed and some features were added to the production drawings. These needed to be translated manually to the numerical model so that there is a consistent set of geometric constraints. Spavisual is a useful tool to visualise geometry, but it is not able to differentiate small details such as length of flexures or element thickness. In addition, some geometric relations are defined mathematically in the model from different parameters, and do not translate directly to CAD. Several key points of the geometry were extracted from the CAD and SPACAR representations and compared to ensure that this process yields a close enough (error less than 0.001 mm) representation of the geometry produced in the end.

IDEALIZATION

Here idealization refers to how the behaviour of the elements of the mechanism is translated to a mathematical expression. As detailed in **Chapter 3**, the constitutive equation that translates the temperature field to an equivalent thermal force P in a beam is

$$P = \alpha E A \Delta T. \tag{4.5}$$

With α being the coefficient of thermal expansion, E being the Young's modulus, and ΔT being the temperature increase of the beam. One of the fundamental assumptions of this model is that all elements can be approximated with beams that follow this relation. This approximation was considered adequate if the boundary conditions on the elements which are not beam-like allow free thermal expansion. In the case of this mechanism, intermediate bodies which are not beams, such as the moving frame or the mirror dummy, are constrained with elements with low stiffness in the radial expansion direction. This should make it possible to approximate the behaviour of plate-like elements with one dimensional beams, but it remains a difficult assumption to validate.

NUMERICAL ERRORS

The details of the FEM solver which calculates the displacements at the nodes are outside of the scope of this work. However, FEM solvers, including SPACAR, include warnings in cases of high probability of numerical instability of the solution. This numerical instability is caused by the condition number of the stiffness matrix, which is internally calculated, and is typically a sparse matrix. The condition number and numerical stability can sometimes be improved with actions such as changing the rows and columns so that more optimal pivots can be found when solving the system. The condition number is also sensitive to scaling of the system inputs. Problems with numerical stability have been found in the solution of the thermoelastic problem with some temperature datasets collected in the experiment. These problems typically disappear when multiplying the thermal stresses by an arbitrary multiplier which changes the scale of the problem and allows optimal solution of the system. The solution can then be corrected by dividing the output by the same multiplier. If the model output is linear with the loads, this yields the same result. One of the verification activities was therefore to run the model with linearly scaled inputs, and checking that outputs were also linearly scaled. Since this was true, numerical instability was not considered a problem.

ALLOWED DEGREES OF FREEDOM

SPACAR requires that the user defines the allowed deformation degrees of freedom of each element. This may give rise to errors when assigning the degrees of freedom allowed to the system. The main way to verify that this assignment was done correctly was animating the model under arbitrary and well-defined loads, so the deformations can be visualised and checked against expectations. This procedure was used to verify that the degrees of freedom were correct.

MATERIAL PROPERTIES

Most of the elements in the experimental setup are manufactured with aluminum alloys. The exceptions to this are the stainless steel dummy mirrors and the bolts which connect parts to one another. The properties which are relevant in this model are the coefficient of thermal expansion, the Young's modulus and the bulk modulus. There is a spread on the values of these properties from different sources, with coefficients of thermal expansion of aluminum alloys reported between 21 and 24 $\mu\epsilon/\mathrm{K}$ (**Cardarelli, 2018**). In order to cover the risk of misassigning the material properties to the model, these three material properties were added to the sensitivity analysis, but only the coefficient of thermal expansion is expected to make a significant difference. The reason for this is that the Young's modulus has no influence in free thermal expansion, and the bulk modulus affects shear primarily, which is expected to be minor.

CONTACT STIFFNESS

The SPACAR model cannot model contact stiffness between different parts. The underlying assumption is that the connection between elements behaves the same as any linear elastic material. It was not feasible to manufacture the test item as a monolithic structure, so there are bolted and pinned interfaces present. Estimating contact stiffness is a difficult and uncertain process, and is likely not implementable in SPACAR. In addition, bolted interfaces are not meant to carry any loads in this design, as the load is alleviated by the flexured joints. Therefore, no effort was made in modelling contact stiffness. More research into the specific behaviour of these joints would be needed in order to have a usable model for contact stiffness in flexured mechanisms.

CODING

Most coding errors result in a piece of code not being executable. These are syntax errors and wrong variable definitions which can be immediately caught. Individual functions were checked with intermediate outputs before acceptance. This process could only be done manually and there is no practical way to completely ensure that no part of the code had coding errors. Documentation included with the code details the complete set of versions which are compatible for each iteration of the integrated model. The documentation also explains in detail all variable definitions, and the functionality of each section of each function. Typical errors are also shown via warning messages.

4.5.2. ERRORS IN EXPERIMENTAL RESULTS

METROLOGY FRAME DEFORMATION

A well known challenge in precision measurement is the separation of the metrology structural loop from the structure which is being observed (**Hale, 1999**). There may be a physical separation, or a separation based on data treatment. In this case, the approach is mixed, with both the test item and frame holding the sensors being bolted to the same optical table. In this case, it is not possible to isolate the heat leaks from the test item to the frame. The material of the frame is aluminum, which has the same coefficient of thermal expansion as the material of the test item. Therefore, thermal expansion of the frame can be significant.

The approach is to compensate for this thermal expansion by tracking the temperature of the frame, and compensate the output of the sensor using a model of thermal expansion of the frame. An overconstrained frame introduces uncertainty in the modeling of its thermal expansion, which is why independent frames for the two laser sensors are an improvement of the final experimental setup over the initial iteration. Thermal expansion of the frame was compensated for each sensor as:

$$\Delta Z_{corr} = \Delta Z_{sensor} - \alpha_{frame} L_{frame} \Delta T_{frame}. \tag{4.6}$$

With ΔZ being the displacement at the point of sensing, α is the coefficient of thermal expansion, ΔT is the temperature variation and L is the height from the table to the laser sensor. This correction is likely to overestimate the effect of thermal expansion of the frame because the temperature of the frame is not homogeneous and likely has a maximum close to the sensing point.

TEMPERATURE SENSOR INACCURACY

The non-linearity of the NTC temperature sensors makes it difficult to guarantee their reliability without a good temperature measurement standard to provide multiple calibration points. The calibration procedure described in **subsection 4.4.2** guarantees that given a voltage level, which in this work is set to 10 V, temperature is accurately determined at those points. However, temperature sensors are believed to drift over time (**Rudtsch and Von Rohden, 2015**), and there is a spread in the order of 2 K in the sensor reading at room temperature. This is one of the major problems with relating experimental results to the output of the model, and will be further examined by a sensitivity analysis in **section 4.6.4**.

SENSOR NOISE

Temperature sensor noise introduces uncertainty in the temperature measurements. Given that input temperatures to the thermoelastic model are differential temperatures between one measurement and another, the error in the differential temperature ΔT due to noise is

$$\Delta T(t) = T_{Measured}(t) - T_0 \pm 2e(t). \tag{4.7}$$

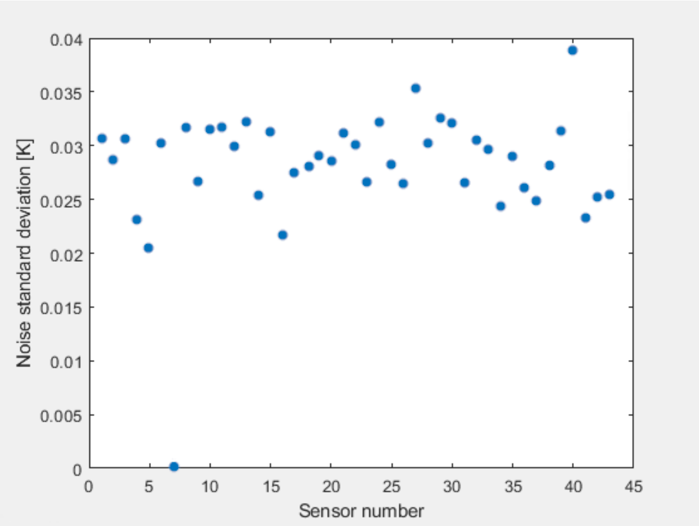

Figure 4.14: Standard deviation of differential temperature measurement noise for all the sensors.

Where $T_{Measured}$ is the temperature measured at time t and T_0 is the initial temperature measurement from which differential temperatures are computed. It is useful to quantify its standard deviation. A sample of 6 minutes at 30 samples per second was taken under the assumption that the real temperatures of the room do not change over that time span in order to characterise the random noise. From this sample, the standard deviation in the differential temperature measurement was calculated as

$$2\sigma_e = 2\sqrt{\frac{\sum_i (T_{Sample\,i} - \mu_T)}{N}} \tag{4.8}$$

Where σ_e is the standard deviation of the sensor noise, $T_{Sample\,i}$ are the sampled temperatures, μ_T the mean of the sample and N the number of samples. The value $2\sigma_e$ for each sensor is shown in **Figure** 4.14. The highest value recorded is 0.039 K on sensor number 40. Note the values for sensor number 7 is not valid due to sensor failure. Taking a 2σ confidence interval, a resolution of 0.5 K can be expected from this setup with a signal-to-noise ratio of 6.2.

SENSOR PLACEMENT

Due to lack of markings, the centre of the end effector needed to be found with drawing tools so that distances to it can be calculated and the sensor readings can be compared to the model. This introduces uncertainty as to what the exact position of the sensing points are relative to the end effector centre. Several measurements of the centre to the edge of the end effector were made and compared to the theoretical radius of the end effector, as a measure of what the uncertainty in the centre is. After six measurements, the centre was estimated to be off by less than 4 mm.

DISPLACEMENT SENSOR CALIBRATION

The laser triangulation sensors used were factory calibrated, and performing additional calibration was outside of the scope of this work. Basic checks of the sensors included moving a target closer and further from it and checking that output was consistent, and leaving it gathering data in an unchanging environment. Sensors have a peak-to-peak noise floor of 0.4 micrometers, as advertised by the manufacturer.

DISPLACEMENT SENSOR POSE

As explained in **subsection 4.4.3**, the relative pose of the displacement sensors induces a cosine error which can be easily reduced to less than 0.5% of the sensor output. This makes this potential source of error negligible compared to others.

ADC CONVERSION ERROR

The displacement sensors incorporate their own ADC and are used in fully digital mode. The performance of this sensor as a complete system has already been discussed. The temperature sensors are connected to National Instruments (NI) data acquisition cards NI PCI 6229 with 32 channels, and NI USB 6211 with an additional 16 channels. The dynamic range of both ADC units is (-10,10) V and their conversion is made with 16 bits, which means the minimum detectable voltage difference is 0.305 mV. The possible voltages of the voltage divider branches go from 0 to 10 V, though the limits of this range only occur if the resistance of the NTC tends to infinity or to 0 respectively. Given the non-linear behaviour of the resistance-temperature relation, it is interesting to characterise the resolution in the temperature domain. The practical range of temperatures found in operation is from 0 to 80 ^{o}C. Using equations 4.1 and 4.3 in the practical temperature range, the range of practical voltages can be found. With this information and the voltage resolution of the ADC, the temperature resolution can be plotted as a function of temperature in the relevant region. The temperature resolution is shown in **Figure 4.15**, which is smaller than the 2σ noise values for the entire range..

OPTICAL TABLE INSTABILITY

The optical table used is a passively damped table in a regular lab space. The technical characteristics of the table could not be retrieved, but dynamic instability of the environment provided by this table is unlikely. The laser sensors used could detect vibrations caused by people walking or jumping next to the table, but they were close to the threshold of detection of the sensors. The sensor reading when a person jumped vigorously next to the optical table shows a maximum transient displacement of less than 1.5 μm and vibrations were undetectable after 10 seconds. The sensor reading during this jumping check can be found in **Figure 4.16**. No influence of building vibration, air conditioning or elevator operations can be detected during long term tests.

4.5.3. ERRORS IN DATA INTERFACE

TEMPERATURE GRADIENTS

Even assuming the temperature sensors are ideal, they only provide the temperature at the point in which they are attached. The temperature field elsewhere is not known. Examining the constitutive equation 4.5 it is apparent that the unit of analysis in this model-experiment system is a beam which expands along its axis, but it does not bend due to its

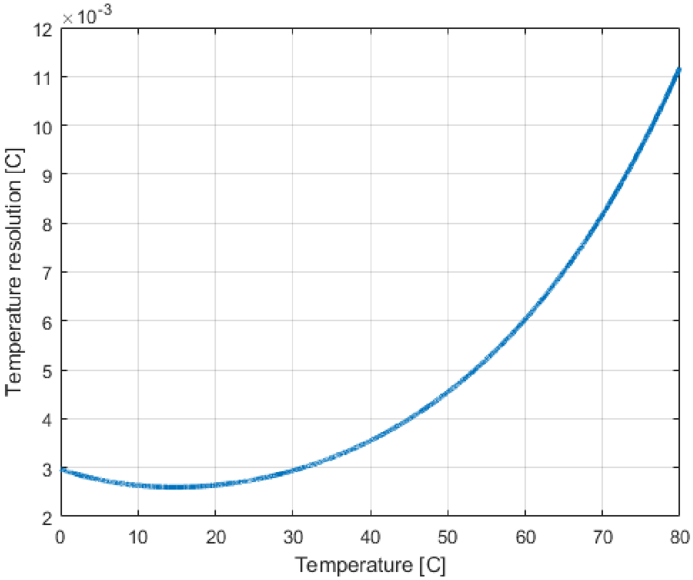

Figure 4.15: Temperature resolution as a function of temperature based on voltage resolution of the ADCs.

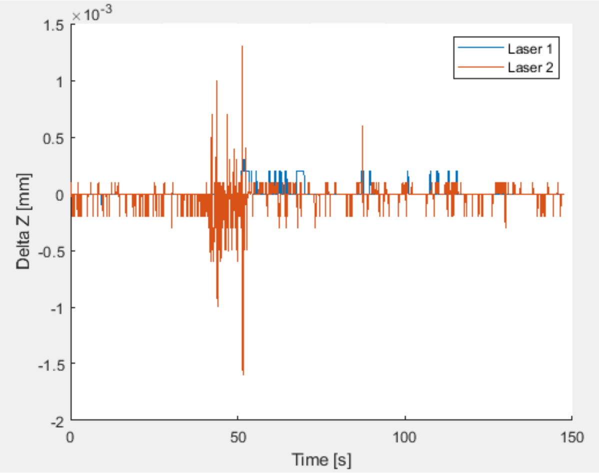

Figure 4.16: Sensor readings during a sanity check where a researcher jumped and tapped the floor next to the optical table.

own temperature field. Gradients along the transverse directions of the beam can have a bending effect (**Malik and Kadoli, 2018; Manolis and Beskos, 1980**) on beam elements, which is not captured in the model proposed here. This is true of any fast-acting surface heating method, such as the heating used in this experiment. The effect is smaller in materials with high thermal diffusivity, which is the case of aluminum, but it cannot be discarded as a source of error. The impact of temperature gradients however will be further studied with the result analysis with bulk temperature change.

DATA IMPORT

Experimental data are split between temperature sensor data and displacement sensor data, which work with different sampling rates and begin acquisition at different times. These are merged into a single data structure by a script which uses the timestamps of both data streams and synchronises them so that they are both in the temperature sensor time axis. Both displacement and temperature sensor data are interpolated to find comparison and input values for the model, respectively. The interpolate function was checked by plotting original and interpolated functions, and these were found to be indistinguishable to machine precision. In order to prevent loss of information during processing, the raw voltages of the temperature sensing system are always recorded, so that the temperature values can be traced back and corrected if necessary.

The next step is calculation of the differential temperatures to an initial steady state and assignment to geometry. This is a manual process that requires matching the model's geometric representation to where the sensors were physically placed. The temperature field in each element was calculated as the measured temperature in elements with an NTC attached and as the average of the two closest NTCs for elements that were not directly measured.

HEAT FLUXES

Heat leaks and unknown thermal couplings have been proposed as a source of uncertainty in the model. The interface between the heaters and the test item has not been characterised in this procedure, and the open structure allows heat to escape to the environment. This may represent a problem with the repeatability of the experimental setup as a whole, but should have no influence on the model performance in predicting the deformation of the mechanism. Thermal expansion is a state function of the temperature, which is directly measured, and therefore as long as the temperature field is known by sensing it, the underlying heat fluxes determining it are not necessary for reliable prediction of the mechanism deformation.

4.5.4. ERRORS OF INTERPRETATION

CAD MODEL TO GEOMETRY

It is possible that the manufacturing process of the test item deviates from the original specifications. As long as such deviations are known, the model can be adapted to fit the new geometry. The test item was manufactured following the ISO 2768 manufacturing standard,

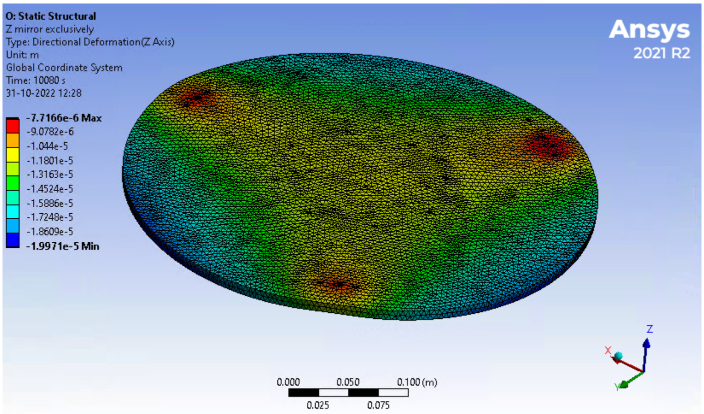

Figure 4.17: Z-axis displacement due to the constrained thermal expansion caused by the bipod struts on the dummy mass for a 10K temperature increase.

with medium tolerances. Parts were checked with a calliper to verify that the nominal dimensions were used. One error was detected in the flexures connecting the moving frame to the fixed frame, which were expected to be 2.4 mm thick and were made 1.4 mm instead. The rest of dimensions examined were correct. Two critical tolerances are the flexure thickness and lengths because of the radius of the wire on wire electrical discharge machining (EDM) processes. These could not be measured directly, but they were included in the sensititivity analysis to check whether they would change the behaviour of the mechanism significantly.

DEFORMABLE END EFFECTOR

In the model, the end effector is assumed to only deform in radial and thickness directions, but not in bending. The boundary conditions provided by the flexured bipods should transfer small loads and so prevent bending due to the end effector's expansion. However, the bipods were designed to hold a lightweighted mirror, and the dummy steel plate is less stiff than a silicon carbide mirror would be. Bending of the plate due to the bipods constraining is thermal expansion was estimated using a separate Ansys FEM model and was found to be small compared to the overall mechanism deformation. The results of independent, constrained thermal expansion simulated by Ansys are shown in **Figure** 4.17. Since the plate is mounted on flexured struts, the figure includes a *Z-axis* rigid body motion plus bending due to the stiffness of the struts. The bending effect at the probing points can be characterised by computing the difference in displacement between points along the X and Y axes. The effect of bending calculated in this manner is 0.4 μm/K for the *X-axis* and 0.03 μm/K for the *Y-axis*. The notable difference in this effect reflects that expansion is less constrained in the Y direction.

NON-LINEARITY

Linear thermoelastic behaviour is an underlying assumption of the model. It is common with isotropic metallic materials, like those used in this research. Non-linear behaviour is found most commonly in load-bearing interfaces, which is one of the topics covered in **Chapter** 2. The design of the test item is supposed to prevent non-linear behaviour by the use of flexured elements to carry whatever loads are transferred between the elements. In any case, linear elastic behaviour can only be assumed at this point.

QUASI-STATIC BEHAVIOUR

Quasi-static behaviour is a very common assumption in thermoelastic problems, though it may not hold in structures with first natural frequencies which are of the order of the inverse of the timescale of the problem. In this case, the first eigenfrequency ω_1 of the test item was found experimentally in the order of 27 Hz. The experiment is carried out in timescales, t_{exp}, on the order of hours and observed oscillations in displacements have are at least at the rough order of magnitude of tens of minutes. The relation between the first eigenfrequency and the characteristic timescale of the thermal deformation is therefore:

$$\frac{1}{\omega_1} \ll t_{exp} \tag{4.9}$$

and quasi-static behaviour can be safely assumed.

DEFORMATION AND POSE

The SPACAR model calculates the displacments of the nodes, which is used to compute the change in pose of the end effector. The laser triangulation sensors, in turn, yield the vertical displacements of the points they are probing. The comparison between sensor readings and model results can be made in pose terms, or displacement terms. It is most convenient to express the model output in terms of Z displacement at the probe point. The relation is given by:

$$\Delta Z_{sensor} = \Delta Z_O + \theta_x * y_{sensor} - \theta_y * x_{sensor} \tag{4.10}$$

where ΔZ_{sensor} is the vertical displacement of the end effector at the sensing point, and x_{sensor} and y_{sensor} are the planar coordinates of the sensing point. ΔZ_O, θ_x and θ_y are the pose parameters as modelled by SPACAR. The inverse relation can only be found if the two sensors are aligned along one of the x- or y- axes for the piston displacement at the origin, ΔZ_O, and one of the rotations, either θ_x or θ_y.

4.6. RESULTS

In this section, the combined results of the experimental setup and the thermoelastic model will be discussed. The experiments have been categorised according to which points were probed with the laser sensors. The sensors are placed over four points according to the schematic seen in **Figure** 4.18. The four points are arranged along the positive and negative x- and y- axes of the mechanism.

4.6.1. TEMPERATURE RESULTS

The important factor in the proposed testing method is the difference between an initial temperature field and the field at a different testing time. If the assumption of quasi-static behaviour holds, it does not matter that the initial or final temperature fields are not in

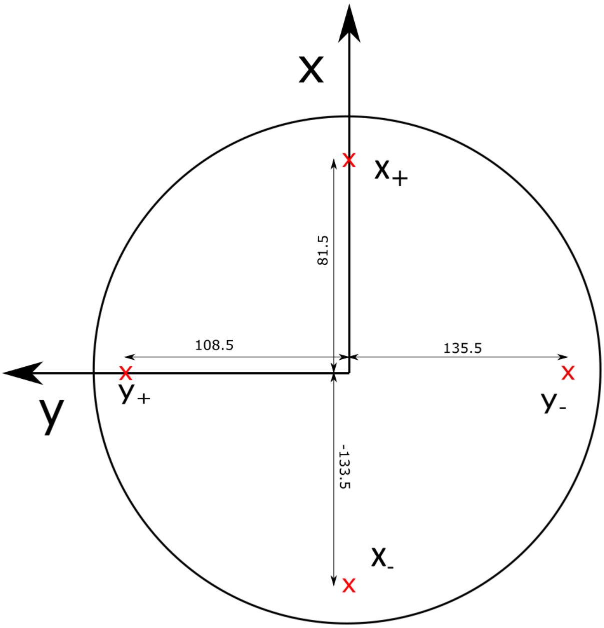

Figure 4.18: Locations of the probing points. Distances are expressed in millimetres

steady state. However, there is an interest in characterising the purely thermal behaviour of the setup. The repeatability and reproducibility of the results depend on external conditions, primarily on the temperature at a given day. Since the positioning of the laser sensors has no influence on the temperature field, all data from the tests can be combined for this part of the analysis. A total of 20 standard tests were carried out with all heaters powered at 20 V for three hours. One of these tests was carried out before the setup had completely reached the steady state. This latter test demonstrates that the thermal steady state of the setup does not depend on the initial conditions, as expected.

The raw temperature results from thermistor 1, placed on the same dummy actuator as heater number 2 on **Figure** 4.8, are shown in **Figure** 4.19. The same test is shown here, carried out in different moments. A 2.7 degrees difference between the coldest and the hottest days within the room in the starting temperature can be observed. The corresponding spread of steady state ’hot’ temperatures is 3.8 degrees. The standard deviation of this distribution is 0.872 degrees. Noise increases in the hot case, but this is not explained by the increase in temperature, as shown by the chaotic behaviour of noise standard deviation and steady state temperature shown in **Figure** 4.20. Possible explanations for this could be a changing contact pressure between the sensor and the test item, instability of the power supply, or electromagnetic interference, but no conclusion can be drawn at this stage.

The temperature in the experiment is also sensitive to the integration of the setup. Thermal interfaces are notoriously difficult to predict, and in this case they depend on the quality of the fit between the heater and the setup. **Figure** 4.21 shows the average temperatures reached by the different actuator stacks. This figure illustrates the dependency of

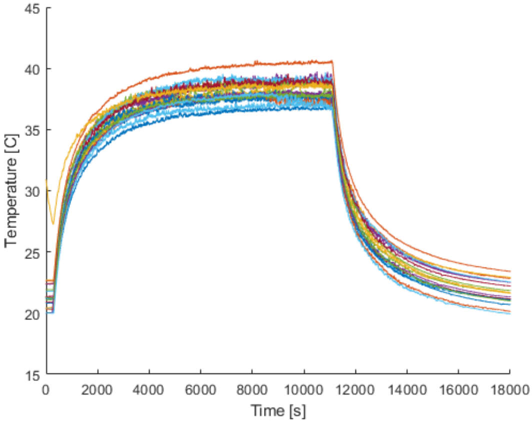

Figure 4.19: Absolute temperature measurements on thermistor 1 across 20 different iterations of the experiment.

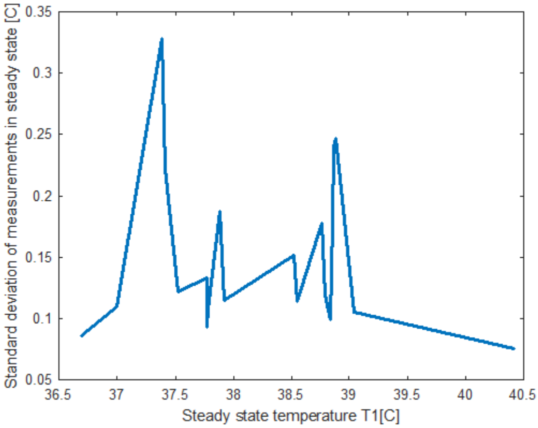

Figure 4.20: Standard deviation in steady state temperature versus steady state temperature in thermistor 1.

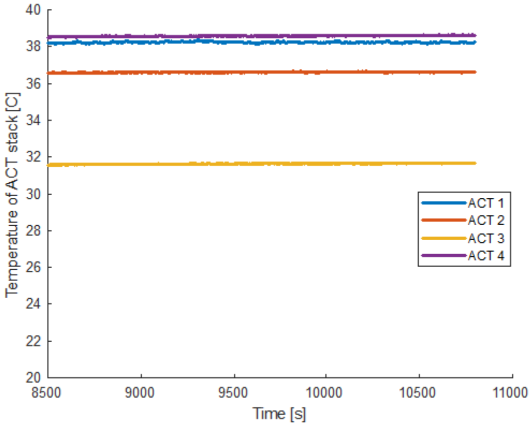

Figure 4.21: Average steady state reached by the different actuator stacks. Stacks 1, 2 and 4 in this case, have a heater integrated and actuator 3 does not. The spread in steady state temperature among the actuators shows that the specific integration between the heater and the test item is not repeatable.

the steady state temperature field on the integration between the heaters and the actuator stack, which would change how much heat actually flows into the setup and how much is lost. The three stacks with heaters integrated reach different temperatures, but the stack which has no heater also sees its temperature increased.

Some of the average differential temperatures used on the thermoelastic model are shown in **Figure** 4.22. It can be observed that the temperature of the metrology frame varies little compared to the major assemblies of the system.

4.6.2. DISPLACEMENT RESULTS

Displacement results are split among the four cases according to where the sensors were placed, with the four locations shown in **Figure 4.18**. Cases are labelled $[-X, X]$, $[-X, -Y]$, $[Y, X]$, and $[Y, -Y]$ for the points that were probed, which were in either the positive or negative sides of the X and Y axes.

Experiment $[X - X]$ was performed a total of six times under the same conditions, **Figure** 4.23 shows the unprocessed output of the laser sensors for the six different tests. Despite the good repeatability of the temperature field, both the starting point of the experiments and their results are not repeatable. No realignment operations were performed on the sensors, yet the starting point of the different experiment runs are significantly shifted. This shift is shown as a function of the initial temperature of the setup in **Figure** 4.24, which indicates this shift is not an exclusive function of initial temperature. As the experiment is concluded, the laser readings also do not fully go back to their initial state. This can be observed more clearly in **Figure** 4.25, where the differential displacement is shown. Differential displacement, ΔZ, is the displacement of the probed points in the test item's reference frame and is

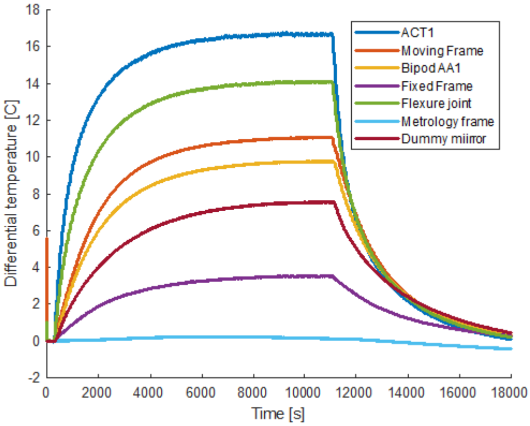

Figure 4.22: Differential temperatures across the test item and averaged over the different standard test runs..

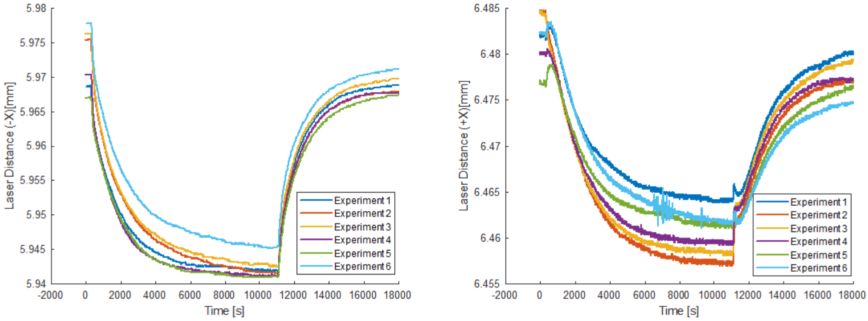

Figure 4.23: Raw laser readings in the [-X,X] test configuration.

calculated from the raw displacement as:

$$\Delta Z(t) = -(z_{laser}(t) - z_{laser}(t_0)) \tag{4.11}$$

where $z_{laser}(t)$ is the raw output of the sensor and t_0 the time at the beginning of the experiment. In order to remove random noise effects, a 5 minute period is left between initial data acquisition and the start of the experiment proper and $z_{laser}(t_0)$ is taken to be the average value over that period.

The fact that the experimental setup does not return to its initial state, which would be expected in linear thermoelastic behaviour, indicates there is some type of history dependence in the test item and/or the displacement sensing method. In order to better illustrate this behaviour, the differential displacement is shown against a synthetic average temperature indicator in **Figure 4.26** for experiment number 5. Similar behaviour can be seen in other experiments.

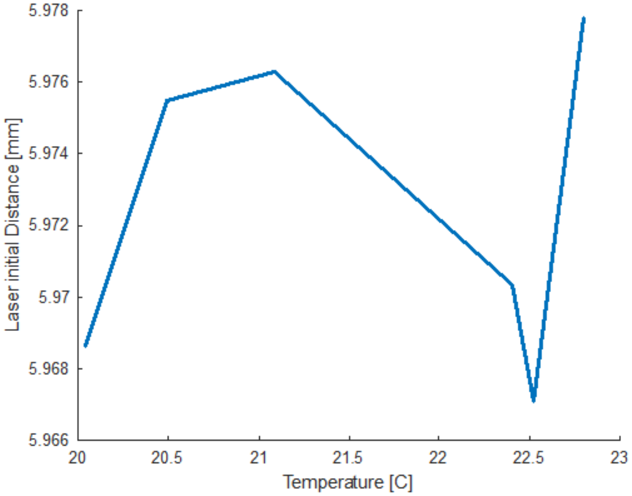

Figure 4.24: Initial temperature reading as a function of temperature, showing no clear tendency. This indicates a history dependence of the laser pointer position.

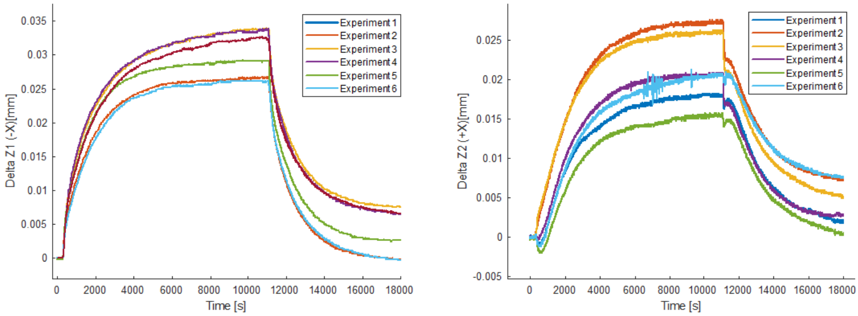

Figure 4.25: Differential displacement as a function of time in [-X,X] configuration

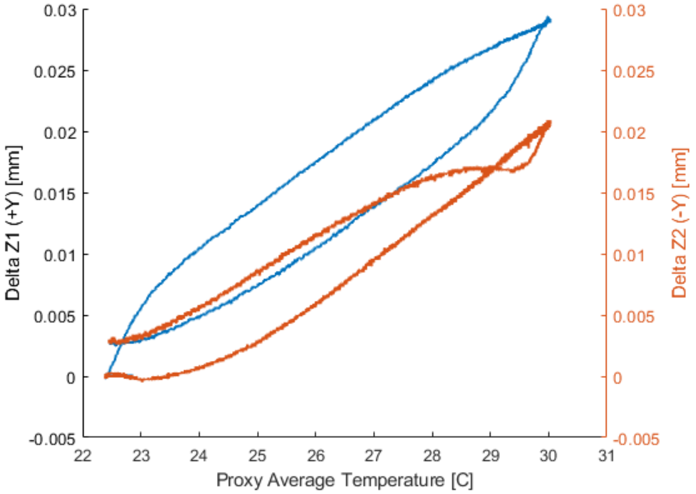

Figure 4.26: Measured displacement plotted against the average temperature of the setup. The average temperature of the setup is used as a proxy for experiment progress, as a single temperature of the setup cannot be defined.

The most immediate feature of this plot is the loop-type behaviour, where displacement does not follow the same path on heating and cooling, and does not go back to the original position. Another features is the bending of the loop at the high extreme of the temperature. These are likely a defect of using the average temperature as a proxy for the experiment advancement. As some elements which are comparatively warmer or have faster responses, but are critical in the final displacement lose temperature very rapidly, the average temperature remains relatively unaffected but the sensor reading changes rapidly. Results for the $[Y-Y]$ cases are shown in **Figures** 4.27 and 4.28. The cases which are executed in the same way, as expected, yield similar results for the points which have been covered. There is not a perfect match when temperature approaches its initial state with initial displacement. This might indicate the influence of residual hysteretic behaviour in the test item, which is not expected in this type of mechanism. As discussed in **Chapter** 2, this type of behaviour is typical of frictional interfaces. However, it cannot be definitely concluded because the test protocol did not give enough time for the setup to completely cool down to the initial temperature.

4.6.3. MODEL PERFORMANCE

The model and the experimental results are compared on the basis of the displacement of the probing points. The model takes measured temperature data and produces a prediction of what the displacements of these points would be. These are compensated for factors not included in the model, mainly the metrology frame expansion, and compared to the output of the sensor as calculated from equation 4.11. The comparison needs to be done in absolute terms due to the different underlying mechanisms determining the pose of the end effector.

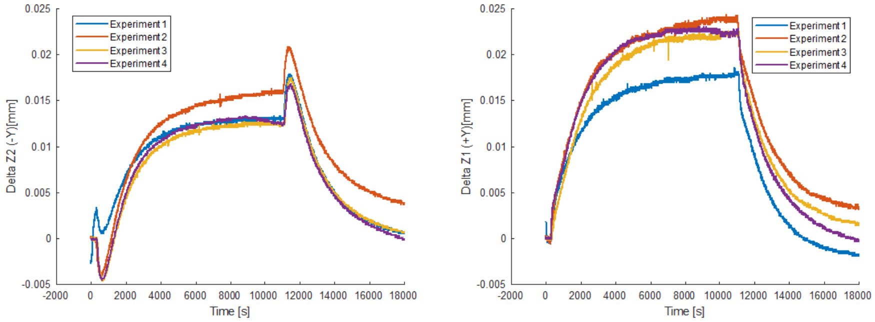

Figure 4.27: Differential displacement as a function of time in [-Y,Y] configuration for four different test runs.

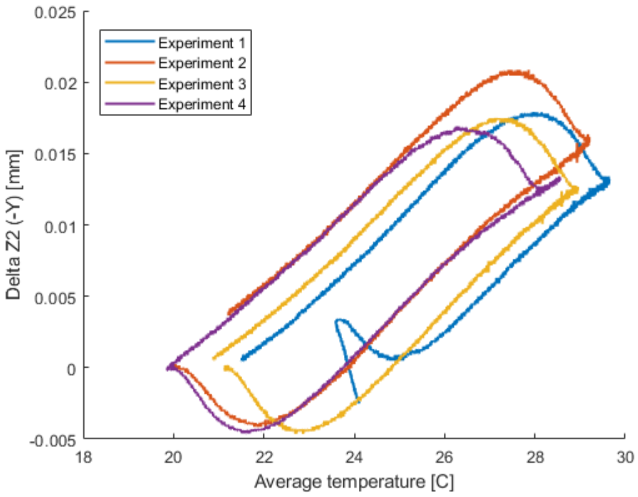

Figure 4.28: Measured displacement plotted against the average temperature of the setup for one of the laser sensors in [-Y Y] configuration.

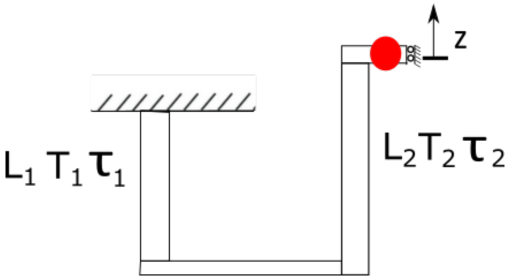

Figure 4.29: Simplified two-beam system, with beam 1 characterised by parameters L_1, T_1 and τ_1, which are the length, the temperature and the thermal time constant respectively. Beam 2 is characterised by L_2, T_2 and τ_2. The end effector is indicated by the red dot.

The reason for this can be visualised with a simple two-beam system, where the beams have different lengths, temperatures and thermal time constants, but the same coefficient of thermal expansion. The beams are connected in series and in opposition, with an end effector only allowed to move in vertical direction, as shown in **Figure** 4.29. The thermal constants of this example are such that $\tau_1 << \tau_2$. It is clear that thermal expansion of the two beams works in opposition, so the displacement of the end effector is given by

$$\Delta Z_{EE}(t) = -\Delta L_1(t) + \Delta L_2(t) = \alpha[-L_1 \Delta T_1(t) + L_2 \Delta T_2(t)]. \tag{4.12}$$

The solution to a thermal problem where these two beams warm up at rates determined by their thermal constants is:

$$\begin{aligned} \Delta T_1 &= A_1 e^{-t/\tau_1} \\ \Delta T_2 &= A_2 e^{-t/\tau_2} \end{aligned} \tag{4.13}$$

With A_1 and A_2 being the steady state amplitudes of the temperature increase of each beam. Combining equations 4.12 and 4.13 and giving arbitrary values to the problem's parameters, **Figure** 4.30 can be found. This figure shows that in cases where a minor element of the kinematic chain reacts fast, it can initially dominate the final displacement over a slower-reacting, larger element. Note also that **Figure** 4.27 shows similar behaviour in the initial stage of the test. The steady state which results is simply the addition of the steady states of the smaller subsystems. However, if the functions $\Delta L_1(t)$ and $\Delta L_2(t)$ are not known, and can only be estimated through a model, the relative error of the model cannot be defined. If, in this example, $\Delta L_2(t)$ is estimated to be zero, and $\Delta L_1(t)$ is known with accuracy, the model will show a large error in smaller time scales and a steady state error of the full influence of $\Delta L_2(t)$. However, such a model would not be well understood to be better in steady state than in short transient. Unfortunately, given the final displacement, it is not possible to decompose it into its components, because the underlying mechanisms are not described by a set of orthogonal functions which can be separated uniquely. This problem of interpretation thus remains in the experimental procedure studied here.

Figure 4.31 shows the estimated and experimental vertical displacements in experiments of [-X X] and [Y -Y] configurations. It is shown that the models significantly underpredict displacements in both cases. This is consistent across different experiments. The

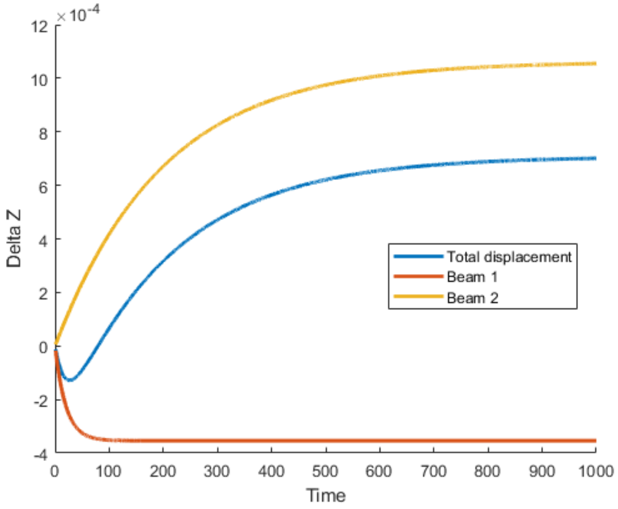

Figure 4.30: Possible solution to the sample thermoelastic problem of two beams in opposition with different rates of temperature change. Note that units are generic.

models do predict the aforementioned behaviour of opposing thermal expansion mechanisms, which is also present on the experimental results in the case of laser 2 in [Y -Y] configuration. Overall, the model can be speculated to predict displacements well on the first 1000 seconds of the test, but then overpredicts the importance of an underlying thermal expansion mechanism. However, this cannot be confirmed due to the lack of a physics-based decomposition of the results. **Figure** 4.32 shows the error of the model calculated as

$$e = \Delta Z_{exp} - \Delta Z_{model}. \tag{4.14}$$

Note the absolute error is 0 by definition at the start of the test, so the model performance is poor over most of the operational range. Though point -X presents more error than any of the others, steady state errors in all cases are of the order of the output, and

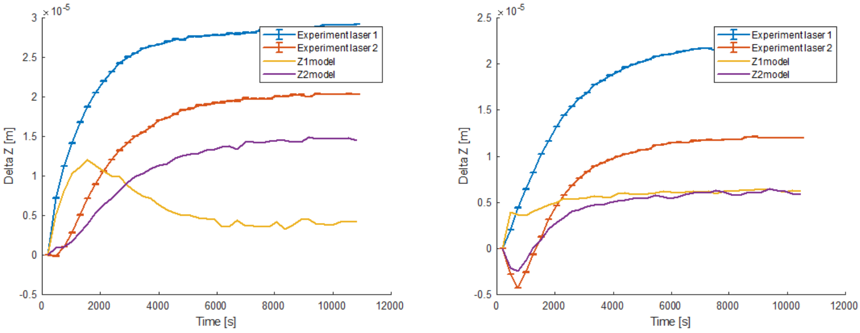

Figure 4.31: Model predictions and experimental results of displacements at the four points measured over two different tests in [-X X] and [Y -Y] configurations respectively. Left figure shows [-X X] and right figure shows [Y -Y].

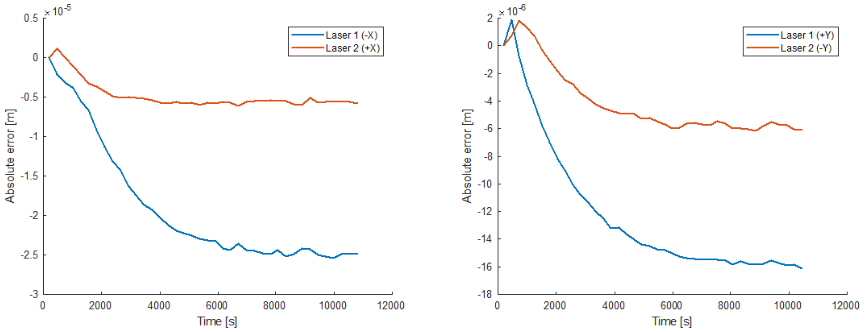

Figure 4.32: Absolute error of the model compared to experimental results. Left figure shows [-X X] and right figure shows [Y -Y].

so the model cannot be validated at this stage. Some factors will be further explored in the sensitivity analysis.

4.6.4. SENSITIVITY ANALYSIS

Since the results of the tests and the experiments do not match, a sensitivity analysis was proposed to check if some important properties of the system fundamentally change the behaviour of the model so that it becomes significantly closer to compliance than the baseline run. The properties analysed here have been assigned a reasonable level of variability so that if the property is critical for the final model performance, it will have a high probability of explaining the lack of compliance of the model. The components of this sensitivity analysis are mainly computational. The influence of material properties, flexural geometry and detected temperature will be explored on a sample experiment. These properties can be altered within expected bounds when defined in the model. An additional sensitivity explored is the sensitivity to control voltage. The power dissipated in the experiment depends directly on the voltage at which the heaters are powered, and it could be that a lower voltage yield a better result.

MATERIAL PROPERTIES

The material properties with a possible influence are the Young's modulus, the bulk modulus, and the coefficient of thermal expansion. Of these three, in a first approximation, the Young's modulus would not be expected to have an influence because the equivalent thermal stress scales with it, and the element stiffness in longitudinal direction is much larger than any flexural element which can constrain its expansion. Indeed, the Young´s modulus had no significant effect in the results, with differences in the order of less than one nanometer. In the same way, the bulk modulus was not found to have an effect in this model. The influence of the coefficient of thermal expansion is illustrated in **Figure 4.33**, but these values do not change the overall behaviour of the test item and do not bring the model significantly closer to the experimental values. Whilst coefficient of thermal expansion has a comparatively large effect compared to other material properties or other parameters included in the sensitivity analysis, thermal expansion is a well-known physical

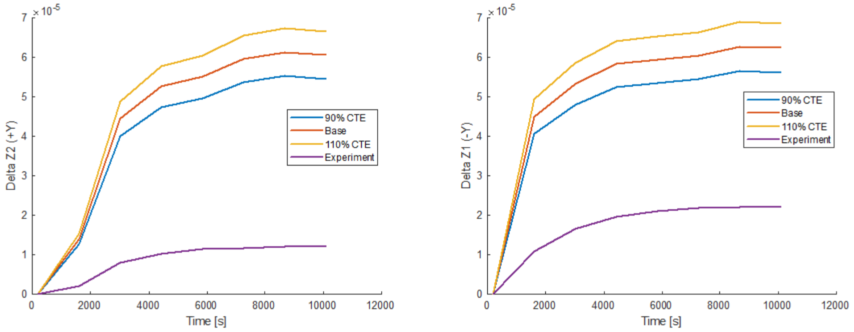

Figure 4.33: Results of a thermoelastic model run for three values of coefficient of thermal expansion.

property given a material alloy, and the level of variability described here covers getting the alloy denomination wrong, and not merely possible variability in the chemical composition of the alloy.

FLEXURE GEOMETRY

Flexures manufactured through wire EDM may present a systematic error due to the thickness of the wire, as this creates a transition zone between body of the work piece and the thin flexure attached. There is an indetermination of the precise equivalent flexure length, but the sensitivity to this effect can be examined. Also, the thickness of the flexures can be subject to similar variability due to the use of different passes of the tool in order to remove surface roughness. The sensitivities to the length is ilustrated in **Figure 4.34**. In this case, there is a significant impact in the model's output for a 2% change of flexure length. Interestingly, the effect of thickness of the flexures was much smaller, in the order of 0.2 μm for a 5% change in thickness. This may be surprising due to the strong dependence of the bending stiffness of blade flexures with thickness. This indicates that in this thermoelastic problem, flexure bending is less important than longitudinal length, which is consistent with the modelling of each element as a longitudinally expanding beam. These flexures are designed to bend significantly, and so a small increase in their stiffness has little effect.

TEMPERATURE SENSING AT HEATED ELEMENTS

There is reasonable doubt of whether the temperature sensing is representative of the real temperature at the points where there are heaters attached. The reason is the effect of thermal conductivity in the beams which are subjected to direct surface heating. The point on the surface where temperature is measured is not directly in contact with the heater, and the heater is at higher temperature than the beam. The temperature distribution will be more homogeneous the more conductive the material, but there is likely significant variability. This effect is illustrated in **Figure 4.35**.

Note that this effect is the origin of thermal bending, but since the elements subjected in contact with the heaters are released at the ends by flexure joints, this bending is not transmitted to other elements in the test item. The influence of this effect was studied by

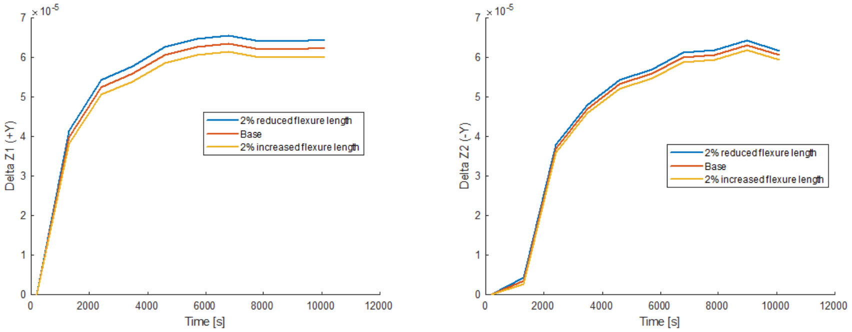

Figure 4.34: Differential displacement in a [Y -Y] test for three settings of flexure length, illustrating the sensitivity to this parameter.

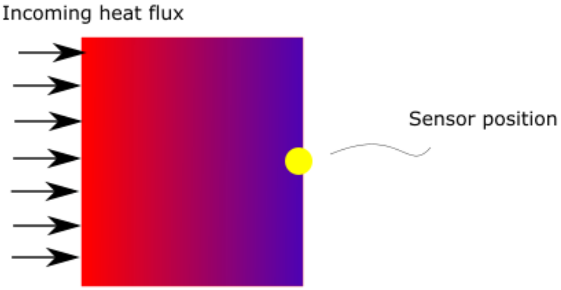

Figure 4.35: Temperature distribution in a beam cross section where only one side is heated and a sensor is placed on another. The red to blue scale represents higher to lower temperatures.

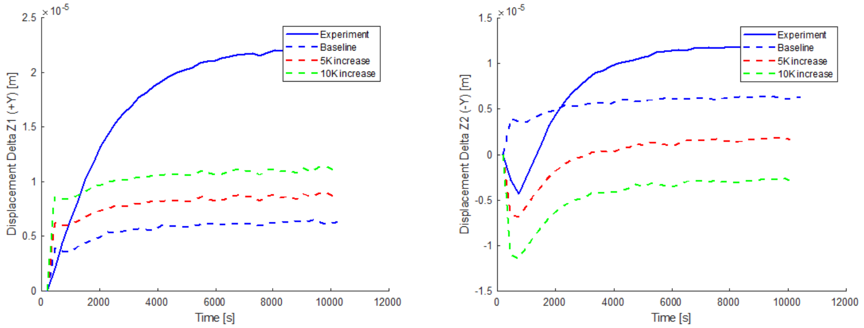

Figure 4.36: Displacements predicted by the model with two different temperature offsets, together with experimental results.

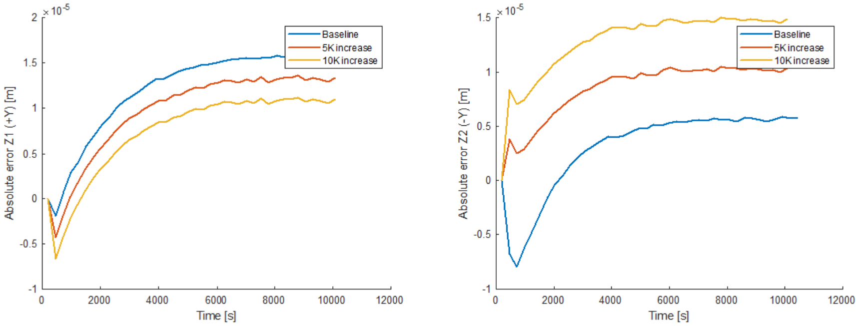

Figure 4.37: Error of the model predictions to the experimental results with two different temperature offsets.

introducing a constant increase in temperature to the readings of the thermistors located at the heated beams. **Figure** 4.36 shows the displacements predicted by the model with this modification and the experimental result in a [Y -Y] experiment.

This result just introduces an offset in the final model outputs. This can change the shape of the early response of the system, as shown by the right side of **Figure** 4.36, but in the steady state just introduces an offset. **Figure** 4.37 shows the absolute error with these temperature offsets. As a sensitivity parameter, this mechanism is the most promising to bring the model to compliance, due to the large uncertainty in the temperature field and its large impact. It is possible that the form of sensitivity in temperature implemented, as a simple offset in time domain, does not reflect the effect of gradients across a single element. However, it is unlikely that this can bring the model to compliance with the experimental values, because for the same offset, errors on the two probed points show very different results.

4.6.5. COMPARISON TO ANSYS MODEL

A separate model of the setup was built in Ansys Workbench. Ansys has the advantage of automatically handling all degrees of freedom allowed due to the use of a more general form

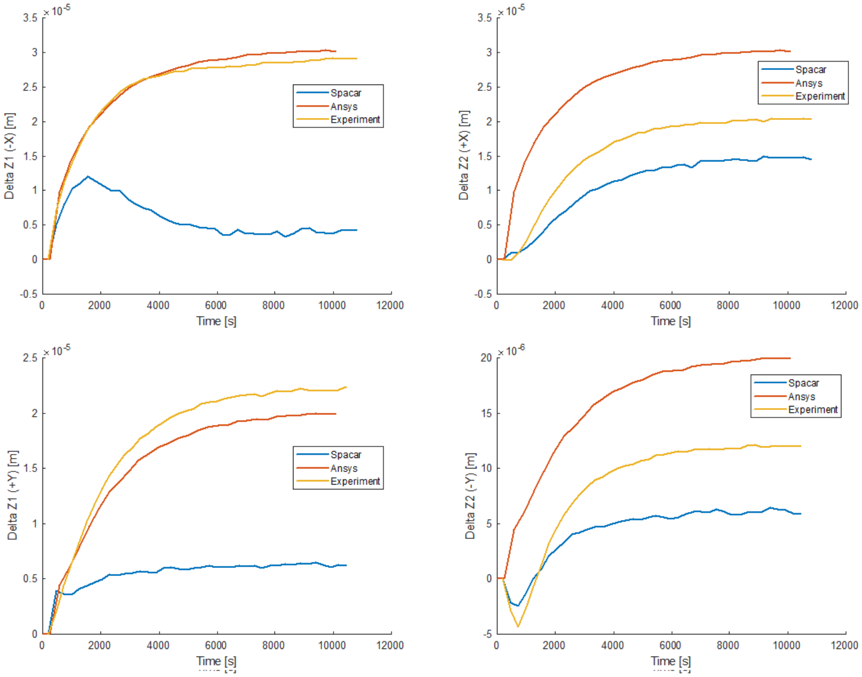

Figure 4.38: Experimental, SPACAR and Ansys displacement results for tests [-X X] and [Y -Y].

of the elastic problem. Ansys computes the solution to a given elastic problem faster than SPACAR and is more user friendly. On the other hand, performing sensitivity analysis to the different parameters of the setup is much more difficult to implement in Ansys than in SPACAR. In addition, Ansys requires a much more developed model of the mechanism, which limits its usefulness in early stage studies.

The results of the simulations by SPACAR and Ansys are shown in **Figure 4.38** for the four points, gathered from two different tests in [-X X] and [Y -Y] configurations. It is shown that both in points -X and +Y, Ansys is significantly closer to the experimental results than SPACAR, which indicates that Ansys likely does model some dynamic of the system which is not present in SPACAR. What this dynamic is, however, cannot be found from these results. However, in positions +X and -Y, SPACAR predicts better than Ansys, although the absolute distance is larger. SPACAR also predicts the initial negative displacement found in position -Y early in the test, which Ansys does not. In light of this data, none of the two models can be fully trusted to predict experimental results in the thermoelastic behaviour of such mechanisms. The absolute errors calculated from these displacements are included in **Figure 4.39**.

CONTROL VOLTAGE

A test in [-X X] configuration was performed with heater voltages of 10, 15 and 20 V. Note that the power dissipated in each of these steps is not linear with voltage, since Joule heating

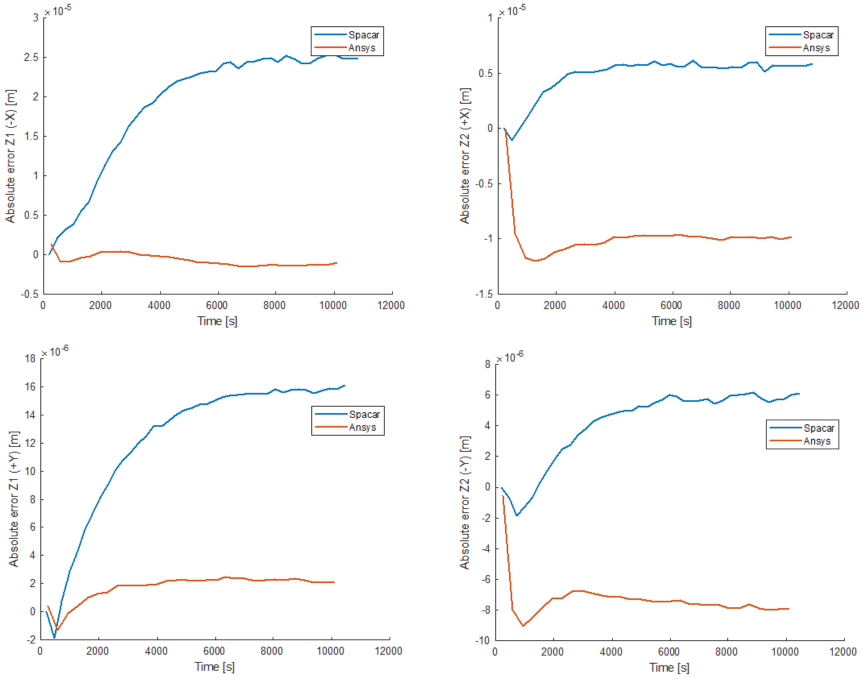

Figure 4.39: Absolute error of SPACAR and Ansys for two tests in [-X X] and [Y -Y].

power has a quadratic relation to voltage. In **Figure** 4.40, it is shown that the error increases as the steady state approaches, which is the same result as was obtained in the baseline results. However, in -X position it varies substantially with voltage in all cases, whilst in +X position the behaviour changes substantially only in the last power setting, perhaps due to some mechanisms becoming important only at high heat dissipations. **Figure** 4.41 shows the predicted and experimental displacements.

4.7. ERROR RESULTS SUMMARY

As a summary of the results in estimating the errors in the setup and modelling, **Table** 4.3 has been compiled, showing the expected orders of magnitude of the errors. The errors for which an order of magnitude estimate is not possible, due to either lack of information or fundamental limitations of how they are defined are excluded. Such errors include coding, as coding errors have the potential to completely invalidate a modelling approach and so an order of magnitude estimate is meaningless. Idealization errors are also no easily quantifiable in this context. Temperature gradient errors cannot be estimated because of the lack of information on these potential gradients, as well as the difficulty in propagating them through the mechanism. These same problems are present in the modelling of contact stiffness. Potential violations of the assumptions of quasi-staticity and linear behaviour are also not testable and there is not enough data to include them.

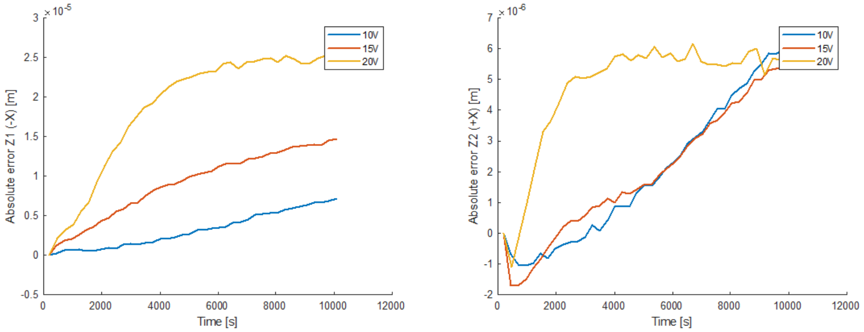

Figure 4.40: Absolute error of the model in [-X X] configuration for three different power settings. Left side shows laser 1 (-X) and right side shows laser 2 (+X).

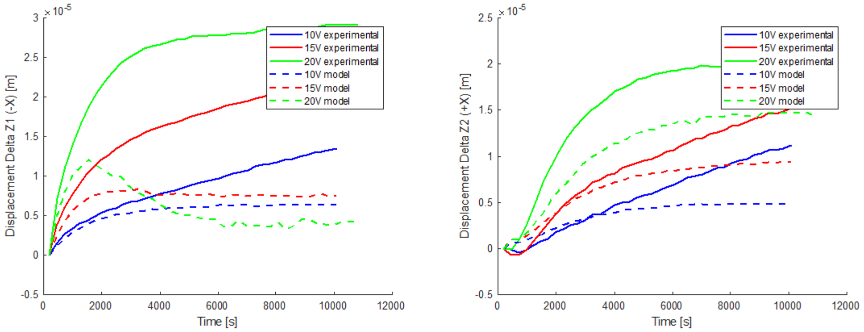

Figure 4.41: Predicted and experimental displacements in the control voltage sensitivity analysis. The experimental configuration used was [-X X].

Table 4.3: Order of magnitude estimates of different sources of error.

Error source	**Error order of magnitude**	**Estimation method**	**Comments**
Geometry representation	<7 μm	Model sensitivity	Since the model cannot be validated, this figure is dubious.
Material properties	<16 μm	Model sensitivity	Very unlikely source of error.
Numerical error	~ 0.001 μm	Model parameters	Can only be estimated from model parametres.
Metrology deformation	<0.67 μm	Analytical	Compensated in modeling.
Temperature sensor noise	<1.4 μm	Experimental/Analytical	Influence likely overestimated.
Displacement sensor calibration	<0.4 μm	Experimental	Threshold of detection is factory-determined.
ADC error	<0.15 μm	Experimental/Analytical	Influence likely overestimated.
Temperature sensor offset	<6 μm	Analytical	Influence likely overestimated.
Displacement sensor placement	<1.5 μm	Analytical	This reflects an uncertainty, but it is a repeatable offset in all cases.
Table instability	<0.4 μm	Experimental	Under threshold of detection under test conditions.

Note that the threshold of detection of the laser sensors is 0.4μm as determined by the laser sensors. Material properties are shown to have the largest potential impact, but as discussed in subsection 4.6.4, only getting the material denomination wrong explains the largest possible impact. Most likely, the variability would be two orders of magnitude smaller because physical properties of standard materials are well characterised. Errors due to temperature sensor offset, resolution and noise are estimated analytically by multiplying them by the total height of the setup and the coefficient of thermal expansion, which means the errors across the different sensors would need to act in the same direction to yield the displacements shown here. Overall, **Table 4.3** represents conservative orders of magnitude of the errors quantified in it.

4.8. LESSONS LEARNED

Even though ultimately the model proposed cannot be validated, there are some lessons that can be extracted to help on future development of optomechanical products under significant thermal loads and more generally to verify and validate thermoelastic models.

Lessons on testing method:

1. Rapid prototyping is useful to check manufacturability and integration of mechanisms in a low-cost manner.
2. Systematic errors in flexure manufacturing have a minor impact in final model predictions in this case. This is likely a result of the dominant effect of longitudinal expansion of flexures and intermediate bodies in this particular setup.
3. It would have been easier to validate the experimental methods with a stepwise approach including test items of increasing complexity over different iterations.
4. No substantial evidence of non-linear behaviour was found in the tests. However, there is a phenomenon of drifting initial conditions which may be a result of deformation of the metrology frame.
5. Neglecting the effect of thermal bending may explain poor model performance, but this is not a testable hypothesis at this point.

Lessons on test setup:

6. Use of NTC thermistors allows to easily measure large numbers of local temperatures, but in this iteration, they have a large spread in the order of ±1 K, which might be caused by spatial variability of the room temperature, but casts doubt on their accuracy. If thermal bending is a concern in this type of mechanism, it might be easier to use thermal infrared cameras instead of any type of contact sensor.
7. The presence of opposing mechanisms of thermal expansion makes it difficult to define relative error requirements for a test setup.
8. The test methodology proposed does not provide sufficient information for analysis of different, opposing expansion mechanisms, because the sensor output cannot be decomposed into constituent orthogonal functions with a clear physical meaning.

Lessons on modelling.

9. Though SPACAR has been demonstrated to successfully model the elementary thermoelastic problem of a cantilever beam with a temperature increase, the same as Ansys 2021, neither of them predict the experimental results in this complex context. However, SPACAR is notoriously less user friendly and slower for this application.

10. As a tool, SPACAR's ability to quickly change system parameters and process results directly in the Matlab environment is offset by its complicated initial setup and limitation to beam elements.

11. Though several sensitivity parameters have been proposed and tested in the model, none of them are significant enough to bring the SPACAR model significantly closer to the experimental results.

12. Intermediate bodies that can be approximated as rigid bodies in quasi-static load cases can dominate dynamic characteristics at frequency ranges above 20 Hz. SPACAR grossly overestimates first eigenfrequencies, but eigenmodes can have some resemblance to experimental ones.

13. In small displacement thermoelastic problems effecting flexure mechanisms, no evidence has been found for an influence of the bulk or stiffness modulus on the results. The coefficient of thermal expansion does have an effect on the model output, but this is a typically well characterised property.

4.9. CONCLUSIONS

A procedure for computational model verification and validation has been described and applied to a thermoelastic model of a flexure mechanism. The main work package of this process was the development, execution and validation of an experimental method to investigate the performance of the computer model. A combined verification and validation procedure was applied to find, to the best of the abilities of the author, all the possible challenges in both the model and the experiment. The results of the experiment and the model have been compared, and unfortunately, the model has not been successfully validated against these results. However, lessons have been extracted from the attempt. A separate Ansys computational model was also compared to the experimental results, and also failed to predict them. The sensitivity analysis has shown dependency of the output respect to different parameters, but none of the factors identified can account for the discrepancy.

BIBLIOGRAPHY

Beards, C. (1995). *Engineering Vibration Analysis with Application to Control Systems*. Elsevier. https://doi.org/978-0-340-63183-6

Cardarelli, F. (2018). *Materials Handbook: A Concise Desktop Reference Third Edition.*

Evers, E., Van Tuijl, N., Lamers, R., & Oomen, T. (2019). Identifying thermal dynamics for precision motion control. *International Federation of Automatic Control*, *52*(15), 73–78. https://doi.org/10.1016/j.ifacol.2019.11.652

Evers, E., van Tuijl, N., Lamers, R., de Jager, B., & Oomen, T. (2020). Fast and accurate identification of thermal dynamics for precision motion control: Exploiting transient data and additional disturbance inputs. *Mechatronics*, *70*(July), 102401. https://doi.org/10.1016/j.mechatronics.2020.102401

Hale, L. C. (1999). *Principles and Techniques for Designing Precision Machines* (Doctoral dissertation). Massachusets Institute of Technology.

Hatamura, Y., Nagao, T., Mitsuishi, M., Kato, K., Taguchi, S., Okumura, T., Nakagawa, G., & Sugishita, H. (1993). Development of an Intelligent Machining Center Incorporating Active Compensation for Thermal Distortion. *CIRP Annals - Manufacturing Technology*, *42*(1), 549–552. https://doi.org/10.1016/S0007-8506(07)62506-2

He, J., & Fu, Z.-F. (2001). *Modal Testing: A Practical Guide*. Elsevier. https://doi.org/https://doi.org/10.1016/B978-0-7506-5079-3.X5000-1

Herzog, R., & Riedel, I. (2015). Sequentially optimal sensor placement in thermoelastic models for real time applications. *Optimization and Engineering*, *16*(4), 737–766. https://doi.org/10.1007/s11081-015-9275-0

Kleijnen, J. P. C. (1995). Verification and validation of simulation models. *European Journal of Operational Research*, *82*, 145–162. https://doi.org/10.4018/978-1-60566-774-4.ch004

Koevoets, A. H., Eggink, H. J., Van Der Sanden, J., Dekkers, J., & Ruijl, T. A. (2007). Optimal sensor configuring techniques for the compensation of thermo-elastic deformations in high-precision systems. *Collection of Papers Presented at The 13th International Workshop on THERMal INvestigation of ICs and Systems, THERMINIC*, (September), 208–213. https://doi.org/10.1109/THERMINIC.2007.4451779

Li, Y., Zhao, W., Lan, S., Ni, J., Wu, W., & Lu, B. (2015). A review on spindle thermal error compensation in machine tools. *International Journal of Machine Tools and Manufacture*, *95*(99), 20–38. https://doi.org/10.1016/j.ijmachtools.2015.04.008

Malik, P., & Kadoli, R. (2018). Thermal induced motion of functionally graded beams subjected to surface heating. *Ain Shams Engineering Journal*, *9*(1), 149–160. https://doi.org/10.1016/j.asej.2015.10.010

Manolis, G. D., & Beskos, D. E. (1980). Thermally induced vibrations of beam structures. *Computer Methods in Applied Mechanics and Engineering*, *21*(3), 337–355. https://doi.org/10.1016/0045-7825(80)90101-2

Morishima, T. (2016). Novel thermal error reduction techniques in temperature domain. https://doi.org/https://doi.org/10.4233/uuid:ffdfd697-640c-419a-b39a-539d57b17d60

Morishima, T., Van Ostayen, R., Van Eijk, J., & Schmidt, R. H. (2015). Thermal displacement error compensation in temperature domain. *Precision Engineering*, *42*, 66–72. https://doi.org/10.1016/j.precisioneng.2015.03.012

Pepper, S. (2018). *Design of a Primary Mirror Fine Positioning Mechanism for a Deployable Space Telescope.*

Rudtsch, S., & Von Rohden, C. (2015). Calibration and self-validation of thermistors for high-precision temperature measurements. *Measurement: Journal of the International Measurement Confederation*, *76*, 1–6. https://doi.org/10.1016/j.measurement.2015.07.028

Saathof, R., Wansink, M. V., Hooijkamp, E. C., Spronck, J. W., & Munnig Schmidt, R. H. (2016). Deformation control of a thermal active mirror. *Mechatronics*, *39*, 12–27. https://doi.org/10.1016/j.mechatronics.2016.07.002

Siemens. (2020). Modal Testing: A Practical Guide. https://community.sw.siemens.com/s/article/Modal-Testing-A-Guide

Vanherck, P., Dehaes, J., & Nuttin, M. (1997). Compensation of thermal deformations in machine tools with neural nets. *Computers in Industry*, *33*(1), 119–125. https://doi.org/10.1016/s0166-3615(97)00016-x

Weck, M., McKeown, P., Bonse, R., & Herbst, U. (1995). Reduction and Compensation of Thermal Errors in Machine Tools. *CIRP Annals - Manufacturing Technology*, *44*(2), 589–598. https://doi.org/10.1016/S0007-8506(07)60506-X

5

CHARACTERIZATION OF PIEZOACTUATOR SELF-HEATING

I'm elected, electric spy,
I'm protected electric eye.

Judas Priest, Electric Eye.

Piezoelectric actuators are a very attractive technology for active optics mechanisms in space applications due to their very high precision and reliability. However, self-heating of these actuators may limit their use in space or under high loads, due to the limited ability to evacuate heat. Test procedures that reproduce the operational conditions of these actuators are important to check these operational limits. Here an effort to characterise the thermal emission of pre-stressed piezoelectric actuators in operation is presented. The technique allows direct measurement of the power dissipated by the test item via the control of the different heat transfer mechanisms, using the fall in power provided as measure of power dissipated by the actuators, instead of relying on direct temperature sensors. This allows the construction of a thermal model with a dissipation term readily integrated in system-level modelling to account for the dissipated heat of the piezo. The technique may also be applied to other piezo low power applications in the order of 1 W of thermal emission, and is adaptable to emulate the boundary conditions encountered in operations.

5.1. SELF-HEATING AS A PROBLEM FOR SPACE INSTRUMENTS

5.1.1. PIEZOACTUATORS IN SPACE INSTRUMENTATION

In previous chapters, the need for several types of actuation mechanisms in space telescopes has been discussed. Though there are other options for powering such mechanisms, piezoelectric actuators are one of the candidate technologies for a variety of designs. Their simple integration, high stiffness, fast response and high repeatability are strong points of actuators based on this principle. Losses present in these materials, as they convert electrical power into motion during repetitive operation cause them to warm up, a phenomenon referred to as self-heating (**Uchino, 2017**). In this chapter, further study on the thermal behaviour of these actuators is presented.

Piezoelectricity is a property of some crystals an ceramics which produce internal polarization in response to mechanical stress, which is the direct piezoelectric effect, or change dimensions in response to an electric field, which is called inverse piezoelectric effect. Piezoelectricity only appears in materials whose crystalline or molecular structure has no centre of symmetry, which also means all piezoelectric materials are anisotropic. The complete behaviour of piezoelectric materials is described by the piezoelectric tensor d_{ij}. Each component represents the mechanical strain in direction j when the material is subjected to an electric field in direction i (**Waanders, 1991**). However, for the purposes of actuation, only one of the components of the tensor is employed, usually either d_{33} or d_{31}, to drive deformation. When used in this way, these are called the piezoelectric coefficients or constants.

Piezoelectric actuators exhibit complex behaviour from a control standpoint, characterised by strong field-polarization hysteresis (**Yu et al., 2002**). In addition, piezoelectric materials are subject to creep and saturation (**Abdul Satar et al., 2020**). Even so, piezoelectric actuators are capable of reaching resolutions in the order of one nanometre, provided accurate control can be designed. Several approaches are described in the literature for drive and control of these actuators (**Minase et al., 2010; Sabarianand et al., 2020**).

5.1.2. SELF-HEATING OF PIEZOELECTRIC ACTUATORS

Piezoelectric ceramics are classified in soft and hard (**Gao et al., 2020**). Hard piezoelectric materials tend to have smaller piezoelectric constants. They are used for applications where small displacements and high frequencies are needed. Typical examples are ultrasonic transducers. Soft piezoelectric materials have larger piezoelectric constants, which produce larger strokes. This is advantageous for actuators which work at lower frequencies. The latter type of material is of interest for this research since the application is a precision actuator. In addition, piezoelectric actuators may operate in linear mode or in bending mode, and are embedded in a wide variety of motion amplifiers (**Gao et al., 2020; Mohith et al., 2021**). In this chapter, the focus is given to linear-mode actuators constructed out of piezoceramics. These actuators have a smaller range of motion with respect to stepping bending mode actuators, but have much higher stiffness and blocked force. The linear actuators used in applications where high precision is needed are pre-stressed by a frame, which reduces stick-slip behaviour at the interface between the mechanism and the actuator and provides a standard interface. **Figure 5.1** shows a linear pre-stressed piezoelectric actuator that was used in the tests of this study.

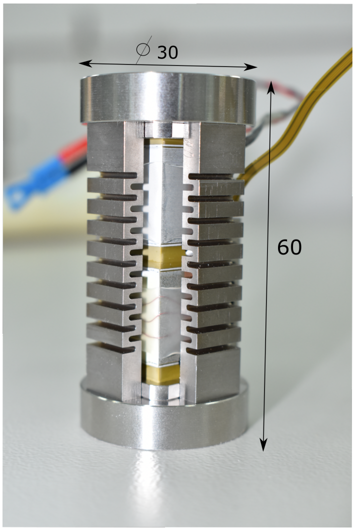

Figure 5.1: Pre-stressed actuator, a test item for this study. The inner part is the multi-layer piezoelectric stack with integrated electrodes, whilst the outer part is the preloading structure. Dimensions expressed in millimetres.

Self-heating is the dissipation of thermal power as a result of the loss of energy when transforming electrical power into mechanical power or viceversa. Self-heating of piezoactuators may be a challenge both in optical and thermo-mechanical terms. Even before complete thermal failure of the actuator, additional heat may disturb measurements in thermal infrared (TIR) instruments. Heat leaking from the actuator may cause misalignment due to thermal expansion of either the actuator or its surroundings. In addition, self-heating has been identified as a potential source of runaway thermal failure due to increased current draw at high temperatures (**Stewart and Cain, 2014**). Self-heating also changes the electrical properties of the actuators, which are sensitive to temperature, and need to be compensated (**Somwan et al., 2015; Yoo et al., 2020**). Materials for high thermal stability may be designed, but the temperature dependence is difficult to remove (**X. Liu et al., 2015; Lu et al., 2018**). Weaver et al. reviewed several methods of characterization of piezoelectric parameters in high temperature materials (**Weaver et al., 2015**). Temperature measurement as a control parameter has been proposed to compensate for temperature dependance of actuator capacitance (**Islam et al., 2011**). Thermal cycling, which can be caused by self-heating, has been identified as a factor in adhesive bonding failure in piezoelectric sensors (**Blackshire et al., 2006**). Tests addressing this phenomenon are important to qualify the system and build a reliable thermal model of the mechanism.

Prior experiments on the self-heating effect of piezoelectric actuators have relied on a transient analysis of the actuator response (**Senousy et al., 2009; Uchino and Hirose, 2001; Zheng et al., 1996**). In this method, the actuator is initially inactive and upon activation with a given frequency and amplitude, self-heating begins. Pritchard et al. (**Pritchard et al., 2004**) inverted the approach to calculate heat dissipation of multi-layer actuators. If temperature is plotted against time in this configuration, the response is analogous to a step response of a first order system. The exact parameters of the decaying exponential solution to the transient thermal problem are fitted via a parameter k_T which models the system dynamics. Zheng (**Zheng et al., 1996**) gives a solution to this transient of the form

$$\Delta T = \frac{k_1}{k_T}(1 - e^{-\frac{k_T}{k_2}t}) \tag{5.1}$$

with k_1 and k_2 being two constants describing the system parameters and ΔT the temperature rise. k_T includes the conductive, radiative and convective couplings of the actuator to its environment and allows a description of the behaviour as a first order system. However, such a study does not allow direct computation of the generated heat flow. Moreover, k_T is a fitting parameter which is difficult to trace back to first principles if the thermal couplings to the environment are not well characterised. In addition, these models are difficult to integrate into system-level thermal models where boundary conditions are complex.

In this study, the goal of the test setup is to observe the self-heating in a more direct manner, without relying on such transient fitting techniques. The observation principle here is based on steady state thermal equilibrium between the test item and its environment. Another measurement procedure relying on steady-state measurements was carried out by Quattrocchi et al. (**Quattrocchi et al., 2018**). Their goal was to examine the influence of the enclosing materials on the temperature rise of a piezoelectric patch. However, the authors do not calculate heat production directly.

In this test setup, a more thorough control of thermal boundary conditions is also sought. The objective in the test setup design was to create a single possible thermal path for heat to flow from the actuators into a cold reservoir. Prior to actuator self heating, the setup will be dissipating a known amount of heat with the main thermal path at a constant temperature. The temperature of this path will remain under control once the actuator is switched on. Therefore, in order to keep steady state thermal equilibrium, the known dissipated power will fall by the same amount as the actuator dissipates.

5.2. MODELING SELF-HEATING

Self-heating has been studied previously in the context of fuel injectors by Senousy et al (**Senousy et al., 2009**) and in general by Ronkanen et al. (**Ronkanen et al., 2004**). Khan et al. (**Khan et al., 2016**) developed a constitutive model to predict temperature rise and polarization hysteresis. They obtained good results in polarization hysteresis, but the experimental temperature rise was not well predicted, which the authors attribute to deficient heat transfer control to establish boundary conditions. The factors influencing self-heating were also compiled by Stewart and Cain (**Stewart and Cain, 2014**) and can be summarised as:

- Voltage or electric field
- Excitation frequency
- Temperature

- External load
- Actuator size
- Duty cycle

The two widely cited contributions to overall self-heating are strain losses and dielectric losses (**Stewart and Cain, 2014**), caused respectively by volume changes in the material, and by non-ideal dielectric behaviour respectively. Uchino and Hirose add another contribution solely related to the piezoelectric effect (**Uchino, 2017; Uchino and Hirose, 2001**). Strain losses are caused by internal friction in the actuator. This friction can appear at grain boundaries in polycrystalline materials, or at the interface with electrodes in thin-film deposited materials (**G. Liu et al., 2015**). The work performed by the load to overcome this internal friction is lost as heat. The estimation of dielectric losses is further compounded by the temperature dependance of the piezoelectric's dielectric constant $\epsilon(T)$. For operations close to the resonant frequency of the actuator, strain losses are dominant over dielectric losses. Dielectric losses dominate in case of frequencies far from resonance (**Stewart and Cain, 2014**).

Voltage and electric field may be used interchangeably when referring to the experiment control parameters. Multi-layer actuators are operated in voltage, and the corresponding electric field found in the layers of the actuators is computed as:

$$E = V/d \tag{5.2}$$

with V being the voltage applied and d the layer thickness.

The effect of external loads was investigated by Li et al (**Li et al., 2008**), who concluded that pre-load has a very modest effect on heat production. This load was investigated with a pre-loading spring. Actuator size has been identified as a relevant parameter when studying piezoelectric materials because as cross sectional area increases, the ratio area to volume also increases and the ability to evacuate heat on the edges of the actuator decreases, resulting in higher temperature setpoints.

Heat transfer in this context is described by the classical triad of heat transfer mechanisms: convection, radiation and conduction. However, convection is difficult to predict and, in space applications, mostly absent. The focus of this research is the thermal behaviour of the piezoactuator in vacuum conditions, which severely limits the heat evacuation of the piezoelectric materials and therefore reduces their operational space. In order to reproduce the operating conditions of the actuator, a thermal vacuum (TV) test is proposed, which allows precise control of the heat path by removing natural or forced convection.

5.3. EXPERIMENTAL SETUP.

The goal of the experiment is to measure the self-heating power of piezoelectric actuators in different conditions of frequency, amplitude and thermal environment. Based on information provided by the manufacturer [1], the power dissipated would depend on the frequency and amplitude of actuation, which for limit cases would be in the order of 5 W.

---

[1] Direct communication with engineers at Cedrat Technologies.

Table 5.1: Characteristics of the test actuator, Cedrat Technologies PPA40XL.

Property	Value
Length	60 mm
Cross section	30x30 mm
Capacitance	20 μF
Layer thickness	100 μm
Nominal preload	20 MPa
Temperature range	-40 to 80 °C
Coupling mode	33

The experimental setup's achievable resolution using this technique was not characterised, but the smallest detectable heat fluxes were desired to be in the order of 10 mW. The test items were three PPA40XL actuators manufactured by Cedrat Technologies, although only one was tested inside the vacuum chamber, whilst all three were subjected to additional tests described in **subsection** 5.4.3. Cedrat is one of the companies with flight heritage on these actuators and can comply with the requirements for space qualification and TV operation. The test campaign was carried out at the facilities of the Netherlands Aerospace Centre (NLR) in Marknesse, Netherlands.

5.3.1. DESCRIPTION

The test environment is a vacuum chamber with a shroud which incorporates thermal control, which allows manipulation of the radiative thermal environment of the sample. This is referred to as a TV chamber. A schematic of the system can be found in **Figure** 5.2 The complete setup consists of:

- Test item, a pre-stressed piezoelectric actuator
- Constrained thermal path
- Thermal control and measurement systems
- Piezoelectric control electronics
- Mechanical load simulator

During the test campaign, points of improvement of the setup were noted. Thermal fluxes could be characterised with a resolution in the order of 60 mW as demonstrated during the calibration procedure, which will be discussed in **subsection** 5.4.1. This is likely sufficient for most applications, but processes with very small heat fluxes may not be characterised without modifications. The main characteristics of the test items are summarised in **Table** 5.1.

The thermal control and measurement system is placed around the actuator. It consists of a cold plate cooled with a working fluid at a fixed temperature. The temperature is controlled via a reservoir of gas nitrogen evaporated through a liquid nitrogen pool. The gas flow passes through a heater channel which brings its temperature to the desired level.

In this way, thermal stability of the cold reservoir in the order of 0.05 K was maintained for three hours. Stability was only compromised during operations to re-fill liquid nitrogen tanks for cooling for the gas nitrogen, which was taken into account during testing operations. Due to the good conductive coupling between the actuator and the cold plate, maintaining temperature homogeneity is critical, as a change in the temperatures within the thermal path changes the power needed for steady state operation. Possible improvements to the thermal stability of the setup are liquid coolants, or a two-phase cooling fluid, taking advantage of the larger heat capacity of these options to attenuate local fluctuations in the temperature.

The actuator is placed within an aluminum cup which is coated black to maximise its radiative coupling to the actuator. The cup is wrapped with low emissivity tape and multilayer insulation (MLI) to minimise radiative losses to the environment, which forces all heat produced to go to the cold plate. Guard heaters at the mass at the top of the actuator match the temperature measured at the actuator, so as to net zero heat transfer on that side. The heat leak through the cup to the environment determines the achievable resolution of the setup. A calibration heater is integrated on the actuator to dissipate a controlled amount of heat to characterise the setup, but this is not used during measurements.A schematic of the test setup is shown in **Figure** 5.2. The actuator with copper wire heaters integrated is shown in **Figure** 5.3.

The types of wires needed in this setup are the lead cables for the piezoelectric actuator and calibration heaters to function, and the thermocouple wires. Thermocouples are directly glued to the sample. Wires which go inside of the cup do not require additional insulation, as free heat transfer within the cup is desired. Those which are in thermally insulated parts are covered with reflective tape to minimise radiation losses. The wires are pulled into the cup through a small gap which is also fit with MLI. Since the wires are small compared to the overall size of the setup, heat leakage through them is neglected.

The piezoelectric control electronics consist of a waveform generator controlled by a desktop computer programmed in LabView. Signals produced by the waveform generator are amplified with a Cedrat LA-75C linear piezoamplifier and sent to the actuator. Strain gauges attached to the actuator make it possible to probe the behaviour of the actuator in displacements, which is interesting to control for the motion amplitude when analyzing the data.

Inertial loads are simulated by placing a stainless steel weight, which is thermally isolated but mechanically coupled to the actuator. In prior research, load was indicated to be a factor reducing thermal dissipation for a voltage-controlled actuator (**Ronkanen et al.,** 2004). This however was done without displacement data, and the expectation is that increasing the load would decrease range of motion. In the case of the pre-stressed actuator, a load level is always present on the actuator. The mass simulation added to it allows calculating the sensitivity of heat dissipation to higher inertial loads.

In the TV chamber, frequency and amplitude can be changed without opening the chamber, which allows batches of tests to be carried out in sequence and minimise total time

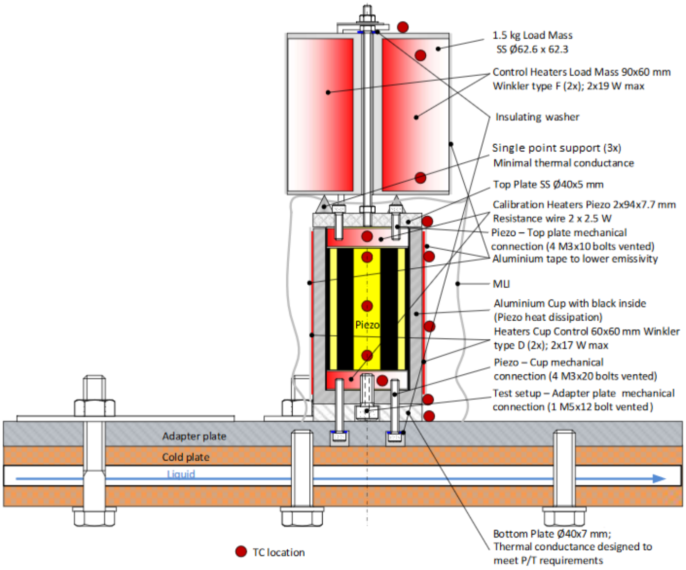

Figure 5.2: Schematic of test setup in thermal vacuum.

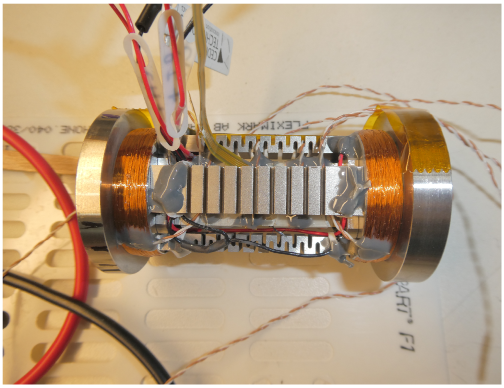

Figure 5.3: Picture of actuator wrapped in copper wire as integrated heater for characterization purposes.

Figure 5.4: Open vacuum chamber and control and measurement equipment.

testing. Controlling the temperature of the cold plate to provide a different temperature setpoint to the actuator can also be done without opening the chamber, but requires manual operation of the pumps. Finally, changing the loads on the actuator or the actuator itself are more intrusive operations which require opening the vacuum chamber. This was avoided because the vacuum chamber requires a complete day to return to operation once the vacuum is lost.

5.3.2. LIMITATIONS OF THE TEST SETUP AND DATA TREATMENT

In order to yield high resolution in power production, the thermal path between the actuator's environment needs to be closed to external losses. In this way, all heat produced by the actuator can be measured. Several well-known practices have been used to limit these heat leaks in the setup, though it is difficult to remove them entirely. Radiative losses from the cup to the shroud are reduced by wrapping the setup in MLI. Another important potential heat leak is the mass simulator on the top of the actuator. This is coupled with the actuator via a screw in the center supported by point contact. The bolted connections between the actuator and the mass are further insulated by the use of thermal washers with poor thermal conduction.

The losses are further reduced by matching the temperatures in their thermal paths. The shroud of the vacuum chamber is set to follow the temperatures of the cup to further minimise heat leak through the cup. The mass is equipped with guard heaters, controlled to match the temperature of the top of the actuator. Note that these two temperatures do not necessarily match in transient due to the mass thermal controller is not tuned to closely follow its target, only to reach it in steady state.

Another major source of error in the measurements is the fluctuation in thermal homogeneity of the adapter plate that acts as interface between the cold sink and the test setup. The temperature of this plate is controlled with the feedback of a thermocouple with another as backup. The latter thermocouple was expected to have a constant offset with the former. However, whilst the controlled thermocouple is stable to within ±20 mK, the spare thermocouple registers slow fluctuations over several hours in the order of ±0.1K, indicating thermal inhomogeneity in this interface. This is significant due to the good conductive coupling between the actuator and the cold plate, as these fluctuations also cause large fluctuations (order of hundreds of miliwatts) in the power measured. A better iteration of this test setup would solve this problem by adding more thermocouples in this critical heat path and tuning the control to keep all of them equally stable. The current iteration of the test setup is not capable of fully characterising this behaviour, which introduces measurement uncertainty.

During the test campaign, points of improvement of the setup were noted. Thermal fluxes could be detected with a resolution in the order of 60 mW as demonstrated during the calibration procedure, but these results cannot be trusted to be accurate if the stability of the cold plate is compromised. This resolution is likely sufficient for most applications, but processes with very small heat fluxes (order of 10 mW) may not be characterised without modifications. Note that temperature rise can be observed without noticeable increase in observed power dissipation with the instrumentation.

5.4. RESULTS

5.4.1. CALIBRATION

The objective of the calibration runs is characterising the measurement procedure to establish what corrections are needed to the raw data. A known amount of power is dissipated in simulator heaters attached to the hubs of the pre-loading structure of the piezoactuator. The controler keeps the temperature of the control thermocouple unaltered by reducing the heat it releases into the setup. Since all the heat fluxes are known in this case, a discrepancy between the measured and the introduced powers indicates a heat leak or another measurement problem.

Data from this calibration run show that the setup underestimates power introduced via this method due to heat leaks. The primary heat leaks causing this were described in **subsection** 5.3.2. The largest influence on the readings was the instability of the cold plate. The trend of this instability over a day of testing is diminishing temperature with time each day, although the trend reverses by the end of a test period, corresponding also to an decrease in power to keep temperatures stable. This confirms that the power measurement swings are related to this phenomenon.

The typical steady-state error of the temperature control is in the order of 0.05 K. The heat leak through the MLI was estimated to be negligible compared to the two main heat leaks, which are the leaks to the mass and the gap between the mass and the cup. The final

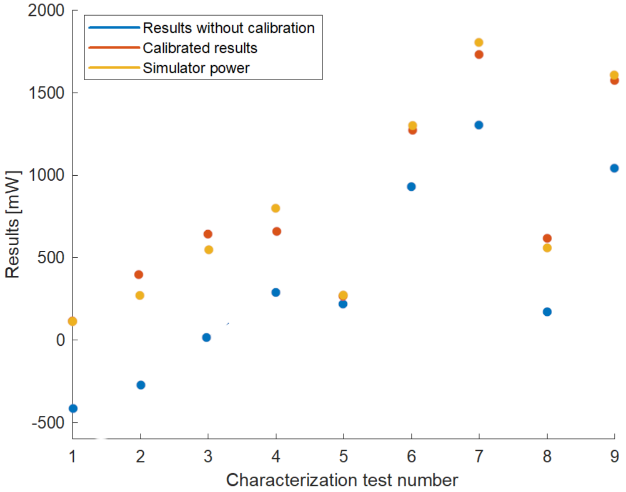

Figure 5.5: Uncorrected results of the setup characterization runs. The x axis only shows the test number, simulator power in each test is decided by the operator.

heat leak is the remnant transient, which can be estimated knowing the mass and materials of the setup per experiment.

Knowing the temperatures of the cold sink, the mass and the shroud, a calibration equation is proposed to turn raw power measurement data into corrected power measurements:

$$P_{Cor} = P_{Raw} + C_{Sink}\Delta T_{Sink} + C_{Mass}\Delta T_{Mass} + C'_{Trans}\frac{\Delta T_{ACT}}{\Delta t} \tag{5.3}$$

In equation 5.3, C_{Sink} and C_{Sink} are the conductive couplings to the sink and mass, and C'_{Trans} is the total heat capacity of the actuator. These three constants determine the correction applied as a function of the respective temperature or temperature variation in time. This method, applied to the calibration runs, shows that once these heat leaks are corrected, the setup produces good measurements of heat. However, later tests with the piezoactuators active at low electric field magnitudes show that measurements below the 150 mW threshold are not reliable. **Figure** 5.5 shows the uncorrected and corrected results when dissipating a known quantity of heat into the system. The constants in equation 5.3 were found by minimising the relative error between the corrected measurement and the known quantities of heat dissipated in the different tests.

The same procedure was followed with the tests performed in cold conditions. These constants are sensitive to large temperature changes, because thermal expansion of the interfaces in the setup alters their conductive properties (**Cooper et al.,** 1969). Therefore, correction constants need to be found for each temperature setpoint with this technique. The temperature control of the interface, however, guarantees that given a global setpoint, the interface is not affected by the heat generation of the process being measured. **Table** 5.2 shows the values of the correction factors applied in the two temperature setpoints.

Table 5.2: Experimentally determined correction factors for the two TV test conditions.

	C_Sink [mW/K]	C_Mass [mW/K]	C'_Transient [mW/sK]
T_Sink = $0^{o}C$	2479	383.8	136.4
T_Sink = $-40^{o}C$	2787	212.1	348.0

5.4.2. POWER MEASUREMENT.

The real power measurements were carried out in the TV chamber. The principle of measurement was proven to work, but its resolving power is limited at low power dissipations in the order of 500 mW. At high dissipation, the boundary condition controls and the vacuum limit the amount of heat that can be effectively evacuated from the PZT stack. This limitation in heat flow causes a rise in the internal temperature of the piezoelectric stack in the actuator at high power dissipation. Tests were interrupted by a safety trigger when temperatures rose to 80°C. This limits the space of frequency and amplitude that can be probed with this setup. The limits to this space were found via trial and error. All tests were performed with sinusoidal excitation. The defining characteristics of the inputs used are summarised in **Table** 5.3.

Table 5.3: Input characteristics for the different tests.

Actuator 1 TV	Frequency [Hz]	Amplitude [V]
	50	42.5
	20	85
	5	170
	100	42.5
	150	42.5
	50	85
	20	170
	100	85
	150	85
	20	127.5
	40	170
	190	21.5
	190	21.5

Figures 5.6 and 5.7 show the corrected measurements from the piezoelectric actuators as a function of frequency and amplitude respectively. The error bars represent the magnitude of the correction factors applied to the setup as a measure of uncertainty. Note that the error bars may reach negative values, but this would not make physical sense. The results show that for small excitation amplitudes, thermal dissipation cannot be detected with this setup. The results also show the expected result that increasing frequency or amplitude of

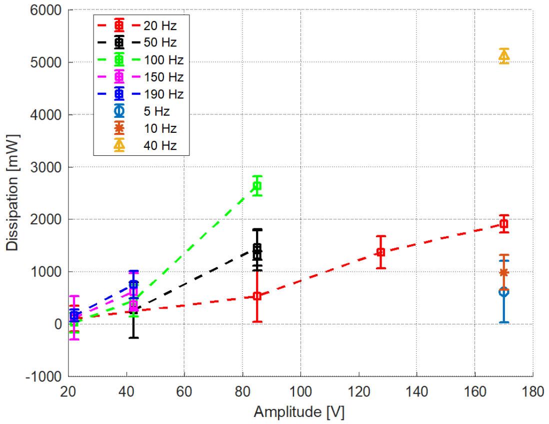

Figure 5.6: Measured thermal dissipation as a function of amplitude for different excitation frequencies.

the actuator increases heat dissipation. Dependency with frequency appears linear, and quadratic with voltage amplitude. Of special interest is the maximum dissipation achieved at maximum amplitude is reached at 40 Hz, which would be an immediate practical limitation to the operation of a system in order to avoid actuator thermal failure, assuming that the thermal environment in the test in the test is representative of the operational environment.

In this setup, the amplifier output was independently verified to be according to manufacturer specification. However, there was no way of recording those values as the tests were progressing. However, they could be recorded in the tests with actuators outside of the vacuum, as described in the following section.

The cold plate and shroud were brought to a cold setpoint at -40ºC. The test was repeated for a reduced set of actuation parameters. The expectation was that dissipation at colder temperature setpoints would be significantly smaller than at ambient because such behaviour has been reported in the literature. However, in this study there is no significant evidence as to the effect of temperature in the power dissipation in this temperature range. **Table** 5.4 shows final results for both temperature settings.

Table 5.4: Comparison of results at 0ºC and -40ºC for different settings.

Test parameters	0 ºC setpoint [mW]	-40 ºC setpoint [mW]
50 Hz / 85 V	1461.4 / 1311 / 1408.6	1340
100 Hz / 85 V	2639.7	2742.3
20 Hz / 170 V	1909.9	2068.8

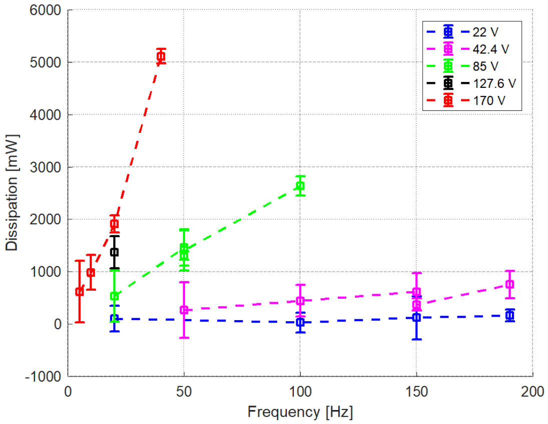

Figure 5.7: Measured thermal dissipation as a function of frequency for different excitation amplitudes.

5.4.3. TRANSIENT OPEN AIR TEST.

An additional test was performed outside of the vacuum chamber with actuators of the same model and manufacturer. The experimental procedure presented herein is difficult to set up and to run, so it was not done for the several actuators. In order to have confidence that the actuators behave in similar fashion, a simpler setup with no vacuum chamber was prepared and executed on the three actuators available. A glass cover isolates the actuator stack from air currents in the lab. The cold plate is kept at 15ºC via a cooling loop of glycol and water. This setup can be seen in **Figure** 5.8.

In this test, the output voltage of the amplifier and the voltage prior to a shunt resistor are recorded by an oscilloscope. The instantaneous power consumed by the actuator can be modeled as:

$$P(t) = (V_{amp}(t) - V_{shunt}(t)) * V_{shunt}(t)/R_{shunt} \tag{5.4}$$

where V_{amp} and V_{shunt} are the voltages at the amplifier output and across the shunt resistor and R_{shunt} is the resistance of the shunt. These signals were multiplied in time domain to obtain instantaneous power and then averaged over 5 cycles to obtain the power reading. The measured signal $V_{amp}(t)$ includes a DC offset as a result of the amplifier not delivering a zero-average sine wave. This DC component is filtered by the actuator due to its capacitive nature of the actuator, which is seen on DC as an open circuit. Therefore, no current can flow on DC and no power is consumed. More precisely, in DC conditions, there can be some current leakage through any real material, which can be seen in the models presented by Paganelli et al (**Paganelli et al.,** 2010). In this application, however, this effect was too small to be detected. Other models, such as proposed by Zhang et al. do not consider this potential leakage in DC at all (**Zhang et al.,** 2015).

Table 5.5 shows the frequency and amplitudes use for testing on this setup. The results of real power consumption are shown in **Figure** 5.9. These values show agreement within the order of 10% of the output. with the results presented in the TV test as shown in **Figure**

Figure 5.8: Setup outside of vacuum.

Actuator 1/2/3 OOV	Frequency [Hz]	Amplitude [V]
	50	42.5
	20	85
	5	170
	100	42.5
	150	42.5
	50	85
	20	170
	100	85
	150	85
	40	170

Table 5.5: Characteristics of the sine waves used in out of vacuum (OOV) tests.

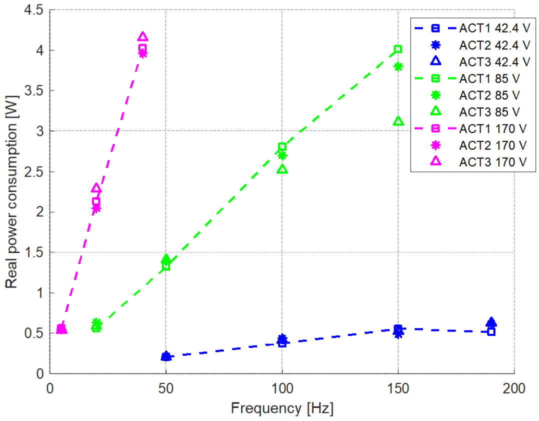

Figure 5.9: Power consumption results of the different actuators tested outside of the vacuum.

5.10. A notable exception is the maximum dissipation case in both, which is a setting of 40 Hz at 170 V. In this case, dissipation directly measured is significantly larger in TV. This is likely a result of the higher actuator temperature reached in TV, as it is not possible to evacuate as much heat as in the presence of air. This effect was not present at cold temperatures, but it is, as previously mentioned, well established in literature.

5.5. CONCLUSIONS

The described measurement method for heat dissipation is capable of producing a dissipation profile for piezoelectric actuators or other types of heat generating low power test items. The measurement principle has been demonstrated and described, but several challenges remain to improve its resolution, and more importantly its repeatability. Measurements from this method have been used to compare dissipation in different temperature setpoints, and can be adapted to better reflect the boundary conditions encountered in real operations. The method's current shortcomings have been analysed and mitigation strategies have been proposed for future iterations. The results are in line with the intuitive expectation that higher actuation frequency and amplitude increases the total losses, and suggest limitations to the operation based on the self-heating of the actuators.

5.6. FUTURE WORK

The technique described in this chapter was novel and there are several changes which can further improve accuracy and repeatability of direct power measurements for piezoactuators and other low-power electrical components. These were deemed unnecessary during the design of the experiment, which in hindsight should have been part of it. Quantitative measurements of current system repeatability were not executed, which was a flaw in the test protocol, but repeatability is expected to improve with the proposed changes.

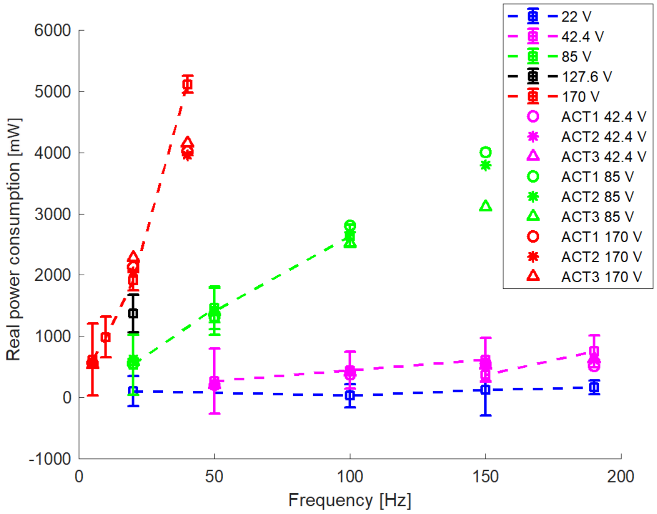

Figure 5.10: Lost power results from the tests carried out inside and outside vacuum. Datapoints joined with dashed lines represent TV tests, the rest are results from OOV tests.

One challenge in the data analysis of the setting was the erratic behaviour of the main thermal path through the adapter plate. Even though stability was better than 0.1 K/h, this is not sufficient to resolve low power dissipation without correcting for thermal drift of the cold plate. In addition, the fact that only two thermocouples monitored this thermal path meant there could be unexplored contact dynamics at the interface which cannot be accounted for with the current sensing equipment. In order to address this problem, a more thermally conductive material could be used to construct this part of the setup, with the goal of reducing zonal differences. In addition, more temperature sensors placed at the base of the cup are needed to fully characterise the complex bolted interface and design the control strategy accordingly. In this work, only two thermocouples were used, and only one of them gave relevant information about the temperature fluctuations at the base.

Thermal stability can also be improved by changing cooling technology. Gas nitrogen is safe to use in the vacuum chamber even if a leak occurs. Other possibilities which could perform better are a glycol bath, or more adequately, a two-phase cooling loop such as described by van Gerner et al. (**van Gerner et al., 2017**). However these are more complex and less safe alternatives in case of leakage in the vacuum chamber.

BIBLIOGRAPHY

Abdul Satar, M. H., Murad, A. F., & Ahmad Mazlan, A. Z. (2020). Characterization of piezoelectric patch material with hysteresis, saturation, creep, and vibration nonlinearity effects and its application to the active vibration suppression for cantilever beam. *JVC/Journal of Vibration and Control*, (May), 1–14. https://doi.org/10.1177/1077546320980571

Blackshire, J. L., Martin, S., & Cooney, A. (2006). Characterization and modeling of bonded piezoelectric sensor performance and durability in simulated aircraft environments. *Proceedings of the 3rd European Workshop - Structural Health Monitoring 2006*, *1694*(2006), 283–289.

Cooper, M., Mikic, B., & Yovanovich, M. (1969). Thermal contact conductance. *International Journal of Heat and Mass Transfer*, *12*(3), 279–300. https://doi.org/10.1016/0017-9310(69)90011-8

Gao, X., Yang, J., Wu, J., Xin, X., Li, Z., Yuan, X., Shen, X., & Dong, S. (2020). Piezoelectric Actuators and Motors: Materials, Designs, and Applications. *Advanced Materials Technologies*, *5*(1), 1–26. https://doi.org/10.1002/admt.201900716

Islam, M., Seethaler, R., & Mumford, D. (2011). Real time temperature measurement for multilayered piezoelectric stack actuators. *Canadian Conference on Electrical and Computer Engineering*, 001194–001197. https://doi.org/10.1109/CCECE.2011.6030651

Khan, K. A., Muliana, A. H., Atitallah, H. B., & Ounaies, Z. (2016). Time-dependent and energy dissipation effects on the electro-mechanical response of PZTs. *Mechanics of Materials*, *102*, 74–89. https://doi.org/10.1016/j.mechmat.2016.08.001

Li, F. X., Rajapakse, R. K., Mumford, D., & Gadala, M. (2008). Quasi-static thermo-electro-mechanical behaviour of piezoelectric stack actuators. *Smart Materials and Structures*, *17*(1). https://doi.org/10.1088/0964-1726/17/1/015049

Liu, G., Zhang, S., Jiang, W., & Cao, W. (2015). Losses in ferroelectric materials. *Materials Science and Engineering R: Reports*, *89*, 1–48. https://doi.org/10.1016/j.mser.2015.01.002

Liu, X., Wang, G., Li, M., Chen, J., Dong, S., & Hu, Z. (2015). Development of hard high-temperature piezoelectric ceramics for actuator applications. *Journal of Materials Science: Materials in Electronics*, *26*(12), 9350–9354. https://doi.org/10.1007/s10854-015-3075-3

Lu, X., Wang, L., Jin, L., Hu, Q., Tian, Y., Hou, L., Yu, K., Zhang, L., Wei, X., Yan, Y., & Liu, G. (2018). Ultra-low hysteresis electrostrictive strain with high thermal stability in Bi(Li0.5Nb0.5)O3-modified BaTiO3 lead-free ferroelectrics. *Journal of Alloys and Compounds*, *753*, 558–565. https://doi.org/10.1016/j.jallcom.2018.04.257

Minase, J., Lu, T. F., Cazzolato, B., & Grainger, S. (2010). A review, supported by experimental results, of voltage, charge and capacitor insertion method for driving piezoelectric actuators. *Precision Engineering*, *34*(4), 692–700. https://doi.org/10.1016/j.precisioneng.2010.03.006

Mohith, S., Upadhya, A. R., Navin, K. P., Kulkarni, S. M., & Rao, M. (2021). Recent trends in piezoelectric actuators for precision motion and their applications: a review. *Smart Materials and Structures*, *30*(1). https://doi.org/10.1088/1361-665X/abc6b9

Paganelli, R. P., Romani, A., Golfarelli, A., Magi, M., Sangiorgi, E., & Tartagni, M. (2010). Modeling and characterization of piezoelectric transducers by means of scattering parameters. Part I: Theory. *Sensors and Actuators, A: Physical*, *160*(1-2), 9–18. https://doi.org/10.1016/j.sna.2010.03.006

Pritchard, J., Ramesh, R., & Bowen, C. R. (2004). Time-temperature profiles of multi-layer actuators. *Sensors and Actuators, A: Physical*, *115*(1), 140–145. https://doi.org/10.1016/j.sna.2004.04.019

Quattrocchi, A., Freni, F., & Montanini, R. (2018). Self-heat generation of embedded piezoceramic patches used for fabrication of smart materials. *Sensors and Actuators, A: Physical*, *280*, 513–520. https://doi.org/10.1016/j.sna.2018.08.022

Ronkanen, P., Kallio, P., Vilkko, M., & Koivo, H. N. (2004). Self heating of piezoelectric actuators: Measurement and compensation. *Proceedings of the 2004 International Symposium on Micro-NanoMechatronics and Human Science*, 313–318. https://doi.org/10.1109/mhs.2004.1421324

Sabarianand, D. V., Karthikeyan, P., & Muthuramalingam, T. (2020). A review on control strategies for compensation of hysteresis and creep on piezoelectric actuators based micro systems. https://doi.org/10.1016/j.ymssp.2020.106634

Senousy, M. S., Rajapakse, R. K., Mumford, D., & Gadala, M. S. (2009). Self-heat generation in piezoelectric stack actuators used in fuel injectors. *Smart Materials and Structures*, *18*(4). https://doi.org/10.1088/0964-1726/18/4/045008

Somwan, S., Limpichaipanit, A., & Ngamjarurojana, A. (2015). Effect of temperature on loss mechanism of 0.7PMN–0.3PZT ceramics. *Sensors and Actuators, A: Physical*, *236*(1), 19–24. https://doi.org/http://dx.doi.org/10.1016/j.sna.2015.10.029

Stewart, M., & Cain, M. G. (2014). Measurement and Modelling of Self-Heating in Piezoelectric Materials and Devices. In M. G. Cain (Ed.), *Characterisation of ferroelectric bulk materials and thin films*. Springer. https://doi.org/10.1007/978-1-4020-9311-1

Uchino, K. (2017). High-Power Piezoelectrics and Loss Mechanisms. *Advanced piezoelectric materials - science and technology (2nd edition)* (2nd).

Uchino, K., & Hirose, S. (2001). Loss Mechanisms in Piezoelectrics : How t o. *IEEE Transactions on Ultrasonics*, *48*(1), 307–321.

van Gerner, H. J., Bolder, R., & van Es, J. (2017). Transient modelling of pumped two-phase cooling systems: Comparison between experiment and simulation. *47th International Conference on Environmental Systems*, (July), 1–15. https://ttu-ir.tdl.org/handle/2346/72881

Waanders, J. W. (1991). *Piezoelectric ceramics: Properties and Applications*. N. V. Philips' Gloeilampenfabrieken.

Weaver, P. M., Stevenson, T., Quast, T., Bartl, G., Schmitz-Kempen, T., Woolliams, P., Blumfield, A., Stewart, M., & Cain, M. G. (2015). High temperature measurement and characterisation of piezoelectric properties. *Journal of Materials Science: Materials in Electronics*, *26*(12), 9268–9278. https://doi.org/10.1007/s10854-015-3285-8

Yoo, J., Im, J., & Im, I. (2020). Physical Characteristics of (1 - x)[(Na,K)(Nb,Sb)O3]–(Bi,Na)ZrO3–xBaZrO3 Ceramics for Piezoelectric Actuator. *Transactions on Electrical and Electronic Materials*, *21*(5), 477–481. https://doi.org/10.1007/s42341-020-00225-9

Yu, Y., Naganathan, N., & Dukkipati, R. (2002). Preisach modeling of hysteresis for piezoceramic actuator system. *Mechanism and Machine Theory*, *37*(1), 49–59. https://doi.org/10.1016/S0094-114X(01)00065-9

Zhang, Y., Lu, T. F., & Peng, Y. (2015). Three-port equivalent circuit of multi-layer piezoelectric stack. *Sensors and Actuators, A: Physical*, *236*, 92–97. https://doi.org/10.1016/j.sna.2015.10.033

Zheng, J., Takahashi, S., Yoshikawa, S., & Uchino, K. (1996). Heat Generation in Multilayer Piezoelectric Actuators. *Journal of the American Ceramic Society*, *79*(12), 3193–98. https://doi.org/10.1111/j.1151-2916.1996.tb08095.x

6

CONCLUSIONS AND RECOMMENDATIONS

In this thesis, different aspects of the mechanical stability of space telescopes have been investigated. The general challenge of stability of the optical elements in a deployable telescope was studied first in a literature study. The problem was then restricted to the thermoelastic challenges of deployable telescopes. In this chapter, the contributions and innovations of this research in studying the aspect of general stability, and more precisely to thermoelastic stability, will be summarised, followed by an outlook on future work.

6.1. SUMMARY

The summary of this doctoral thesis is provided by answering the research questions in the following paragraphs.

> **RQ1:** What are the characteristics of a deployable structure which can meet the stability, accuracy, and integrity requirements needed for space-based optical performance?

This research question was answered mainly through a literature study. **Chapter 2** is devoted to a review of thermal and mechanical engineering challenges which need to be overcome in order to have a working system. The systems that have been proposed in the literature have also been reviewed in order to establish how researchers were tackling these issues. The most informative and exhaustive information can be found in literature on the James Webb Space Telescope and its prior developments as the Next Generation Space Telescope. From a top level perspective, a divide can be found between segmented aperture primary mirrors, with more stringent wavefront error requirements in exchange for increased aperture, and deployable secondary mirrors intended to increase the focal length of the system. All system designs include some form of active optics mechanism in order to bridge the gap between the repeatability of the deployment mechanism and the required alignment between optical elements, which highlights the importance of active optics mechanisms.

A lot of attention in the literature specifically about deployable telescopes is focused on the study of microdynamics. In **Chapter 2**, an effort was made to characterise what the community may understand as microdynamics, but it remains a vaguely defined term. However, many papers pointed to hysteretic behaviour of mechanical interfaces as the cause of several phenomena which affect the repeatability and stability of precision deployable structures. In order to avoid this, compliant mechanisms were proposed as potentially beneficial. Hysteresis in a compliance-assisted rolling hinge was investigated in (**Villalba et al., 2019**). Despite the importance of the sunshield and thermal control systems in the JWST's system design, thermoelastic behaviour is not widely discussed in literature regarding similar systems. In this respect, a distinction between the steady thermal environment of deep space observatories and the dynamic thermal environment of Earth Observation missions with deployable optics must be made.

From this literature survey, it was found that there were three key technologies which drive the technology development efforts in the mechanical engineering of deployable optics: Precision deployment and actuation mechanisms, including active optics, vibration and thermal control and isolation, and lightweight mirrors. Technology of lightweight mirrors is tied to the use of novel materials such as Berillyum O-30 in cryogenic telescopes. Other advancements in lightweight mirror technology include the use of hybrid composite mirrors (**Catanzaro et al., 2000**) with thin layers of glass or ceramic for better polishing properties. Finally, large active mirrors (**Hickey et al., 2010**) have been proposed for both secondary mirrors of large observatories or primary mirrors in modular telescopes.

> **RQ2:** What are the characteristics of an active optics mechanism capable of aligning the segmented mirrors of a deployable telescope?

Chapter 3 focuses on the methods for the design of an active optics mechanism. As a summary, active optics mechanisms for space application need to be comprehensive, precise and resilient. Here, comprehensive merely refers to the ability to constrain or actuate all degrees of freedom of the end effector, as required. The Freedom and Constraint Topologies method easily characterises all the possible geometric arrangements of constraints and actuators which provide the desired actuated and fixed degrees of freedom, derived directly from optical sensitivity analysis. Kinematic performance of the mechanism, which constitutes the case study in this thesis, was assessed with both analytical linearised inverse kinematics, and with extended finite element analysis. Both of these analysis resulted in satisfactory positioning of the end effector in simulations.

In terms of achieving precision, the methods proposed here borrow from the contributions to the wider field of precision engineering and rely on prior work on the design of mechanisms with compliant elements. Such mechanisms are articulated by flexural elements because of the advantages they present and which have been reviewed in **Chapter 2**. These advantages can be summarised as reduced hysteresis, high repeatability, lack of lubrication and reduced part count. In addition to these characteristics, active optics mechanisms are designed to be athermal in as many directions of motion as possible. If this cannot be achieved, the mechanism needs to be able to compensate for the residual thermoelastic deformations as its temperature changes, which detracts from available actuation for other disturbances. In case thermoelastic deformation is not taken into account early in the design, the design complexity may be shifted to the design of a thermal control system with stringent requirements. In order to achieve high precision, literature very often refers to the principle of exact constraint design to achieve repeatable mechanisms without the need of tight manufacturing tolerances. However, this principle can be broken in case it conflicts with some other design consideration, such as in the athermalization or stiffness properties of the final design. Overconstraint is broadly undesirable, but can be offset with some techniques like monolithic manufacturing of redundant constraints, which was implemented in this research. Other techniques which allow high precision in overconstrained systems are the use of symmetric designs, elastic averaging, or very precise manufacturing. The latter of these is not desired, because of the high costs involved.

Finally, resilience of the mechanism refers to its ability to withstand launch loads and continue operating normally. In this thesis, the survival of the mechanism against launch loads has been assessed through computational models. Classical structural design theory highlights that the major failure mechanisms are stresses above the yield strength of the material, resonance of the structure with the launcher loads, and buckling of slender elements, such as wire or blade flexures. In order to mitigate these failure mechanisms, materials with high specific strength and high specific stiffness are beneficial. In addition to these classical failure mechanisms, **Chapter 2** also contains references to the phenomenon of microplasticity, which consists in small permanent deformations to the structure well below the yield stress. Avoiding microplasticity entirely is likely to lead to overly massive elements, so its effects should be included in sensitivity analyses. However, this was not done in this thesis.

The Analytical Hierarchy Process (AHP) has been applied to the choice of materials, actuator technology, and final concepts. Though AHP is a trade-off method which uses relative comparisons between the different options and the different trade-off criteria, a modification was proposed here using a normalization of objective data in the cases where this was possible. This modification was applied to the material selection process. In the case of actuator technology, the trade-off gave parallel pre-stressed piezoelectric actuators as the most appropriate concept in this case, although this is not a conclusion that can be generalised.

Thermoelastic modelling was performed on the resulting mechanism in order to find the extent to which athermalisation could be implemented and eliminate temperature differences as a factor in mechanism repeatability. Thermal modelling of the mechanism in simulated orbital conditions show that temperature gradients are very significant. The most rudimentary approach to athermalization of mechanisms understands that the temperature across the mechanism changes, but it remains homogeneous. In this research, instead, a model of the inhomogeneous temperature field was used as the input for the thermoelastic model. This should offer a more realistic approximation to the performance of athermalization strategies.

> **RQ3:** What are the characteristics of the critical components of the DST, as derived from in-the-loop hardware testing?

Two main components were experimentally examined in this thesis: a prototype of the active optics mechanical frame, and a parallel pre-stressed piezoelectric actuator. These are understood to be critical due to the importance of active optics in mitigating disturbances to the positioning of the optical elements. More components could be classified as critical in achieving a working system, such as the deployment mechanism or the deployable baffle, but their detailed design and testing are not the focus of this dissertation.

The active optics mechanism prototype was tested with the intention of validating the models used in its development experimentally. **Chapter 4** details the verification and validation approach followed for these models, including the experimental methods developed for the active optics mechanism. Before manufacturing, the prototype was first 3D-printed as a check that it could be integrated. The final test item was subjected to dynamic loads with the application of a modal hammer. The modal characteristics were recorded with tri-axial accelerometers. This showed that the flexibility in the intermediate bodies of the mechanism drastically lowered the mechanism's first eigenfrequency compared to prediction. The first eigenfrequency was found to be at 27 Hz, far below the 100 Hz requirement initially set and the 198 Hz prediction by the Spacar model. The main interest, however, was comparing thermoelastic model results to experimental thermal deformations.

A method for investigating the displacement of the mechanism's end effector under thermal load has been proposed, developed and implemented. The results do not permit validation of the initial models, but do show complex behaviour of the mechanism due to an inhomogeneous temperature field. Overall, increased temperature led to an elevation of the end effector, as expected, but the opposing thermal expansion mechanisms also made the system decrease its overall elevation in some stages of the thermal transient.

One of the main difficulties of using an experimental setup for model validation is the need for verification and validation of the test methodology, and the test setup. The main problem in the test methodology described in **Chapter 4** is that, given non-compliance, the inability to decompose the different thermal expansion dynamics present makes it impossible to diagnose what the problem is, and whether it pertains to the test setup or to the model. In addition, a clear definition of relative error between the model output and the experimental results is a severe limitation in assessing model accuracy. These challenges would have likely been more apparent with a stepwise approach in which systems of increasing complexity were tested and the methodology could be developed from a more solid understanding of both the system thermoelastic response and the testing equipment.

Self-heating of a parallel pre-stressed actuator has also been experimentally characterised. The results show that for high frequency and stroke of actuation, thermal emissions of these actuators can become a significant disturbance to the thermal state of a mechanism frame. They also highlight the difficulty in removing excess heat in an environment with no convection, as in space. The methodology proposed in testing of self heating can be used to define operational boundaries of frequency and stroke in a similar environment to real space conditions.

6.2. INNOVATIONS AND CONTRIBUTIONS

Review of thermal and mechanical engineering challenges and technologies relevant to deployable optics.

A review of the specific mechanical and thermal characteristics of deployable optics has been presented in **Chapter 2** to supplement previous work describing conventional space optics structures. The projects present in literature were also examined with a special interest in their mechanical characteristics. From this information, general enabling technologies were identified and described.

Integrated design and trade-off methodologies for the design of active optics mechanisms.

Techniques for design of flexural mechanisms have been reviewed and integrated for active optics mechanisms in the context of deployable space telescopes. The methods include the selection of flexural constraint systems, material and actuator selection, and trade-off methods combining engineering judgement with objective data.

Implementation and application of simple thermoelastic models in early stage design.

In the opinion of the author, insufficient attention is given in literature to the thermoelastic characteristics of complex mechanisms in space applications. The modelling workflow proposed here to support design efforts includes the modelling of realistic thermal situations and its influence in the final behaviour of the mechanism.

Systematic approach to model verification and validation in thermoelastic modelling of complex mechanism.

Model verification and validation has been designed and executed. The main risks to model accuracy have been identified and, to the extent of the possibilities, mitigated. The ones which could not be mitigated have at least been identified, but more work is required to arrive at models which can reliably predict thermoelastic deformations.

Experimental methodology for thermoelastic testing.

A combined thermoelastic experimental method has been developed and implemented. The method in its current form cannot validate the computational models previously presented, but a critique of the method and suggested improvements have also been examined in **Chapter** 4.

New experimental characterisation method of self-heating in piezoactuators.

A method for experimental evaluation of piezoelectric self-heating in thermally controlled vacuum has been presented in **Chapter** 5. To the knowledge of the author, no similar method is present in literature. This method can be extended to other electrical appliances. The results produce direct dissipated power measurements as opposed to inferring it from a curve fit to the temperature measurements, as is commonly done.

6.3. SUGGESTIONS OF FUTURE WORK

Deployable optics concepts rely on a combination of many technological advances, only a subset of which has been studied in depth in this thesis. **Chapter** 2 already points at several technologies which help enable these systems. More important at this stage is to examine what future work is needed on the specific research lines explored in depth here.

Characterisation of simpler sub-assemblies under thermoelastic loading.

In retrospect, the approach of trying to validate the proposed computational models with experimental results on the complex flexure mechanism proposed for the primary mirror active optics was excessively ambitious. Both Ansys and Spacar have been shown in separate cases to be able to reproduce the elementary results of thermal expansion of a simple beam. In light of this, a step-wise approach to thermoelastic testing of assemblies of increasing complexity might help elucidate the opposing and varied dynamics governing the position of the end effector of the mechanism as a function of the inhomogeneous temperature field. In addition, a better approach to creating homogeneous temperature field may also be useful in assessing the robustness of athermalization to the temperature gradients, as the final thermal environment in operation may not be well characterised.

Decomposition of opposing thermal expansion mechanisms in complex assemblies.

One of the main challenges in the proposed method of thermoelastic testing is the lack of information which can help distinguish the underlying origin of the features of the final output. It is possible that some model decomposition mathematical techniques can be used in this case, such as thermal modal analysis or proper orthogonal decomposition. However, even if such a decomposition is possible, the experimental component of this research program would benefit from additional information collected. In particular, the use of higher resolution thermal characterisation through the use of a thermal infrared camera instead of an array of temperature sensors, and the use of strain gauges with adequate temperature correction would yield more information about the interaction between thermal deformation and the mechanism's kinematics.

Possible shift away from pure physics-based modelling in design in favour of a data-driven approach.

In this thesis, design methods have been supported with physics-based modelling. The general idea is that when these models achieve correct predictions of the behaviour of the system, the system parameters can be tuned to achieve compliance with requirements. In particular, this is true of the actuation stroke of the active optics mechanism, where budgeting of the total actuator stroke may be used to address different disturbance sources. However, literature on machining centres concerned with thermal loads has circumvented this partially through the use of data-driven control. It is possible that within some rough order of magnitude bounds, a mechanism prototype can be integrated and a more general data collection can be used to automatically allocate the actuation stroke without detailed knowledge of the underlying physical mechanisms.

Thermal model verification and validation of the in-orbit environment.

It is clear that the thermal environment is very important to the actuation system. It has been shown that, at least in some cases, detailed knowledge of the temperature field is required for an adequate sizing of the athermalization features which can be added to a baseline design. However, numerical simulation of the complete system has large margins of error which have not been thoroughly explored here. Two main activities may reduce this knowledge gap: Experimental characterisation of the thermal environment experienced by the mechanism in orbit, and thermal sensitivity analysis which ensures final compliance under the uncertain loads.

Definition of operational boundaries of operation in piezoelectric actuators.

Research into actuator self-heating shows that this can be a problem not only due to thermal runaway effects destroying the actuator, but also due to large thermal dissipation to other parts o the actuation system. This suggests that there are physical limits to the velocity at which the mirror pose may be changed to compensate for disturbances and therefore to the possible bandwidth of the corrections, even if the driving control algorithms can be ran at very high frequency. To the knowledge of the author, this is not currently the main limitation in active optics systems, but it may become relevant if new actuation commands are issued at high frequency.

Actuator integration on the frame.

Whilst the actuator and the frame can be, in principle, readily integrated using the bolted interfaces already used with the dummies, there may be additional technical issues arising from the integration of the two. Examples of these issues would be the cabling introducing additional unforeseen stiffness, or the actuation not being aligned with the expected axis due to manufacturing defects in the preloading frame. In addition, the measurement and control system still needs to be designed and implemented.

BIBLIOGRAPHY

Catanzaro, B. E., Keane, D., Connell, S. J., Baiocchi, D., Burge, J. H., Maji, A. K., & Powers, M. K. (2000). *UltraLITE glass/composite hybrid mirror* (tech. rep. July 2000). https://doi.org/10.1117/12.394003

Hickey, G., Barbee, T., Ealey, M., & Redding, D. (2010). Actuated hybrid mirrors for space telescopes. *Space Telescopes and Instrumentation 2010: Optical, Infrared, and Millimeter Wave*, *7731*(August 2010), 773120. https://doi.org/10.1117/12.858217

Villalba, V., Leegwater, S., & Kuiper, H. (2019). CORE Hinge Testing Phase results of the Delft Deployable Space Telescope. *33rd Annual AIAA/USU Conference on Small Satellites*.

CURRICULUM VITÆ

Víctor Manuel VILLALBA CORBACHO

09-12-1993	Born in Málaga, Spain.

EDUCATION

2011-2015	Undergraduate study in Aerospace Engineering Higher Technical School of Engineering, University of Seville
2015-2017	MSc Space Science and Technology Luleå University of Technology and Cranfield University
2017-2022	PhD. Space Engineering Delft University of Technology *Thesis:* Thermoelastic Stability of Deployable Space Telescopes *Promotor:* dr. ir. H. Kuiper

LIST OF PUBLICATIONS

THIS THESIS

1. **V. Villalba Corbacho, H. Kuiper, E. Gill**, *Review on thermal and mechanical challenges in the development of deployable space optics*, Journal of Astronomical Telescopes, Instruments, and Systems, Vol. 6, Issue 1, 010902. .

2. **V. Villalba Corbacho, H. Kuiper, E. Gill**, *Direct self-heating power observations in pre-stressed piezoelectric actuators*, Sensors and Actuators A: Physical Volume 333, 1 January 2022, 113276.

3. **D. Dolkens, H. Kuiper, V. Villalba Corbacho**, *The deployable telescope: a cutting-edge solution for high spatial and temporal resolved Earth observation*, Advanced Optical Technologies Volume 7 Issue 6.

4. **V. Villalba Corbacho, S. Leegwater, H. Kuiper**, *CORE Hinge Testing Phase results of the Delft Deployable Space Telescope*, Proceedings of the 33rd Annual AIAA/USU Conference on Small Satellites.

OTHER WORK

1. **S. Jiménez Alfaro,V. Villalba Corbacho, V. Mantič**, *Singular elastic solutions in corners with spring boundary conditions under anti-plane shear*, International Journal of Fracture volume 223, pages 197–220 (2020).